Conceptualization and Application of Unmanned Aerial Vehicles Design Methodology

Daniel Patinha Coelho

Thesis to obtain the Master of Science Degree in

Aerospace Engineering

Supervisor: Prof. Agostinho Rui Alves da Fonseca

Examination Committee

Chairperson: Prof. Filipe Szolnoky Ramos Pinto Cunha
Supervisor: Prof. Agostinho Rui Alves da Fonseca
Member of the Committee: Doutor Frederico José Prata Rente Reis Afonso

July 2019

To my parents, Sandra and Jorge.
To my love, Inês.
To my family and friends.

To my dear friend, Domingos.
I sworn to live a successful life in your memory so to avenge that so unfairly taken from you. This is the first step. May the light of your smile shine ever brighter upon the ones you left behind. Keep watching over us as we keep preserving your memory in our thoughts and our hearts.
Until we meet again.

Abstract

Unmanned Aerial Vehicles (UAV) are the subject of study for over half a century. The first steps taken into the world of unmanned aircraft were mostly bounded with adapting existent manned aircraft into unmanned. With the technological evolution experienced in the recent decades UAV emerged as unique aircraft with a dedicated branch of the aviation industry. Despite this fact, the UAV world is yet somewhat secret when it comes to the conceptual design of such machines. As there are methodologies for manned aircraft conceptual design, provided by authors such as Jan Roskam, Daniel P. Raymer, Thomas C. Corke and Mohammad H. Sadraey, among others, a similar methodology should also be developed for the design of fixed-wing UAV. Albeit such methodology may be partially based on the existent manned aircraft conceptual design methodologies, there are many details that impose a great difference between manned and the existent unmanned aircraft, from the usually different take-off mass to the overall configuration of the aircraft. The uniqueness of UAV in comparison with manned aircraft becomes even more evident as the Reynolds number experienced in flight decreases, due to the smaller size and lower flight speeds. The conceptualization and application of such methodology is the purpose of this work, which culminates in the development of a Medium Altitude Long Endurance (MALE) class UAV to be ultimately manufactured by UAVision Aeronautics.

Keywords

Conceptual Design Methodology, Unmanned Aerial Vehicle (UAV), Remotely Piloted Aerial Vehicle (RPAV), Medium Altitude Long Endurance (MALE), Low Reynolds.

Resumo

Veículos aéreos não tripulados, *Unmanned Aerial Vehicles* (UAV) em inglês, são objeto de estudo há mais de meio século. Os primeiros passos dados no mundo das aeronaves não tripuladas foram, na sua maioria, vinculados à transformação de aeronaves tripuladas existentes em aeronaves não tripuladas. Com a evolução tecnológica das últimas décadas, o UAV surgiu como uma aeronave única, com um ramo dedicado da indústria da aviação. Apesar deste facto, o mundo dos UAV ainda é um pouco secreto quando se trata do projeto conceptual de tais máquinas. Como existem metodologias para projeto conceptual de aeronaves tripuladas, formuladas por autores como Jan Roskam, Daniel P. Raymer, Thomas. C. Corke e Mohammad H. Sadraey, entre outros, uma metodologia similar também deveria ser desenvolvida para o projeto de UAV de asa fixa. Embora tal metodologia possa ser parcialmente baseada nas metodologias de projeto conceptual de aeronaves tripuladas existentes, há muitos detalhes que impõem uma grande diferença entre aeronaves tripuladas e aeronaves não tripuladas existentes, desde a geralmente diferente massa à descolagem até à configuração geral da aeronave. A singularidade do UAV em comparação com aeronaves tripuladas torna-se ainda mais evidente à medida que o número de Reynolds experienciado em voo desce, devido ao menor tamanho e menor velocidade de voo. A conceptualização e aplicação de tal metodologia é o objetivo deste trabalho, que culmina no desenvolvimento de um UAV da classe *Medium Altitude Long Endurance* (MALE) para ser posteriormente fabricado pela UAVision Aeronautics.

Palavras-Chave

Metodologia de Projeto Conceptual, Veículos Aéreos Não Tripulados, Veículos Aéreos Romotamente Pilotados, Média Altitude Longa Resistência, Baixo Reynolds.

Acknowledgments

The accomplishment of the present work allowed me the realization of an academic dream which dates back since before the start of my academic path in 2013. For a long time I have been passionate about aircrafts and especially unmanned aircrafts and that passion lead me to be involved in several extracurricular projects always aiming for the creation of an unmanned remotely piloted aircraft. The big leap for me, regarding this particular work, was the opportunity to design a proper unmanned aerial vehicle which I may get to see built. Furthermore, it was a great honor to develop such a work in cooperation with the leading unmanned aerial systems manufacturer in Portugal, UAVision Aeronautics. Without further due, I would like to express my sincere gratitude to all the people who help me get this far.

To Diogo Vicente, Aerospace Engineer at UAVision Aeronautics, for his devotion to this project from the absolute beginning and all his indispensable help throughout the development of this work. I could not have asked for a better mentor. Thank you Diogo.

To my university supervisor, Prof. Agostinho Fonseca, for never creating any difficulty in this process and for his help in the development of this document. Thank you professor.

To Nuno Simões, UAVision Aeronautics CEO, for never posing a problem regarding my internship, for the opportunity he gave me in joining the team and for his support regarding this work. Nuno, in just three month you already provided me with countless opportunities and on top of that you were always supportive regarding my thesis and also my personal life. Thank you very much.

To all my remaining colleagues at UAVision Aeronautics. For the great work environment, even in the most stressfull situations, for the companionship and welcoming you always provided me. Alda, Daniel, Henrique, Marco, Ricardo, Rodrigo, Sandro, Sónia, Vasco and Waqas, thank you all.

To the awesome colleagues and friends the academic life gave me, specially Joana, João and Pedro. This six year journey was much more bearable with your help. Thank you for all the work, sweat and adventures we shared. Also, in this regards, a special thank you to my godfather, José, who also became one of my closest friends.

To my closest friends André, Ariana, Daniela, Diogo, Duarte, Jorge, José, Luís, Tiago, who know me for a long time, shared this and many other journeys with me and who have always been present both in joy and sorrow. Wars come and go, but my soldiers stay eternal. I love you all from the bottom of my heart.

To my little cousins, André and Rafael, you're both blood of my blood and therefore part of me, now and forever. I wish you both all the best and even more than I wish for myself. I love you and will always be there for you.

To my grandfather, Manuel, for his undying support and care. I love you.

To my grandmother, Catarina, who, despite living far away for the past years, have been present through all my life, always loving are caring. I love you vuela.

To my one and only, Inês, whom I am lucky enough to have in my life. My love, none of this would mean anything without you. You are and always will be my reason to shine, so we may have the best life together. Thank you for who you are, for making me smile when I can't find any reason to do so, and for all the love we share. I will always love you my princess.

Finally, to my parents, Sandra and Jorge, for their love and undying devotion to me and my present and future well-being. This is yours, all for you. All my past, present and future conquests shall be dedicated to you, for it is the least you deserve. You are the main responsibles for my success and I will be forever in your debt. I could not have asked for better parents, neither for more love and attention than that you gave and will always give me. Love you Nita, love you Raton, always.

Contents

Abstract i
Resumo iii
Acknowledgments v
List of Figures ix
List of Tables xiii
List of Acronyms xv
List of Symbols xvii

1 Introduction **1**

2 Methodology **5**
2.1 Aircraft Conceptual Design Process 5
2.2 Unmanned Aerial Vehicles Database 8
2.2.1 Estimation of the Fuselage Maximum Diameter 9
2.2.2 Estimation of the Zero Lift Drag Coefficient 9
2.2.3 List of Unmanned Aerial Vehicles 10

3 Unfit Methodology Details **13**
3.1 Lift-To-Drag Ratio 13
3.2 Structural Factor 14
3.3 Aspect Ratio 14
3.4 Fuel Consumption 14
3.5 Efficiency Factor 14
3.6 Zero Lift Drag Coefficient 15
3.7 Airfoil, Taper and Sweep Angle Selection 15
3.8 Fuselage Design and Fineness Ratio 15
3.9 Tail Position and Size Coefficients 15

4 Proposed Methodology Adaptations **17**
4.1 Maximum Take-off Mass Estimation 17
4.1.1 Empty Mass 17

4.1.2 Fuel Fractions Estimation . . . 18
4.2 Wing Design . . . 23
4.2.1 Airfoil Selection . . . 23
4.2.2 Taper Ratio and Aspect Ratio . . . 25
4.2.3 Sweep Angle Selection . . . 28
4.2.4 Drag Estimation . . . 30
4.3 Fuselage Design . . . 35
4.4 Tail Design . . . 36
4.4.1 Length Ratio . . . 37
4.4.2 Tail Size Coefficients . . . 38
4.5 Verification of the Proposed Adaptations . . . 45

5 MALE UAV Design Project **49**
5.1 Requirements and Payload . . . 49
5.2 Take-off Mass Estimation . . . 51
5.3 Design Point Selection . . . 52
5.4 Wing Design . . . 54
5.5 Enhanced Lift Design . . . 57
5.6 Tail Design . . . 58
5.7 Engine Selection . . . 59
5.8 Fuselage Design . . . 60
5.9 Structure Design and Material Selection . . . 62
5.10 Refined Mass and Static Stability Analysis . . . 66
5.11 Heimdall's Overview and Performance . . . 67

6 Conclusions **71**
6.1 Future Work . . . 73

Bibliography **75**

A Aircraft Configurations **79**

B Aircraft Reference Definitions **83**

C Airfoil Studies **85**

List of Figures

2.1 Design process layout. 6

4.1 Structural factor distribution with the maximum take-off mass, from database. 18
4.2 Fuel mass fractions for different aircraft during a climb and accelerate to cruise condition flight phase. 19
4.3 Maximum range lift-to-drag ratio versus wing aspect ratio plot, from database. 21
4.4 Wing aspect ratio versus endurance plot, from database. 21
4.5 Maximum endurance lift-to-drag ratio against wing aspect ratio, from database. 22
4.6 Effect of the maximum thickness-to-chord ratio on the maximum lift coefficient for a variety of 2D airfoil sections. 23
4.7 Historic values of the maximum thickness-to-chord ratio on the main wing of aircraft as a function of Mach number. 23
4.8 Shape of the S1223, S2062 and SG6043 airfoils. 24
4.9 Lift coefficient evolution with the angle of attack at different Re, for the airfoils on table 4.1. 24
4.10 Drag coefficient evolution with the lift coefficient at different Re, for the airfoils on table 4.1. 24
4.11 Pitching moment coefficient evolution with the angle of attack at different Re, for the airfoils on table 4.1. 25
4.12 Lift-to-drag ratio evolution with the lift coefficient at different Re, for the airfoils on table 4.1. 25
4.13 Lift distribution for unswept, straight tapered wings of varying taper ratio. 26
4.14 Wing aspect ratio distribution with the maximum take-off mass, from database. 26
4.15 Influence of aspect ratio on the lift-to-drag ratio. 27
4.16 Influence of aspect ratio on the lift-to-drag ratio powered by three halves. 27
4.17 Taper ratio influence on the lift-to-drag ratio. 28
4.18 Taper ratio influence on the lift-to-drag ratio powered by three halves. 28
4.19 Left side: lift-to-drag ratio comparison between different taper configurations for the same wing area, always considering taper 0.4. Right side: planform shape of the different taper configurations considered. 28

4.20 Effect of sweep angle on delay of the drag rise. 29
4.21 Historic data showing values of sweep angle as a function of design Mach number. 29
4.22 Numerical calculation of induced drag factor for linearly tapered and elliptic wings. 30
4.23 Comparison between the presented formulations for estimating the drag coefficient of an aircraft. 32
4.24 Plots of the lift coefficient against the angle of attack for the wings used on the formulations comparison. 32
4.25 Zero lift drag coefficient distribution with the maximum take-off mass, from database. . . . 33
4.26 Zero lift drag coefficient distribution with the cruise Reynolds, from database. 33
4.27 Evolution of the overall drag coefficient with the fineness ratio for subsonic aircraft. 36
4.28 Fineness ratio against maximum take-off mass, differing by tail mount configuration, from database. 36
4.29 Length ratio for different engine positioning configurations. 38
4.30 Horizontal tail size coefficient distribution with the maximum take-off mass for the different engine positioning configurations referenced in appendix A. Taken from the database. . . 40
4.31 Horizontal tail size coefficient distribution with the maximum take-off mass for the different tail configurations referenced in appendix A. Taken from the database. 40
4.32 Size comparison between Hermes 450 and GNAT 750 unmanned aerial vehicles. 41
4.33 Horizontal tail size coefficient versus wing aspect ratio for different engine positioning configurations, from database. 42
4.34 Horizontal tail size coefficient versus wing aspect ratio, focusing on the difference between boom-mounted tails and conventional aft tails. 42
4.35 Horizontal tail size coefficient against the tail position over wing mean aerodynamic chord ratio, from database. 43
4.36 Total length over span ratio against wing aspect ratio, from database. 43
4.37 Vertical tail size coefficient distribution with the maximum take-off mass for different engine positioning configurations, from database. 44
4.38 Vertical tail size coefficient distribution with the maximum take-off mass for different tail configurations, from database. 44
4.39 Predator, General Atomics. 45
4.40 Hermes 450, Elbeit Systems. 45
4.41 Ogassa, UAVision Aeronautics. 45
4.42 Relative error of each computed property for the selected aircraft. 47

5.1 MX-15D gimbal, L3 WESCAM. 51
5.2 MX-10D gimbal, L3 WESCAM. 51

5.3 Epsilon 175, Octopus ISR Systems. 51
5.4 18xHD radar, Garmin. 51
5.5 Satellite communication system, Ultisat. 51
5.6 Design point selection for Heimdall's conceptual design project. 54
5.7 Heimdall wing planform shape. 55
5.8 Analyses of the airfoils in study. Left side: lift coefficient evolution with the the angle of attack. Right side: drag polar and respective polynomial fitting needed to acquire k. 56
5.9 Estimated 3D lift coefficient against angle of attack for Heimdall wing. 57
5.10 Heimdall's estimated drag polar. 57
5.11 RT600LCR-EXE engine. 60
5.12 Heimdall's fuselage layout. 61
5.13 V-n diagram showing Heimdall's flight envelope including gusts (full grey line). 63
5.14 Heimdall's wing structural layout. 65
5.15 EAM-12 life raft, Eastern Aero Marine. 68
5.16 EAM-25 life raft, Eastern Aero Marine. 68
5.17 Heimdall's overall look. Left side: top view. Right side: side view. 70

A.1 Gnat 750 by General Atomics, USA. 80
A.2 Hermes 900 by Elbeit Systems, Israel. 80
A.3 TD100 by BRICAN, Canada. 80
A.4 SkyPro V2 by SkyPro, UAE. 80
A.5 Tiguar C by UAVionics, Poland. 80
A.6 Wingo by UAVision, Portugal. 80
A.7 Heron by IAI, Israel. 80
A.8 Havoc by BrockTek, USA. 80
A.9 Sky-Y by Alenia Aeronautica, Italy. 80
A.10 Phoebus by Drone America, USA. 80
A.11 Argos by CATUAV, Spain. 81
A.12 Dominator by ADS, Israel. 81
A.13 Predator by General Atomics, USA. 81
A.14 Ogassa by UAVision, Portugal. 81
A.15 Recon by UASUSA, USA. 81
A.16 Phoebus by Drone America, USA. 81

B.1 Aircraft reference coordinate system. 84
B.2 Horizontal tail placement. 84

B.3 Vertical tail placement. 84
B.4 Location of the aerodynamic center for thin airfoils. 84
B.5 Leading edge sweep angle and quarter chord line sweep angle definitions. 84

C.1 Parabolic fitting, CLARK Y airfoil. 86
C.2 Parabolic fitting, EPPLER 387 airfoil. 87
C.3 Parabolic fitting, EPPLER 403 airfoil. 87
C.4 Parabolic fitting, EPPLER 423 airfoil. 88
C.5 Parabolic fitting, NACA 2412 airfoil. 88
C.6 Parabolic fitting, NACA 23012 airfoil. 89
C.7 Parabolic fitting, NACA 64110 airfoil. 89
C.8 Parabolic fitting, SELIG 1223 airfoil. 90
C.9 Parabolic fitting, SELIG 2027 airfoil. 90
C.10 Parabolic fitting, SG 6043 airfoil. 91

List of Tables

2.1 Different tail and engine configurations of the unmanned aerial vehicles considered in the database. . . . 8
2.2 Unmanned aerial vehicles considered in the database and some of their performance and design parameters. . . . 12

4.1 Airfoil exemplars fit for low Reynolds flyers. . . . 24
4.2 Main wing aspect ratio for different aircraft. . . . 26
4.3 Interference factor values. . . . 34
4.4 Length ratio range for different engine position configurations. . . . 38
4.5 Length ratio range proposed for unmanned aerial vehicles regarding different engine position arrangements. . . . 38
4.6 Tail size coefficients for different aircraft and tail configurations. . . . 39
4.7 Horizontal tail size coefficient range proposed for different engine position configurations. 42
4.8 Aircraft requirements for verifying the proposed methodology adaptations. . . . 45
4.9 Computed properties of the aircraft selected for verifying the proposed methodology adaptations. . . . 45
4.10 Relevant properties of the aircraft selected for verifying the proposed methodology adaptations. . . . 46

5.1 Inputs and result of the take-off mass estimation. . . . 52
5.2 Inputs for the design point selection. . . . 54
5.3 Heimdall wing planform shape parameters. . . . 55
5.4 Summary of the decision driver characteristics of the airfoils in study. . . . 55
5.5 Input parameters and outputs of the enhanced lift devices design. . . . 58
5.6 Heimdall's tail shape parameters. . . . 59
5.7 RT600LCR-EXE engine performance details. . . . 60
5.8 Parameters used for computing Heimdall's V-n diagram. . . . 62
5.9 Input parameters for computing the wing spar layering. . . . 64

5.10 Carbon fiber layering for the wing spar. 64
5.11 Refined mass estimates and computed moments of inertia. 66
5.12 Heimdall design and performance parameters. 67
5.13 Heimdall's payload options and expected performance. 68

C.1 k values obtained for the airfoils studied. 85

List of Acronyms

AFME Aft Fuselage Mounted Engine

ATME Aft Tail Mounted Engine

BMAT Boom Mounted A-Tail

BMHT Boom Mounted H-Tail

BMIUT Boom Mounted Inverted U-Tail

BMLT Boom Mounted L-Tail

BMPT Boom Mounted Pi-Tail

BMT Boom Mounted Tail

BMVT Boom Mounted V-Tail

CAD Computer Aided Design

CAT Conventional A-Tail

CG Center of Gravity

CTT Conventional T-Tail

CVT Conventional V-Tail

CYT Conventional Y-Tail

FMT Fuselage Mounted Tail

FMTE Fuselage Mounted Twin Engines

HALE High Altitude Long Endurance

MALE Medium Altitude Long Endurance

MTOM	Maximum Take-off Mass
MTOW	Maximum Take-off Weight
NME	Nose Mounted Engine
RPAV	Remote Piloted Aerial Vehicle
RPAS	Remote Piloted Aerial System
SF	Structural Factor
UAV	Unmanned Aerial Vehicle
UAS	Unmanned Aerial System
WME	Wing Mounted Engine
WMTE	Wing Mounted Twin Engine

List of Symbols

Greek symbols

α	Angle of attack
α_0	Zero lift angle of attack
δ	Departure of the wing loading distribution from eliptic
δ_f	Flap deflection
η	Propulsive efficiency
λ	Taper ratio
Λ_{LE}	Sweep angle respective to the leading edge
$\Lambda_{(\frac{t}{c})_{max}}$	Sweep angle respective to the maximum thickness line
$\Lambda_{\frac{c}{4}}$	Sweep angle respective to the quarter chord line
ρ	Mass of air per unit of volume

Roman symbols

A	Aspect ratio
b	Wing span
c	Aerodynamic chord
c_r	Aerodynamic chord at the root
c_t	Aerodynamic chord at the tip
$\bar{c}$	Mean aerodynamic chord
C	Specific fuel consumption

C_d	2D drag coefficient
C_D	3D drag coefficient
C_{d_0}	2D zero lift drag coefficient
C_{D_0}	3D zero lift drag coefficient
C_{d_i}	2D induced drag coefficient
C_{D_i}	3D induced drag coefficient
C_f	Friction coefficient
C_{HT}	Horizontal tail size coefficient
C_l	2D lift coefficient
C_L	3D lift coefficient
C_{l_α}	2D lift coefficient versus angle of attack slope
C_{L_α}	3D lift coefficient versus angle of attack slope
C_m	Pitching moment coefficient
C_{VT}	Vertical tail size coefficient
d	Fuselage equivalent diameter
D	Drag force
E	Endurance (or loiter time)
e_f	Efficiency factor
$\mathcal{F}$	Form factor
g	Gravity acceleration
h	Fuselage height
I	Moment of inertia
k	Departure from the presumed parabolic shape of the airfoil lift-drag polar
K'	Correction for nonlinear effects
K_Δ	Correction for nonlinear effects

K_n	Static margin
ℓ	Length
L	Lift force
m	Mass
M	Mach number
n	Load factor
N	Number of unmanned aerial vehicles
P	Propulsion power
$\mathcal{Q}$	Interferance factor
R	Range
Re	Reynolds number
s	Ground distance
S	Planform area
S_{wet}	Wetted area
t	Airfoil thickness
$\hat{u}$	Average normal gust speed component
V	Speed
w	Fuselage width
W	Weight
X	Generic variable

Subscripts

CAC	Property in the Climb and Acceleration to Cruise phase
Cl	Property in climb conditions
Cr	Property in cruise conditions
computed	Computed property

D Property in dash (maximum speed) conditions

database Property from database

dive Property in dive conditions

e Empty aircraft property

est Estimated value of property

ESTO Property in the Engine Start-up and Take-off phase

f Final value

flap Flap property

flapped Property of the wing with flaps in use

fuel Fuel property

fus Fuselage property

HT Horizontal tail property

highAoA Property at high angle of attack

i Initial value

Ld Property in landing conditions

Lt Property in loiter conditions

max Maximum value of property

min Minimum value of property

N Property in the Nth flight phase

opt Optimum value of property

pl Payload property

real Real value of property

res Reserve fuel property

S Property in stall conditions

SL Property at sea level

T	Tail property
To	Property in take-off conditions
Total	Aircraft overall property
VT	Vertical tail property
W	Wing property
WF	Wing flapped property

Chapter 1

Introduction

In the past, humanity's will to evolve and master abilities seen as impossible led to the development of outstanding machines ever more complex. That same will pushed the boundaries of technology further once the sky was conquered with aircraft. The evolution continued to a time in which aircraft may be unmanned and present a new way of mastering the sky. In the present days, the generations are becoming more and more familiarized with the so-called drones, nonetheless, the Unmanned Aerial System (UAS) technologies currently provided by the aviation industry are still a novelty for many people, despite being subjects of study for over half a century.

In fact, technological advances in the aviation industry throughout the past century provided the world with two kinds of unmanned aircraft, they are the Unmanned Aerial Vehicles (UAV) and the Remotely Piloted Aerial Vehicles (RPAV), which are both commonly referred to as drones. Despite the differences, since both are unmanned, the term UAV may be considered as the generic title, furthermore, some people use the terms RPAV and UAV interchangeably. To clarify, the UAV developer and user community uses the term UAV to refer to an unmanned aircraft capable of performing autonomous and preprogrammed missions whilst the term RPAV is used to describe an unmanned aircraft piloted from a remote location. An autonomous aircraft does not need to be remotely piloted, instead, the operator of such aircraft only needs to provide the system with waypoint coordinates. A waypoint is a set of instructions correlated to a set of geographic coordinates, it is the way of telling the system "go there and do this".

The development of UAS was a turning point for the aviation industry, specially on the military scope. Such systems allowed the fulfilment of many different agendas, previously possible only through manned missions, without the inherent risks a flight crew would undergo. Furthermore, UAS nowadays allow the execution of tasks that were otherwise much more expensive and sometimes unviable to perform from the skies, e.g. border patrol and maritime surveillance [1, 2]. Luckily UAS technologies grew largely in the past decades and now allow things that weren't thought possible a few generations ago.

Opposing to the general knowledge, UAV technologies already exist since before the first world war. The first UAV arose from a military perspective and the need to overcome the enemy forces technologically. For the sake of argument, one could say the first UAV was a stone thrown in the air in prehistoric times, or perhaps a chinese rocket launched in the thirteenth century, despite the fact that those "vehicles" had little or no control and essentially flew in a ballistic trajectory. If the generation of lift is a driver in naming the first UAV, maybe the kite wins the title. In fact, Douglas Archibald provided the world with one of the first reconnaissance UAV by attaching cameras to kites, in 1883 [1]. Nonetheless, it was only in the first world war that UAV became recognized systems and the Kettering Aerial Torpedo was developed as a detachable-wing biplane used for bombing enemy ground. Once above target, the wing would detach and the fuselage filled with explosives would plunge the ground like a bomb. Following this first aircraft, several other UAV were developed in the past and present centuries. From adapting existing manned aircraft into unmanned to designing and building an UAV from scratch, mankind has done it all, allowing the present generations the access to unmanned systems with unthinkable abilities that no manned aircraft should perform, considering the biologic limitations of the crew. For example, the Reaper, a weaponized variant of the Predator UAV developed by General Atomics, provided a unique capability never before seen in armed conflict, combining persistent surveillance and precision targeting with near instantaneous lethal response [2].

The reality of the aviation industry in the XXI century allowed the growth of the worldwide interest in the ever-improving concept of UAV. In fact, aside the military world, UAV have been developed for a variety of civil applications, from structural inspection, topographic analysis, crops surveillance and payload delivery, to search and rescue missions.

There are several UAV classes based primarily on their endurance and flight altitude [1, 2]. High Altitude Long Endurance (HALE) UAV are the largest and heaviest UAV in operation. Tactical UAV and Medium Altitude Long Endurance (MALE) are the two most prominent UAV classes, for aircraft belonging to these classes present the main desired features regarding common civil and military applications as they are designed for long duration tactical missions such as surveillance, reconnaissance and communications relay. The Small UAV class has also suffered a large development in the past years since it presents smaller UAV that, despite being less equipped and thus less effective than their larger relatives, are much more expendable and therefore more handy in closer and shorter applications, such as target acquisition in close combat. Also, their characteristics, especially the low cost, attracted civilian and private uses, e.g. crop surveillance and local cartography assessment. Technological advances are also allowing for the development of micro and nano UAV solutions.

Despite the visible growth of the UAS industry there still isn't an established methodology for the design of UAV as there are for manned aircraft, provided by numerous authors such as J. Roskam [3, 4], M. H. Sadraey [5], D. P. Raymer [6] and T. C. Corke [7], among others. The reason probably rests with

the economic interest of the many entities already manufacturing and retailing UAV.

Objectives

The present work was developed with the primary objective of suggesting changes to the existent conceptual design methodologies for manned aircraft, so to come up with a methodology best fitted for the conceptual design of fixed-wing UAV. A secondary objective was to develop the preliminary design of a MALE class UAV with requirements provided by UAVision Aeronautics, a portuguese UAV manufacturer which cooperated in the development of this work. Such requirements include a maximum payload of 150Kg and a minimum endurance for maximum payload of 15 hours, as well as the compliance with international aviation regulations.

Thesis Outline

Following this introductory chapter, a description of the design process and of the basic methodology applied for manned aircraft conceptual design is presented in chapter 2, along with a description of the UAV database which was created to support this work. Furthermore, a summary of the contents of the conceptual design methodology which need to be adapted to UAV design is presented in chapter 3. Afterwords, the adaptations proposed are presented in chapter 4, thus setting the methodology to be applied in the conceptual design of an UAV. In chapter 5 the conceptual design project of a MALE UAV is presented, following the methodology proposed and the requirements imposed by UAVision Aeronautics. Chapter 6 then presents the conclusion of this document and the future work proposals.

Chapter 2

Methodology

The present chapter sets the basis for the work developed. For starters it is of utmost importance to bear in mind that the methodology set for the conceptual design of UAV is based on the existent methodology for manned aircraft conceptual design proposed by authors such as Jan Roskam [3, 4], Daniel P. Raymer [6], Thomas. C. Corke [7] and Mohammad H. Sadraey [5]. For reference, the manned aircraft conceptual design methodology followed was the one proposed by T. C. Corke [7], which basically compiles information from some of the other mentioned authors. Also, the analysis of the methodology was performed in comparison with empirical data gathered in the UAV database that was created to support this work and will be described in section 2.2.

2.1 Aircraft Conceptual Design Process

Different authors propose different descriptions for the conceptual design process of an aircraft, despite they all end up reflecting more or less the same process and the same steps, only with different designations and sometimes with a different order for addressing design steps. Therefore, albeit some small differences, there is no methodology utterly better than the others and it is up to the designer to select which of the authors to follow. In the present work the methodology followed is the one proposed by T.C. Corke [7], although the order of addressing design steps is not entirely the same. The design process described in figure 2.1 is based on the proposal offered by T.C. Corke [7], where the the red color indicates the major design steps.

To promote a better understanding of the scope of the present work. a summarized description of the conceptual design process is presented, based on the literature [3, 5, 6, 7].

The first step on the conceptual design process is the estimation of the Maximum Take-off Mass (MTOM) of the aircraft, which is influenced by the payload requirement and the mission profile. Basically.

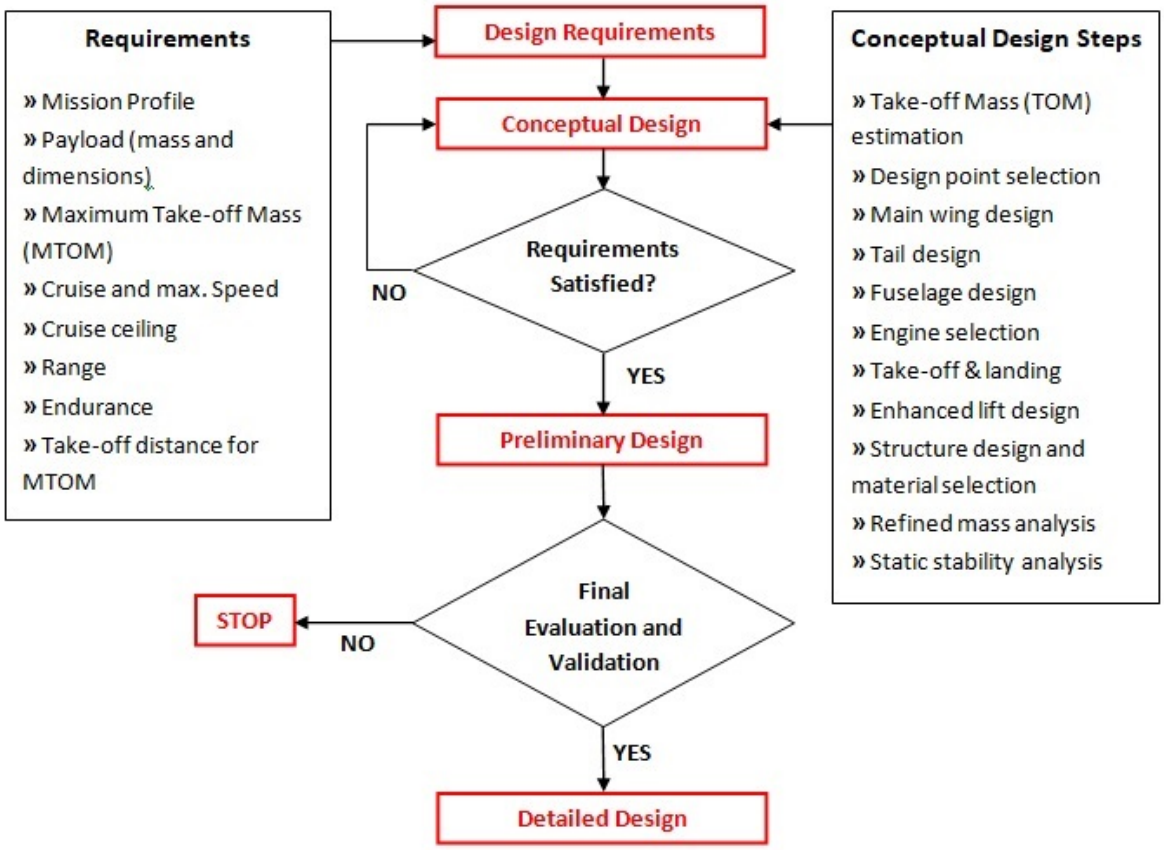

Figure 2.1: Design process layout.

the mission profile is reflected in the mass estimation for the fuel to be consumed in order to perform the required mission. The fuel mass estimation is then based in relations that have been developed in the past for each flight stage.

After the estimation of the MTOM, the selection of the design point follows. The design point reflects the choice for wing loading. $\frac{W}{S}$. where W is the aircraft's weight and S is the wing planform area, and power loading, $\frac{W}{P}$, where P is the propulsion power, P. For UAV with jet engines the thrust-to-weight ratio is considered, instead of the power loading. In other terms, one may see the design point as the ratio between wing area and propulsion power. The design point is influenced directly by the mission profile as well as the desired maneuverability, since there is a relation between the S and P required for the aircraft to be capable of sustaining each flight stage and performing each desired manoeuvre.

The next step is the wing design, where the geometry and the airfoil are selected. This is the first part of the conceptual design which is performed with less empirical assumptions. Since the goal is to get the wing geometry, the wing design must be done iterating with the design point since the design point provides the wing area needed based primarily on empirical assumptions.

With the wing design defined, the following step is the tail design which is performed based on

empirical relations and with respect to the main wing geometry. The goal at this stage is to get the first estimation of the horizontal and vertical tail sizes and position in relation to the main wing. It is also in this design step that the geometries and the airfoils of both surfaces are selected.

The fuselage design is the conceptual design step that follows, which has the objective of sizing the fuselage needed to accommodate the aircraft components and payload. The process is mainly based on empirical assumptions and the major concern is to plan the payload distribution bearing in mind the the location of the aircraft Center of Gravity (CG).

After the fuselage design it is time for the engine selection, which depends mainly on the amount of power needed, which by it-self is selected by the designer upon choosing the design point. Thus, the scope in this step is to select one engine or a set of engines able to provide the power required. The engine(s) selection must be performed taking into account the engine(s) location. If the choice is to attach engine(s) to the fuselage, the fuselage design step must be iterated.

The take-off and landing design step is when the designer can better estimate the take-off and landing distances based on the information provided from the design of the aerodynamic surfaces and engine selection which at this stage is already available. This design step is where the designer can foresee if enhanced lift devices are required based on take-off and landing distances requirements.

Afterwords, in the enhanced lift design step, the designer uses formulations to predict the amount of lift that several enhanced lift devices may produce and selects which of those devices to apply on the aircraft, in order to obtain the amount of lift needed for the aircraft to respect the requirements for take-off and landing distances.

The next step in the conceptual design of an aircraft is the structural design and material selection. In this step the driver is the ultimate load factor that the aircraft must withstand during operation. The load factor is a coefficient which multiplied by the aircraft Maximum Take-off Weight (MTOW) gives the load that the aircraft must sustain. On top of the load factor other safety factors are multiplied taking into account the airworthiness and certification of the aircraft. After the computation of the ultimate load, the basic internal structure of the aerodynamic surfaces and fuselage is devised.

The before last step in the conceptual design is the refined mass analysis, where the mass, dimensions and position of all aircraft components is attained and the inertia of the aircraft is studied in order to, as best as possible, obtain the location of the aircraft CG. This step is also performed by iterations with respect to the information obtained in the static stability analysis.

The static stability analysis is the last step on the conceptual design process and its purpose is to understand whether or not the aircraft would be capable of sustaining flight without active control.

2.2 Unmanned Aerial Vehicles Database

To support the present work a database of UAV was created. Despite the efforts to acquire the maximum amount of technical information regarding as many different UAV as possible, the success was not as notorious as it could be due to the fact that most of the UAV contacted manufacturers were not keen to provide such information, as they find it classified. Therefore it was only possible to collect data from UAV whose manufacturers have already made technical data available to the general public. Despite the large number of UAV existing nowadays worldwide, it was only possible to gather the necessary information for thirty eight of them. The specifications of each of these UAV, which provided the basis for the later estimations of several different design and performance parameters, were obtained either on their respective manufacturer brochure, upon direct contact with the respective manufacturer or by computation using the specific parameters available. As a way of supporting the results, the UAV selection was performed aiming to collect information on UAV with different configurations regarding the type of tail mountage and shape and also engine positioning. Table 2.1 shows the different configurations considered and the number of UAV, N, on the database with such configurations. The figures mentioned on this table are presented in appendix A and show an exemplar of the respective configuration.

Table 2.1: Different tail and engine configurations of the unmanned aerial vehicles considered in the database.

Tail Configuration	**N**	**Figure**
Boom Mounted A-tail (BMAT)	9	A.6
Boom Mounted H-tail (BMHT)	9	A.7
Boom Mounted Inverted U-tail (BMIUT)	2	A.10
Boom Mounted L-tail (BMLT)	1	A.8
Boom Mounted Π-tail (BMPT)	2	A.9
Boom Mounted V-tail (BMVT)	1	A.5
Conventional A-tail (CAT)	3	A.1
Conventional T-tail (CTT)	6	A.3
Conventional V-tail (CVT)	4	A.2
Conventional Y-tail (CYT)	1	A.4
Engine Configuration	**N**	**Figure**
Aft Fuselage Mounted Engine (AFME)	21	A.14
Aft Tail Mounted Engine (ATME)	7	A.13
Fuselage Mounted Twin Engines (FMTE)	2	A.16
Nose Mounted Engine (NME)	2	A.11
Wing Mounted Engine (WME)	3	A.15
Wing Mounted Twin Engines (WMTE)	3	A.12

Despite the low number of UAV exemplars, the database served its purpose which was to prove by simple assumptions, supported by the relations and proposals provided by T. C. Corke and the other already mentioned authors [3, 5, 6, 7], that the values for a number of parameters used in the conceptual design of a manned aircraft do not apply for UAV conceptual design, as will be explained in chapter 3.

Several technical parameters of the UAV in the database were studied and related to each other

with the scope of finding relations from which to support the changes to the conceptual design values and procedures that will be proposed in chapter 4. Albeit many parameters had no apparent relations, other presented visible relations and were thus used to support the work presented in chapter 4. Apart from the parameters that were computed based on design data, it was found the need to estimate two parameters which, for being considered sensitive technical information, were not provided by the manufacturers. Such parameters are the zero lift drag coefficient, C_{D_0}, and the fuselage maximum diameter, d_{max}. For each one a description of the assumptions and methods followed for the estimation is presented.

2.2.1 Estimation of the Fuselage Maximum Diameter

It is of importance to mention that d_{max} is used in the fuselage conceptual design to estimate the aerodynamic drag resulting from the exposure of the fuselage to the airflow through the fineness ratio, $\frac{d_{max}}{\ell_F}$, where ℓ_F is the fuselage overall length. The problem for most UAV in the database arose from the fact that, contrary to the majority of manned aircraft, the fuselage does not have a cylindrical shape. To solve this problem a fair approximation is to consider the sectional area given by the fuselage maximum height, h_{max}, and width, w_{max}, and compute the equivalent circular sectional area and afterwords obtain d_{max}. The mathematical relation used for this computation is given by equation .

$$d_{max} = \sqrt{\frac{4 \times h_{max} \times w_{max}}{\pi}} \tag{2.1}$$

2.2.2 Estimation of the Zero Lift Drag Coefficient

In order to obtain an estimate of C_{D_0} a basic assumption was made regarding the project of the UAV in the database. The assumption was that the optimum lift coefficient, $C_{L_{opt}}$, which is the C_L value considered in conceptual design of an aircraft, occurs for the maximum lift-to-drag ratio, $\left(\frac{L}{D}\right)_{max}$, where L is the lifting force and D is the drag force, as it is assumed for the preliminary design of every propeller driven aircraft. Furthermore, $\left(\frac{L}{D}\right)_{max}$ occurs when the induced drag coefficient, C_{D_i}, equals C_{D_0} [7], thus the overall drag coefficient, C_D, equals two times the C_{D_0} value, according to equation 2.2, where A is the wing aspect ratio and e_f is the efficiency factor. At this stage, e_f is assumed to take the average value of 0.8, which is an inaccurate assumption as will be explained. Nonetheless the value of 0.8 is proposed by T. C. Corke and the other authors [3, 5, 6, 7] and thus it will be used, since the goal is to prove that the C_{D_0} range proposed in manned aircraft conceptual design methodologies does not apply to UAV design. Afterwords, the computation of $C_{L_{opt}}$ was based on the procedure presented next.

$$C_D = C_{D_0} + \frac{C_L^2}{\pi A e_f} \tag{2.2}$$

- In cruise conditions thrust, T, equals drag, D, and lift, L, equals the weight of the aircraft, W, approximately, thus equation 2.3 applies. In equation 2.3, g is the gravity acceleration, V_{Cr} is the cruise speed, P_{Cr} is the power used for cruise, η is the propulsive efficiency and $(\%P)_{Cr}$ is the percentage of the total power, P, that is used for cruise.

$$\frac{L}{D} = \frac{W}{T} = \frac{MTOMg}{\frac{P_{Cr}}{V_{Cr}}} = \frac{MTOMgV_{Cr}}{\eta(\%P)_{Cr}P} \tag{2.3}$$

- The real lift coefficient, $C_{L_{real}}$, is given by equation 2.4, where ρ is the air density and S_W is the wing area, and the real drag coefficient, $C_{D_{real}}$, is given by equation 2.5. Therefore C_{D_0} may be expressed as in equation 2.6.

$$C_{L_{real}} = \frac{MTOMg}{\frac{1}{2}\rho V_{Cr}^2 S_W} \tag{2.4}$$

$$C_{D_{real}} = \frac{C_{L_{real}}}{L/D} \tag{2.5}$$

$$C_{D_0} = \frac{C_L}{L/D} - \frac{C_L^2}{\pi A e_f} \tag{2.6}$$

- $\left(\frac{L}{D}\right)_{max}$ is given by equation 2.7 and the optimum lift coefficient, $C_{L_{opt}}$, is given by equation 2.8. This equations are provided by T. C. Corke [7].

$$\left(\frac{L}{D}\right)_{max} = \sqrt{\frac{\pi A e_f}{4C_{D_0}}} \tag{2.7}$$

$$C_{L_{opt}} = 2C_{D_0}\left(\frac{L}{D}\right)_{max} \tag{2.8}$$

- Tuning the value of $(\%P)_{cruise}$ so that $C_{L_{real}} \approx C_{L_{opt}}$, it is possible to obtain a value for C_{D_0} as close as possible to the real one and thus evaluate this parameter.

2.2.3 List of Unmanned Aerial Vehicles

Table 2.2 shows the list of unmanned aerial vehicles considered in the database and some of their performance and design parameters. Notice that E_{max} is the maximum endurance, Re_{Cr} is the cruise Reynolds, SF is the structural factor, C_{HT} and C_{VT} are the horizontal a vertical tail size coefficients, respectively, and the acronyms on the configuration column are presented in table 2.1 and also on the

acronyms list. It is also of importance to mention that table 2.2 does not represent the entire database, instead it only presents the parameters thought off as the most important regarding the present work.

Only fixed-wing propeller driven UAV were considered in the database. The reason for this choice is that the vast majority of the existent UAV are propeller driven aircraft due to their low required flight speeds.

Table 2.2: Unmanned aerial vehicles considered in the database and some of their performance and design parameters.

UAV	MTOM [kg]	E_{max} [h]	V_{Cr} [m/s]	S_w [m^2]	A	Re_{Cr}	SF	C_{HT}	C_{VT}	C_{D_0}	Configuration
Aerosonde 4	15	24	25.72	0.567	14.75	310649	0.6	1.23	0.072	0.014	BMAT + AFME
Aerostar	200	9	31.86	4.27	9.89	1293235	0.5	0.46	0.036	0.029	BMPT + AFME
Anka	1600	24	40	13.6	22	1942523	0.44	0.74	0.016	0.033	CVT + ATME
Argos	12	14	18.9	0.864	10.47	336147	0.48	0.59	0.033	0.019	CTT + NME
Argus	90	10	36.01	2.24	12.54	940175	0.68	1.04	0.052	0.01	BMAT + AFME
Bayraktar	650	24	38.6	9.6	15	1907615	0.57	0.39	0.026	0.019	BMAT + AFME
Border Eagle	15	10	20	0.883	10.88	351919	0.6	0.28	0.013	0.022	BMHT + AFME
Dominator	1910	28	57	17.8	10.24	4642741	0.63	0.54	0.036	0.014	CTT + WMTE
F300	25	10	20	1.73	5.2	712261	0.56	0.11	0.023	0.034	BMHT + AFME
Falco	420	14	40	4.53	11.44	1640746	0.71	0.89	0.056	0.039	BMHT + AFME
Flyox	4000	25.8	64.8	32.2	6.09	9206959	0.55	0.42	0.048	0.019	CVT + WMTE
Gnat 750	510	48	40	5.9	19.62	1354918	0.5	0.75	0.017	0.02	CAT + ATME
Harfang	1250	24	40	13.2	20.88	1964894	0.53	0.89	0.045	0.023	BMHT + AFME
Havoc	79.4	18	25.7	3.27	7.34	1059760	0.48	0.34	0.046	0.025	BMLT + AFME
Hermes 450	550	30	36.2	7.7	14.32	1639923	0.48	0.36	0.02	0.028	CVT + ATME
Hermes 900	1180	36	31.3	13.3	16.92	1714423	0.7	0.72	0.028	0.065	CVT + ATME
Heron	1270	52	30.9	15.35	17.94	1765883	0.47	0.81	0.028	0.056	BMHT + AFME
Heron TP	5670	36	67.1	27.5	24.58	4384249	0.49	1.19	0.04	0.012	BMHT + AFME
Hunter	884.51	21	36	9.1	11.98	1938460	0.74	1.05	0.046	0.063	BMHT + TMFE
I-Gnat	700	48	40	8.3	19.93	1594816	0.55	0.77	0.017	0.019	CAT + ATME
Nightwarden	340	15	46.3	4.7	10.43	1920411	0.32	0.24	0.016	0.015	BMAT + AFME
Ogassa	36	8	25.72	1.06	16.64	400997	0.61	1.02	0.061	0.022	BMAT + AFME
PD-1	40	10	26.4	1.17	13.68	477027	0.55	1.16	0.038	0.024	BMAT + AFME
Penguin B	21.5	20	22	0.79	13.78	325349	0.47	0.9	0.065	0.031	BMAT + AFME
Phoebus	221.8	7	26.82	7.31	8.58	1529798	0.33	0.16	0.026	0.028	BMIUT + TMFE
Predator	1020	24	37.55	11.455	24.64	1581645	0.5	0.75	0.013	0.033	CAT + ATME
Ranger	7	1.5	13.89	0.7	12.86	200213	0.6	0.5	0.016	0.028	CTT + WME
Raybird 3	20	15	33.3	0.9	9.9	620234	0.45	0.5	0.022	0.006	BMIUT + AFME
Recon	5.35	1	15.65	0.6	10.33	232959	0.58	0.32	0.0186	0.017	CTT + WME
Searcher Mk. III	450	18	30.9	5.1	14.33	1138612	0.73	0.77	0.051	0.08	BMHT + AFME
Shadow v2	170	6	36.2	2.6	7.11	1352156	0.49	0.49	0.029	0.046	BMAT + AFME
Skypro v2	5	3	13.9	0.7	5.71	300536	1	0.08	0.012	0.032	CYT + ATME
Sky-Y	1200	12	50	13.8	7.16	4289505	0.71	0.33	0.091	0.023	BMPT + AFME
TD100	25	2.3	23.15	1.38	18.12	395659	0.65	0.62	0.024	0.009	CTT + NME
Thor Twin	700	10	38.9	10	12.1	2184592	0.67	0.64	0.039	0.033	BMAT + WMTE
Tiguar C	25	20	25	1.73	9.73	650521	0.56	0.63	0.065	0.007	BMVT + AFME
Uqab	200	4	33.3	4.1	7.38	1533482	0.5	0.34	0.043	0.035	BMHT + AFME
Yarara	35	6	25	1.1	14.4	426838	0.66	1.29	0.028	0.024	CTT + WME

Chapter 3

Unfit Methodology Details

In this chapter the details of the manned aircraft conceptual design methodology that do not fit the design of UAV are outlined and an explanation is provided regarding the reason why they are unfitted. A safeguard should be made at this point: the importance of outlining the unfitted details and ultimately propose more fitted alternative for them is bound with the fact that a more accurate initial guess will help reducing the number of iterations needed in the conceptual design process of an UAV.

3.1 Lift-To-Drag Ratio

The lift-to-drag ratio, $\frac{L}{D}$, is used in the TOM estimation through the computation of the fuel fractions. In the first step of the conceptual design it must be estimated as a percentage of the maximum lift-to-drag ratio, $\left(\frac{L}{D}\right)_{max}$, which by itself is also estimated, therefore creating three issues. The first is related to the percentage of the the $\left(\frac{L}{D}\right)_{max}$ that is considered. Most UAV, specially in the tactical UAV class, have outboard equipment exposed to the airflow and, due to the lower flight speeds usually experienced by UAV, the drag caused by equipment exposed to the airflow makes a bigger impact on the overall drag of the aircraft, thus lowering the effective $\frac{L}{D}$ in comparison to $\left(\frac{L}{D}\right)_{max}$. The second issue is regarding the maximum lift-to-drag ratio itself, since the $\left(\frac{L}{D}\right)_{max}$ used in the conceptual design is recurrently the one which reflects range-wise efficiency, since manned aircraft are normally design giving more importance to range requirements than to endurance. The case is not the same for many UAV since they are usually designed aiming for loiter efficiency, meaning that the major design driver efficiency-wise is the endurance. The third issue is also related to the $\left(\frac{L}{D}\right)_{max}$ and it is due to the fact that the proposed values for this parameter are based on manned aircraft classes and thus are not fit to most UAV.

3.2 Structural Factor

The Structural Factor (SF) is also used in the MTOM estimation and its purpose is to account for the empty mass of the aircraft. Provided the present technologies regarding the use of composite materials it is not unusual to encounter UAV with structural factors much lower than those of manned aircraft. This fact is also helped by the lack of necessity to accommodate a flight crew, which helps in lowering the complexity of internal structures. Other factors related to the lesser need for redundancy in several components also help lowering the SF.

3.3 Aspect Ratio

The aspect ratio, A, has a major impact on the aircraft overall efficiency and, despite being somewhat a designer choice, may be influenced by mission requirements. For example, if an UAV is to be designed aiming for efficient long endurance missions, it requires an high A [7]. On the other hand, if the mission requirements impose some sort of span limit, the initial A guess must be a lower value. Therefore, the conclusion is that UAV show a wide range of aspect ratios and, in some cases, may even present values above the normally seen in manned sailplanes.

3.4 Fuel Consumption

The fuel consumption, C, is an engine-related parameter which will affect the MTOM estimation through the computation of the fuel mass fractions on the cruise and loiter flight phases. In the literature [3, 5, 6, 7] values are proposed for several types of engines used in manned aircraft. The problem is that propeller driven UAV use smaller engines thus reflecting other values for specific fuel consumption.

3.5 Efficiency Factor

The efficiency factor, also known as Oswald's coefficient, which will be represented in this document by e_f to avoid confusion with the exponential symbol e, has an inverse influence on the induced drag coefficient, C_{D_i}, and by extension in the overall drag coefficient of the wing of an aircraft. This fact than causes a problem since the value of 0.8 proposed in the literature [5, 7] for this parameter, albeit being a good estimate for most manned aircraft for a number of reasons which are not in the scope of this work, may be very far from the values obtained for the majority of UAV. As will be explained, the efficiency factor is affected by a number of different parameters depending on the formulation used to estimate it, and thus may be estimated in a more conservative fashion.

3.6 Zero Lift Drag Coefficient

The zero lift drag coefficient, C_{D_0}, is one of the two components of the overall drag coefficient of an aircraft and for that reason it has an impact on the aircraft design. Since it requires an initial guess, a problem arises regarding the values proposed in the manned aircraft conceptual design methodologies [3, 5, 6, 7] because, as will be shown, UAV present a much wider range of values for this parameter. Also, most UAV present a C_{D_0} above the limit proposed for manned aircraft, C_{D_0}=0.02. Moreover, it is important to outline that, for aircraft having high aspect ratio and low efficiency factors, C_{D_0} gains much more influence on the overall drag coefficient, C_D, as will be shown in section 4.2.4. Being this the case, a proposal must be made for a more fitted initial value for this parameter.

3.7 Airfoil, Taper and Sweep Angle Selection

Despite not being any novelty, the airfoil, taper ratio, λ, and sweep angle, Γ, selection has a big impact on overall efficiency of the wing and therefore on that of the UAV itself. Therefore, when it comes to the efficiency-wise wing design of an UAV it is of importance to provide some considerations. Regarding the airfoil selection, some airfoils fitted for lower Reynolds flight will be pointed out. As for the taper selection, both the taper ratio and the span-wise starting point of the taper will be addressed. Concerning the sweep angle, the idea is to support the proposal for not adding leading edge sweep to the wing.

3.8 Fuselage Design and Fineness Ratio

Since on UAV there is no need to accommodate crew, the fuselage design is aimed to the accomodation of all the systems and payload. The existing conceptual design methodologies for manned aircraft approach the fuselage design with the scope of crew and passenger accommodation and comfort and thus do not provide any help when design the fuselage of an UAV. Being that the case, some considerations will be provided. Regarding the fineness ratio of the fuselage, which is given by the ratio between the fuselage maximum diameter and its length, the goal is to demonstrate which UAV configuration promotes the best efficiency-wise fineness ratio, $\frac{d}{\ell}$.

3.9 Tail Position and Size Coefficients

The tails positioning, given by the $\frac{\ell_T}{\ell_{Total}}$, where ℓ_T is the distance between the wing and the horizontal and vertical tails aerodynamic centers and ℓ_{Total} is the aircraft overall length, and the horizontal

and vertical tail size coefficients end up working hand-to-hand in the design of an UAV and reflect a compromise between the tails distance to the wing and their sizes, so that the aircraft is statically stable. The proposed values for the mentioned parameters, which reflect empirical data from manned aircraft, are somewhat unfitted for most UAV. Also, the conceptual design methodologies do not offer a way of estimating the tail size coefficients. Therefore, through the study of the UAV database developed, considerations will be presented regarding these parameters and a process for estimating an empirical value for the horizontal tail size coefficient will be provided.

Chapter 4

Proposed Methodology Adaptations

In this chapter a discussion is placed regarding each of the parameters that were pointed out in the previous chapter and ultimately an estimate or a proposal for the estimation of such parameters is provided. The parameters found to be troublesome were basically related to four different steps of the conceptual design methodology: the TOM estimation, the wing design, the fuselage design and the tail design. For organization purposes the present chapter is then divided in four sections, each dedicated to one of the aforementioned design steps.

4.1 Maximum Take-off Mass Estimation

The take-off mass, MTOM or m_{To}, of an UAV may be estimated by equation 4.1, where m$_{pl}$ is the payload mass, m_e is the empty mass of the aircraft, m_{fuel} is the fuel mass and m_{res} is the reserve fuel mass, given as a percentage of m_{fuel}. At this stage the payload requirement is already established and thus m$_{pl}$ is known.

$$m_{To} = m_{pl} + m_e + m_{fuel} + m_{res} \tag{4.1}$$

4.1.1 Empty Mass

The empty mass estimation is performed in the literature [3, 5, 6, 7] through the use of a Structural Factor (SF), according to equation 4.2.

$$m_e = SF \times m_{To} \tag{4.2}$$

The structural factor is the ratio between the empty mass of an aircraft and its m_{To} and, in the con-

ceptual design, it is estimated based on empirical data. At the current stage of the UAV industry, the SF depends mostly on the efficiency (mass-wise) of the composite materials used as well as the construction methods. Additionally, the SF also depends and the mission, since an UAV for long endurance has a SF lower than one for shorter endurance, due to the amount of fuel carried. Figure 4.1 shows the structural factors of the UAV considered in the database. There it is visible that the SF may be as low as around 0.3, nonetheless, a good initial guess for the structural factor is 0.5 because, as explained, the SF depends on materials and methods which may not be perfect.

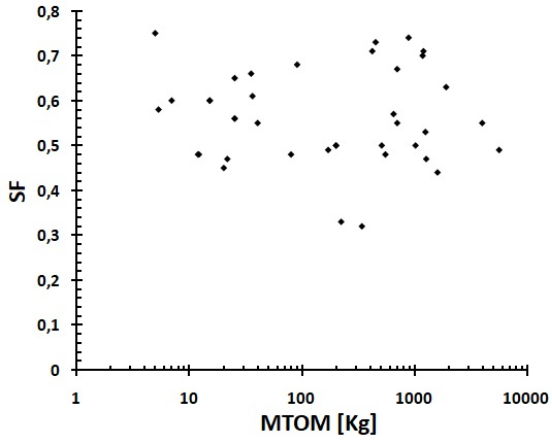

Figure 4.1: Structural factor distribution with the maximum take-off mass, from database.

4.1.2 Fuel Fractions Estimation

The typical flight plan of an UAV designed for surveillance (as are the vast majority) is comprised by five different flight phases: **Engine Start-up and Take-off**, **Climb and Acceleration to Cruise**, **Cruise**, **Loiter** and **Landing**, here highlighted in bold for better understanding. Following the methodology proposed by T. C. Corke [7], the mass of fuel needed is computed through the use of historic fuel mass fractions for each mission phase, as shown by equation 4.3 where m_{Ld} is the mass of the aircraft at **Landing** and m_N is the aircraft mass at the Nth flight phase.

$$m_{fuel} = \left(1 - \frac{m_{Ld}}{m_{To}}\right) \times m_{To} = \left[1 - \frac{m_2}{m_1} \times \frac{m_3}{m_2} \times (...) \times \frac{m_N}{m_{N-1}}\right] \times m_{To} \tag{4.3}$$

For the first and last flight phases, **Engine Start-up and Take-off** and **Landing**, the fuel mass fractions are estimated based on empirical data from many aircraft and thus it is considered to be the same for UAV. As a reference, T. C. Corke [7] proposes a fuel mass fraction for **Engine Start-up + Take-off** shown in equation 4.4, where m_i represents the aircraft mass at the beginning of one flight phase and m_f the mass at the end of that same flight phase. The fraction proposed by this author for

the **Landing** phase is the same. Here a note may be introduced regarding the **Landing** phase of an UAV. Despite being a conservative measure to consider in **Landing** the same amount of fuel spent in **Engine Start-up + Take-off**, this is not true for most UAV since it is somewhat uncommon for UAV to use their thrust to slow down. For manned aircraft this is considered because in the **Landing** many exemplars use thrust from the engines to slow down (reverse thrust). What usually occurs during the **Landing** phase of an RPAS, for example, is a thrust reduction, in order to allow the aircraft to be slowed down by the drag force induced by the airflow, and the touch down occurs at stall, which is accurately controlled by the pilot.

$$0.97 \leq \left(\frac{m_f}{m_i}\right) \leq 0.975 \tag{4.4}$$

Regarding the **Climb and Acceleration to Cruise** fuel mass fraction, T. C. Corke proposes a value around 0.95 [7] because it considers an acceleration from M=0.1 to approximately M=1, being M the Mach number. This does not apply to the vast majority of UAV since only HALE UAV fly above M=0.2. Nonetheless, figure 4.2 presents a relation between this particular fuel mass fraction and the cruise mach number.

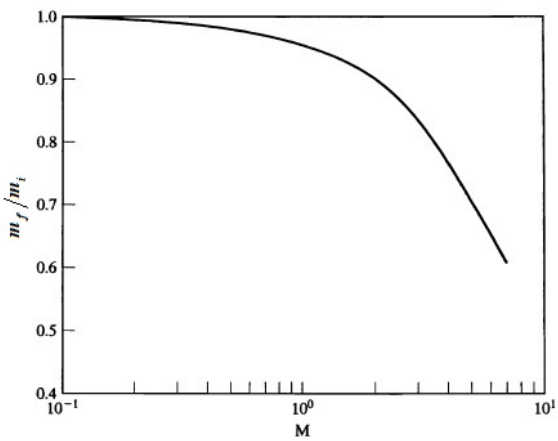

Figure 4.2: Fuel mass fractions for different aircraft during a climb and accelerate to cruise condition flight phase [7].

In this regards, it would be straightforward to consider a fuel mass fraction of 1 for this flight phase to be applied to UAV flying bellow M=0.2, which reflects a cruise speed of V_{Cr}≈66.56m/s. Nonetheless, for a conservative approach it may be considered a fuel mass fraction of 0.99.

As for the remaining flight phases, **Cruise** and **Loiter**, it is more difficult to estimate their respective fuel mass fractions and thus will be discussed with more detail.

Cruise Phase

For this flight phase, instead of historic information there is an analytic formulation called the Breguet Range Equation from which it is possible to compute the mass fraction regarding the **Cruise** flight phase, $\left(\frac{m_f}{m_i}\right)_{Cr}$. For propeller aircraft the formulation is given by equation 4.5, where R is the cruise range, C is the fuel consumption and η is the propulsive efficiency. Also, $\frac{L}{D}$ is the lift-to-drag ratio, as previously explained.

$$\left(\frac{m_f}{m_i}\right)_{Cr} = e^{\left[-\frac{RC}{\eta(\frac{L}{D})}\right]} \tag{4.5}$$

At this point the $\frac{L}{D}$ ratio is not known and therefore has to be estimated. As suggested by T. C. Corke [7], $\frac{L}{D}\approx 0.94\left(\frac{L}{D}\right)_{R_{max}}$, being $\left(\frac{L}{D}\right)_{R_{max}}$ the $\frac{L}{D}$ ratio which maximizes the range in cruise.

A more conservative estimate for UAV is $\frac{L}{D}\approx 0.9\left(\frac{L}{D}\right)_{R_{max}}$. This small change is justified because the majority of UAV have outboard equipment that interferes with the airflow and, due to the low flight speed, cause the viscous drag force to be proportionally bigger than that on similar manned aircraft, thus making it harder to achieve $\frac{L}{D} = \left(\frac{L}{D}\right)_{R_{max}}$. With this in mind, the question now is estimating a good value for $\left(\frac{L}{D}\right)_{R_{max}}$, which also poses a problem.

The value for $\left(\frac{L}{D}\right)_{R_{max}}$ can be obtained using equation 4.6. Unfortunately in this design phase there is no information regarding A or C_{D_0}. To overcome this setback T. C. Corke [7] suggests values for $\left(\frac{L}{D}\right)_{R_{max}}$ for some aircraft categories, which do not apply to the majority of UAV. At this point a different approach was developed to obtain an empirically based estimate for $\left(\frac{L}{D}\right)_{R_{max}}$, which is based on data computed in the database.

$$\left(\frac{L}{D}\right)_{R_{max}} = \sqrt{\frac{\pi A e_f}{4C_{D_0}}} \tag{4.6}$$

First it is necessary to provide an initial guess for the aspect ratio of the wing, A. From figure 4.4 it is possible to determine two classes of UAV based on their endurance: below 24h endurance 7≤A≤15, above 24h endurance 15≤A≤25. As it is possible to observe on figure 4.4, there are some UAV that fall out of these two classes, nonetheless, as far as this design stage is concerned, selecting an aspect ratio within this ranges is a good enough approach. As a recommendation, for E<24h consider A≈10 and for E>24h consider A≈20.

After selecting the A initial guess, it is possible to estimate $\left(\frac{L}{D}\right)_{R_{max}}$ through a linear relation with A, as proposed in the conceptual design methodologies [3, 5, 6, 7]. The proposal provided by T. C. Corke [7] for the mentioned linear relation is presented in equation 4.8. Figure 4.3 shows the plot of $\left(\frac{L}{D}\right)_{R_{max}}$ against A for the UAV considered in the database, where a linear relation between these two parameters may be seen. It is then viable to assume that $\left(\frac{L}{D}\right)_{R_{max}}$ and the wing A are related approximately like

in equation 4.7. Out of curiosity, the blue dashed line in figure 4.3 represents the approach given by equation 4.8. It is straightforward to conclude that approach proposed in equation 4.7 is best fitted for UAV preliminary design.

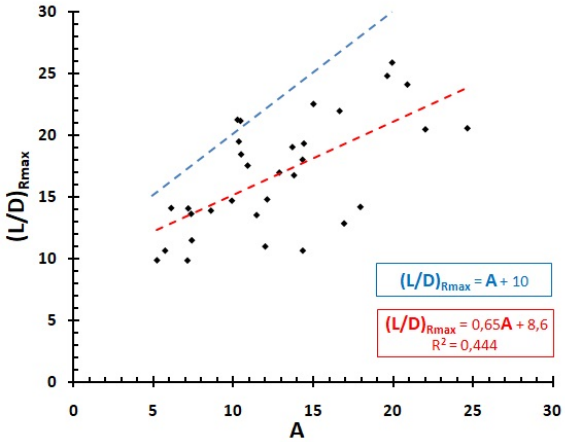

Figure 4.3: Maximum range lift-to-drag ratio versus wing aspect ratio plot, from database.

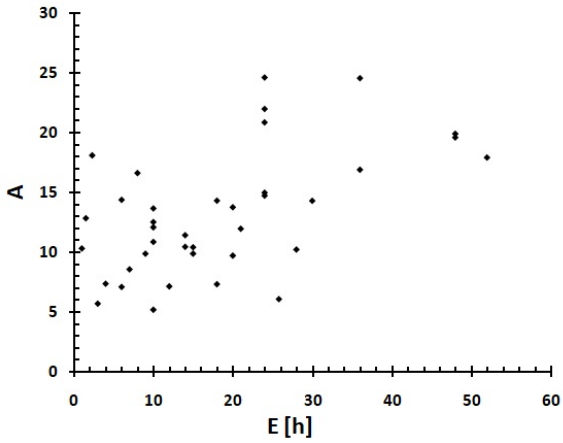

Figure 4.4: Wing aspect ratio versus endurance plot, from database.

$$\left(\frac{L}{D}\right)_{R_{max}} = 0.65A + 8.6 \tag{4.7}$$

$$\left(\frac{L}{D}\right)_{R_{max}} = A + 10 \tag{4.8}$$

Again, at this phase in the design the need is only to find a reasonable value for $\left(\frac{L}{D}\right)_{R_{max}}$, thus the proposed approach may be used.

Regarding the other two quantities presented on equation 4.5, the C and η, it is safe to assume for this design phase that C=0.5$\frac{Kg}{kWh}$ for 2-stroke engines, used normally in UAV with MTOM below 50kg [8], C=0.3$\frac{Kg}{kWh}$ for 4-stoke or Wenkel engines, used in UAV with MTOM over 50kg [8], and η = 0.8, as is proposed by T. C. Corke [7] for personal propeller driven aircraft and also proposed by D. F. Rogers[9] and B. D. Rutkay [10] for UAV. The values for the fuel consumption were proposed based on UAVision Aeronautics experience with several UAV engines, nonetheless, fuel consumption information may be found on propeller driven engine manufacturers [11, 12, 13, 14, 15]. The value for η may also be estimated at this stage through manufacturers data [16]. Also, M. Adamsky [8] provides an extensive analysis on UAV propulsion systems and may be a good tool for selection.

Finally it is now straightforward to determine the mass fractions for the cruise flight phase.

Loiter Phase

For this flight phase there is also an analytic formulation called the Breguet Endurance Equation from which it is possible to compute the mass fraction $\left(\frac{m_f}{m_i}\right)_{Lt}$. For propeller aircraft the formulation is given

by equation 4.9, where V_{Lt} is the loiter speed and E is the endurance.

$$\left(\frac{m_f}{m_i}\right)_{Lt} = e^{\left[-\frac{EV_{Lt}C}{\eta(\frac{L}{D})}\right]} \tag{4.9}$$

According to J. Roskam [3], the lift-to-drag ratio that maximizes E, $\left(\frac{L}{D}\right)_{E_{max}}$, is provided by estimating $\frac{L}{D}$ for so that the ratio $\frac{L^3}{D^2}$ is maximized. Therefore, $\left(\frac{L}{D}\right)_{E_{max}}$ may be estimated through equation 4.10. As a conservative approach, similar to that suggested for the **Cruise** phase, $\frac{L}{D}$ may be estimated as $\frac{L}{D}$≈0.9$\left(\frac{L}{D}\right)_{E_{max}}$.

$$\left(\frac{L}{D}\right)_{E_{max}} = \sqrt{\frac{3\pi A e_f}{16 C_{D_0}}} \tag{4.10}$$

Regarding the estimate for $\left(\frac{L}{D}\right)_{E_{max}}$ an approach similar to that proposed for $\left(\frac{L}{D}\right)_{R_{max}}$ is followed. Knowing the required loiter speed, V_{Lt}, having chosen the wing A and considering C and η to be the same as proposed for the **Cruise** phase, it is now possible to estimate $\frac{L}{D}$ through the relation proposed in equation 4.11. This relation is a simplified approximation which is supported by figure 4.5. It is then possible to estimate the fuel mass fraction for the loiter phase.

$$\left(\frac{L}{D}\right)_{E_{max}} = 0.56A + 7.5 \tag{4.11}$$

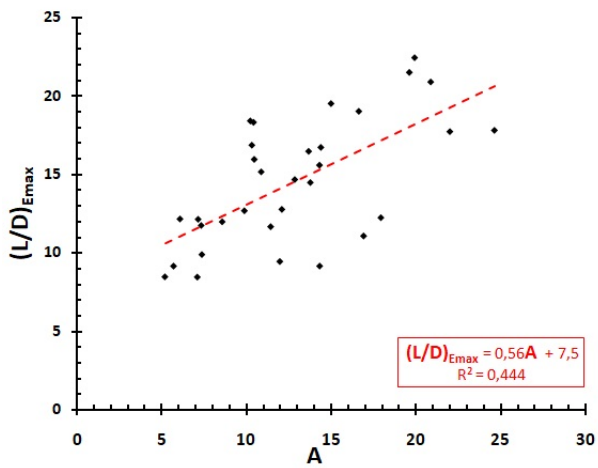

Figure 4.5: Maximum endurance lift-to-drag ratio against wing aspect ratio, from database.

4.2 Wing Design

The conceptual design of the main wing of an aircraft consists of selecting the cross-section shape (airfoil), the aspect ratio, A, the taper ratio, λ, which is given by equation 4.12, and the sweep angles, Λ_{LE}, $\Lambda_{(\frac{t}{c})_{max}}$ and $\Lambda_{\frac{c}{4}}$. There are many requirements that may influence the wing design, namely performance requirements (MTOM, cruise speed, V_{Cr}, stall speed, V_s, range, endurance, maneuverability, etc.) and structural requirements (internal volume, maximum allowed span, structural mass, etc.). For UAV that fly at low speeds (below M=0.2), the main objective in the wing design is usually its efficiency, whether the goal is maximum range or maximum endurance.

4.2.1 Airfoil Selection

Regarding the airfoil selection, one of the core aspects is the thickness, t, which directly influences the choice of the airfoil through the maximum thickness-to-chord ratio, $\left(\frac{t}{c}\right)_{max}$. This is of utmost importance in UAV design since a thinner airfoil allows for a thinner spar, which may pose a problem when designing UAV with high A. The value for the $\left(\frac{t}{c}\right)_{max}$ ratio in low speed flyers is normally $\left(\frac{t}{c}\right)_{max}$≈14$\%$ because, as it was proven by the National Advisory Committee for Aeronautics (NACA) [17], for a variety of airfoil sections a $\left(\frac{t}{c}\right)_{max}$≃14$\%$ provides for the highest maximum lift coefficient, $C_{l_{max}}$, as shown in figure 4.6. Therefore $\left(\frac{t}{c}\right)_{max}$=14$\%$ is a good value to aim for when selecting and airfoil. Also, historical data shows that low speed flyers tend to use airfoils with $\left(\frac{t}{c}\right)_{max}$ close to 14%, as figure 4.7 shows.

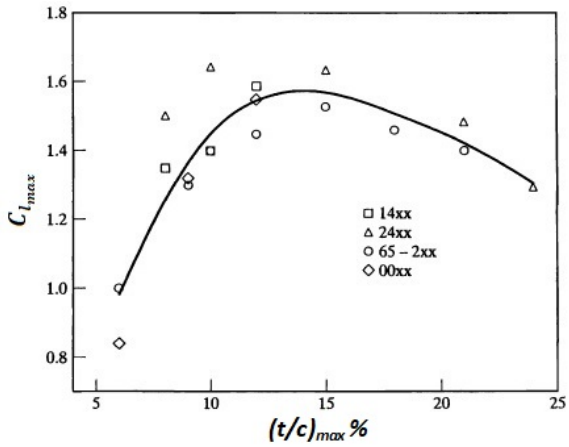

Figure 4.6: Effect of the maximum thickness-to-chord ratio on the maximum lift coefficient for a variety of 2D airfoil sections [17].

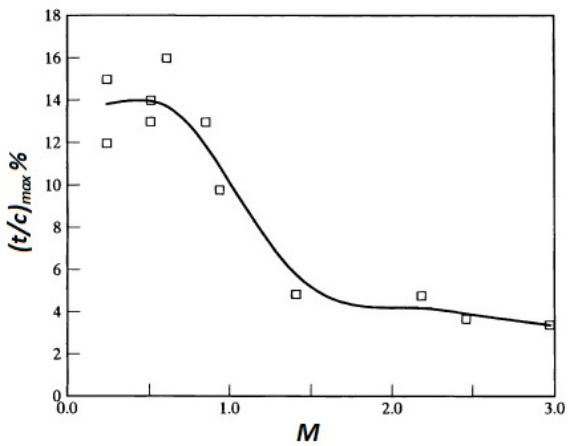

Figure 4.7: Historic values of the maximum thickness-to-chord ratio on the main wing of aircraft as a function of Mach number [6].

Another thing to take into account when selecting the airfoil is the pitching moment coefficient, C_m, because for lower absolute C_m the horizontal tail area may be smaller, since one of the most important uses for the horizontal tail is counteracting the pitching moment.

Apart the enormous amount of airfoils developed by NACA, some of the most common airfoils used

in UAV are the Selig airfoils [18], which were specifically designed for flight at lower Re. Just for a matter of reference when doing the airfoil selection, three different Selig airfoils are presented in figure 4.8 and somewhat described in table 4.1. The S1223 airfoil was designed for high lift and thus it is best suited for UAV with large MTOM, the S2062 was designed for higher flight speeds and small MTOM and the SG6043 sits in between the two previously mentioned airfoils. Furthermore, figures 4.9, 4.10, 4.11 and 4.12 show the most relevant properties, regarding this design phase, of the three proposed airfoils for different Re. Also, in appendix C other airfoils are presented as well as their lift and drag characteristics at different Re. The airfoils were studied in the XFLR5 software.

Table 4.1: Airfoil exemplars fit for low Reynolds flyers.

Airfoil	$(t/c)_{max}$	Max camber
S1223	12.13 %	8.67 %
SG6043	10.01 %	5.5 %
S2062	7.93 %	1.73 %

Figure 4.8: Shape of the S1223, S2062 and SG6043 airfoils.

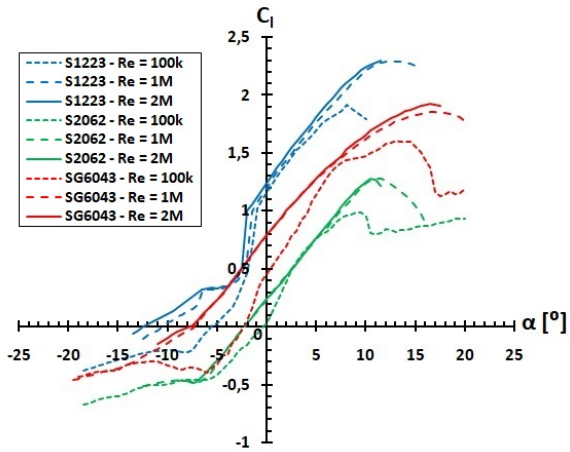

Figure 4.9: Lift coefficient evolution with the angle of attack at different Re, for the airfoils on table 4.1.

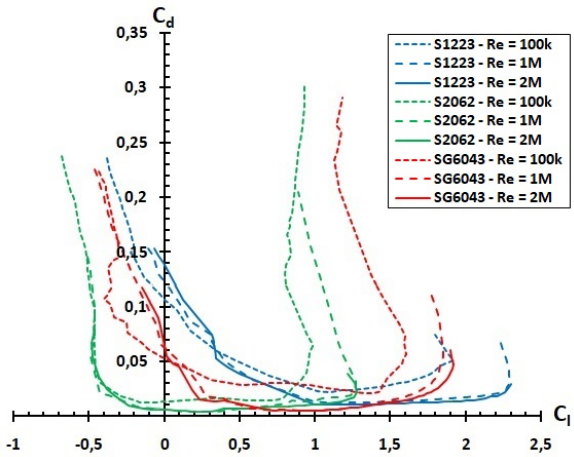

Figure 4.10: Drag coefficient evolution with the lift coefficient at different Re, for the airfoils on table 4.1.

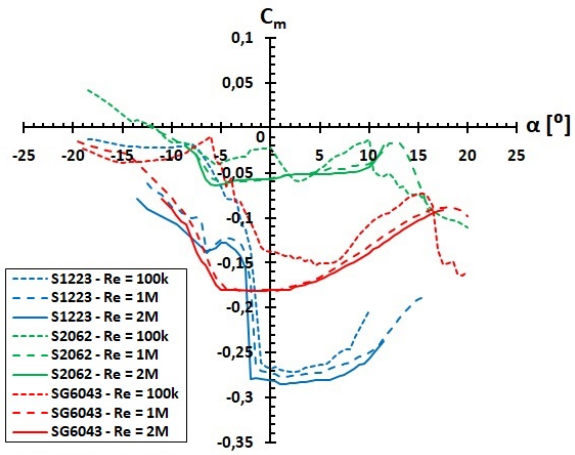

Figure 4.11: Pitching moment coefficient evolution with the angle of attack at different Re, for the airfoils on table 4.1.

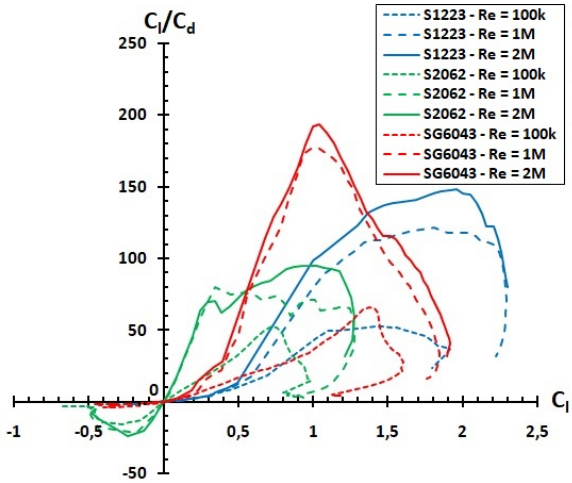

Figure 4.12: Lift-to-drag ratio evolution with the lift coefficient at different Re, for the airfoils on table 4.1.

4.2.2 Taper Ratio and Aspect Ratio

The wing taper ratio, λ, given by equation 4.12, and aspect ratio, A, given by equation 4.13, both have a major influence in the induced drag coefficient, C_{D_i}, which is given by equation 4.14. In fact, the A influence on C_{D_i} becomes clear by inspection of equation 4.14 and the λ influence on C_{D_i} is related to the span-wise lift distribution of the wing. As figure 4.13 shows, decreasing the taper ratio from a rectangular wing shape (λ=1) increases the lift at the wing tip. The assumed optimal taper ratio is λ=0.4 because it is the one which best approximates and ellipse-shaped wing. Form lifting line theory, an unswept, untwisted ellipse-shaped wing provides the minimum drag. Since an elliptic wing is harder to produce, the next best thing efficiency-wise is an untwisted straight tapered wing having λ=0.4.

$$\lambda = \frac{c_t}{c_r} \tag{4.12}$$

$$A = \frac{b^2}{S} \approx \frac{b}{\bar{c}} \tag{4.13}$$

$$C_{D_i} = \frac{C_L^2}{\pi A e_f} \tag{4.14}$$

Regarding the wing A, table 4.2 shows typical values for several aircraft and figure 4.14 shows the distribution with the MTOM for the UAV in the database. Similarly to what happens with figure 4.4, a closer look at figure 4.14 allows for the conclusion that the aspect ratio on UAV, 5≤A≤25, ranges more than what was empirically found for manned aircraft, 2.4≤A≤12.8. As equation 4.14 shows, A

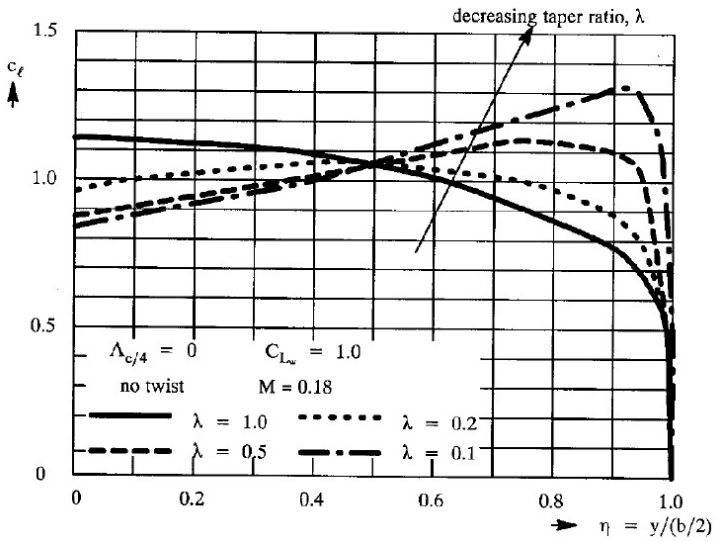

Figure 4.13: Lift distribution for unswept, straight tapered wings of varying taper ratio [3].

has an inverse relation with C_{D_i}, meaning that a bigger aspect ratio will produce a lower induced drag component. This is the reason why it is more efficient to have an A as big as physically possible. The physical limits for the A are the final span of the wing, b, and the wing thickness, t, which is directly related with the wing chord, c. As equation 4.13 shows, a bigger A means bigger span which, for the same total wing area, S, means having a smaller chord, therefore a thinner wing. This poses a problem because an high A introduces the need for a stronger internal wing structure, which implies more mass [5]. Therefore the A choice must be performed with care because without dully caution in the production process the increase in A may not compensate the loss of efficiency provoked by the mass gain. Also, a bigger A implies larger production costs [5, 6]. Nonetheless, in an UAV it is often viable to have a bigger A.

Table 4.2: Main wing aspect ratio for different aircraft [7].

Aircraft Type	A
Personal	5.0-8.0
Commuter	9.0-12.0
Regional Turboprops	11.0-12.8
Business Jets	5.0-8.8
Jet Transports	7.0-9.5
Military Fighter/Attack	2.4-5.0

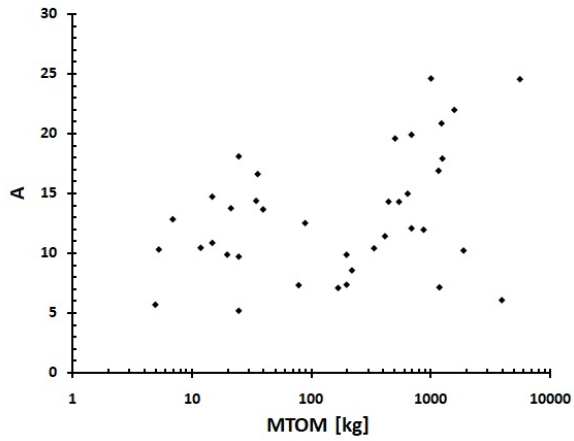

Figure 4.14: Wing aspect ratio distribution with the maximum take-off mass, from database.

To better demonstrate the A influence, an analysis was conducted using the XFLR5 software. Several

wings corresponding to increasing MTOM classes of UAV were analysed and the results are presented in figures 4.15 and 4.16. All the wings in this study were designed without twist or sweep and with λ=1. Also, their dimensions were carefully selected keeping in mind the structural complexity, thus limiting the A. Recalling what was stated in section 4.1.2, the aircraft range is maximum for $\left(\frac{C_L}{C_D}\right)_{max}$ and the endurance is maximum for $\left(\frac{C_L^3}{C_D^2}\right)_{max}$. As figures 4.15 and 4.16 show, increasing A will increase both $\left(\frac{C_L}{C_D}\right)_{max}$ and $\left(\frac{C_L^3}{C_D^2}\right)_{max}$, thus improving the aircraft range and endurance. Comparing figures 4.15 and 4.16 it is also noticeable that A has a much higher influence on $\left(\frac{C_L^3}{C_D^2}\right)_{max}$, meaning it is especially important to consider higher A values when designing an UAV for missions dominated by loiter flight stages.

In addition, in order to demonstrate the taper ratio influence on the aircraft performance, the higher A wings from the previous study were compared with similar wings having λ=0.4 starting from one third of the semi-span (see figure 4.19). The results are presented in figures 4.17 and 4.18 and show that having tapered wings with λ = 0.4 improves yet $\left(\frac{C_L}{C_D}\right)_{max}$ and $\left(\frac{C_L^3}{C_D^2}\right)_{max}$ and therefore the aircraft range and endurance.

The choice for λ=0.4 starting from one third of the semi-span was supported by a simple comparison between three different taper configurations: λ=0.4 starting from the wing root, λ=0.4 starting from one of the third semi-span, b/2, and λ=0.4 starting from two thirds of the semi-span. Figure 4.19 shows this comparison and allows for the conclusion that the best configuration is λ=0.4 starting from one of the third semi-span, nonetheless the difference between each configuration is almost neglectable.

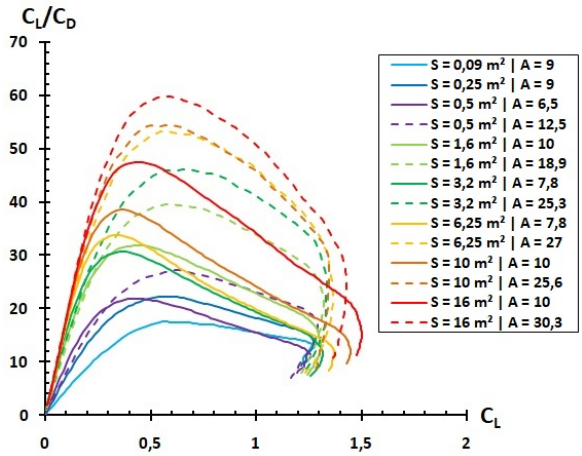

Figure 4.15: Influence of aspect ratio on the lift-to-drag ratio.

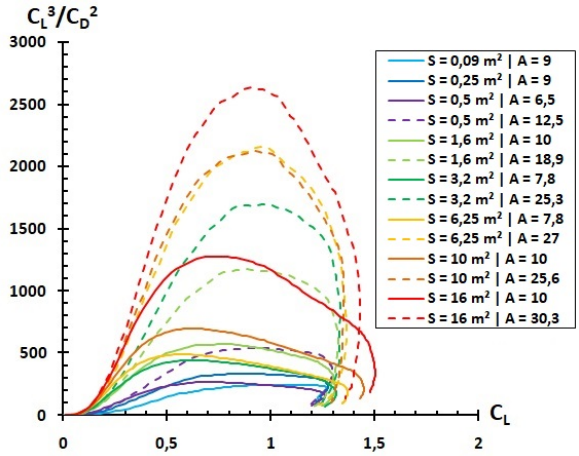

Figure 4.16: Influence of aspect ratio on the lift-to-drag ratio powered by three halves.

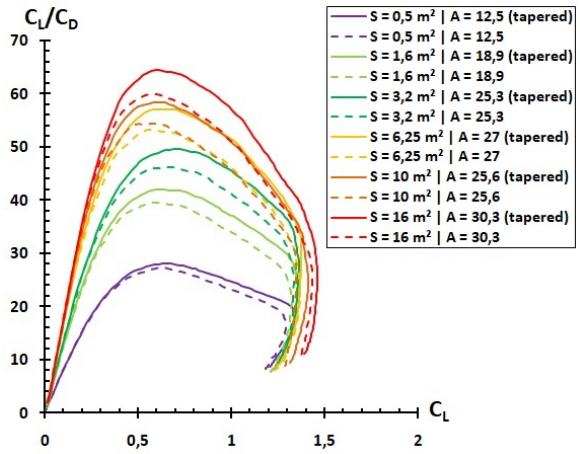

Figure 4.17: Taper ratio influence on the lift-to-drag ratio.

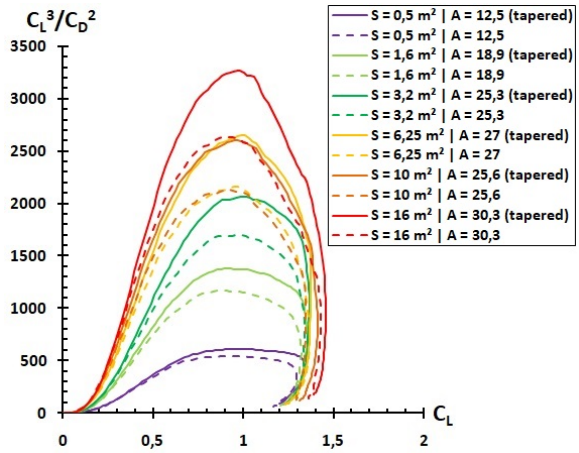

Figure 4.18: Taper ratio influence on the lift-to-drag ratio powered by three halves.

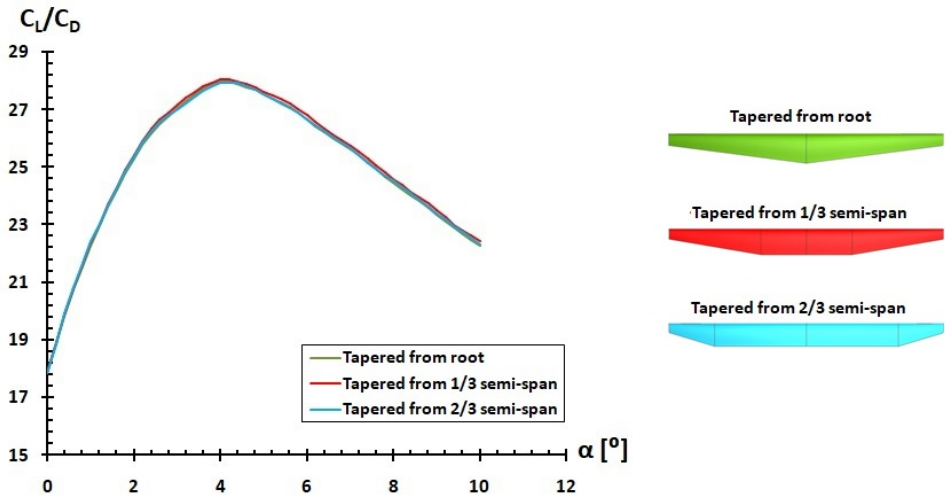

Figure 4.19: Left side: lift-to-drag ratio comparison between different taper configurations for the same wing area, always considering taper 0.4. Right side: planform shape of the different taper configurations considered.

4.2.3 Sweep Angle Selection

Regarding the wing sweep there are some defined angles to take into account. The two most important, for being used upon estimation of other properties, are the maximum thickness line sweep, $\Lambda_{(\frac{t}{c})_{max}}$, and the leading edge sweep, Λ_{LE}. The maximum thickness line sweep is somewhat impractical to use since the maximum thickness line of the wing will depend on the chosen airfoil. Regarding the other defined sweep angles, which may be better visualized in appendix B, and as it is explained D. P. Raymer [6], Λ_{LE} is the angle of concern in supersonic flight, therefore not on the scope of this work, and the quarter-chord sweep, $\Lambda_{\frac{c}{4}}$, is the sweep most related to subsonic flight. The reason for the relation with

the $\frac{c}{4}$ line is because a rectangular wing has its aerodynamic center at approximately the same chord location as the airfoil alone and in subsonic flow this is considered to be at $\frac{c}{4}$ since this is the point where the pitching moment is essentially constant with respect to α for many airfoils. Albeit this assumption may introduce an error in the design, depending on the selected airfoil, it is a generally fair assumption to make in a conceptual design phase.

The main reason for adding leading edge sweep to a wing is to delay and lower the drag rise that occurs when reaching transonic flight speeds, as shown in figure 4.20. In subsonic aircraft usually there is no wing sweep, as figure 4.21 shows, because it does not improve the aerodynamics of the wing and in fact the wing mass increases by adding sweep, according to historical data. As a result, the optimum leading edge sweep for a subsonic UAV is no sweep at all.

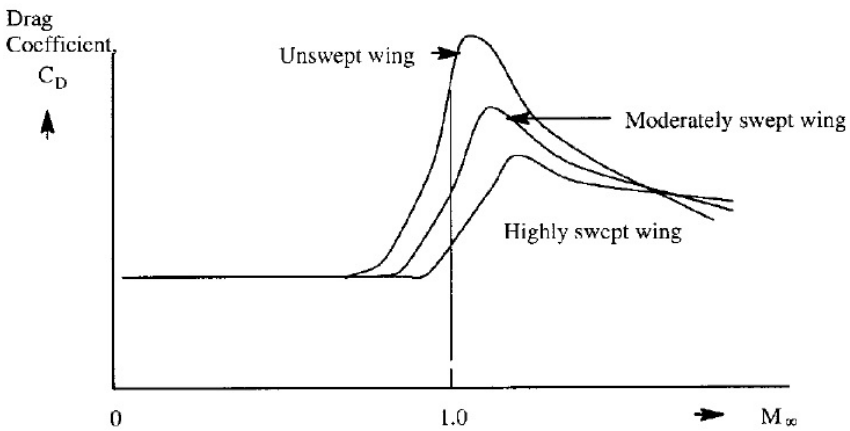

Figure 4.20: Effect of sweep angle on delay of the drag rise [4].

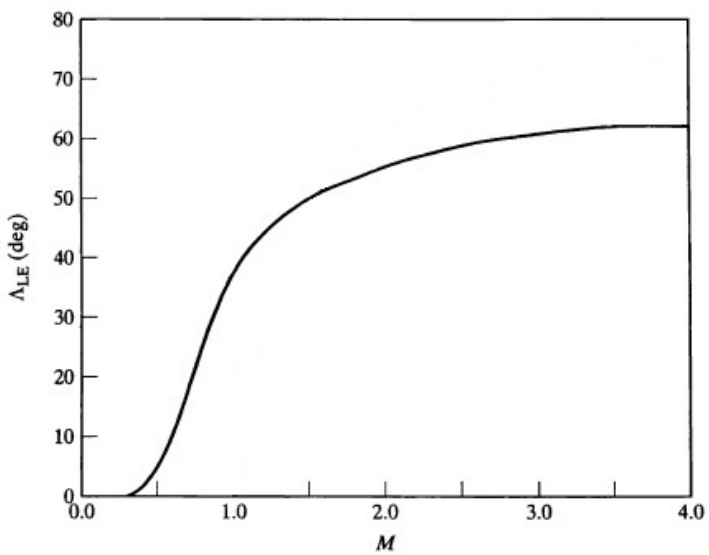

Figure 4.21: Historic data showing values of sweep angle as a function of design Mach number [6].

4.2.4 Drag Estimation

At this stage on the preliminary design of an UAV it is necessary to estimate the overall drag coefficient of the aircraft. To do so, it the necessity comes to determining which formulation to follow and also to provide a value for the zero lift drag coefficient. Different formulations may be considered, albeit some being less conservative than the others due to the efficiency factor computation.

Efficiency Factor

The formulation proposed by T. C. Corke [7] to compute the overall drag coefficient is given by equations 4.15. In this formulation e_f is given by equation 4.15b, where δ is a parameter that corrects the departure of the loading distribution from elliptic as explained by G. R. Spedding and J. McArthur [19]. Also, δ may be taken approximately from figure 4.22.

$$C_D = C_{D_0} + \frac{C_L^2}{\pi A e_f} \tag{4.15a}$$

$$e_f = \frac{1}{1+\delta} \tag{4.15b}$$

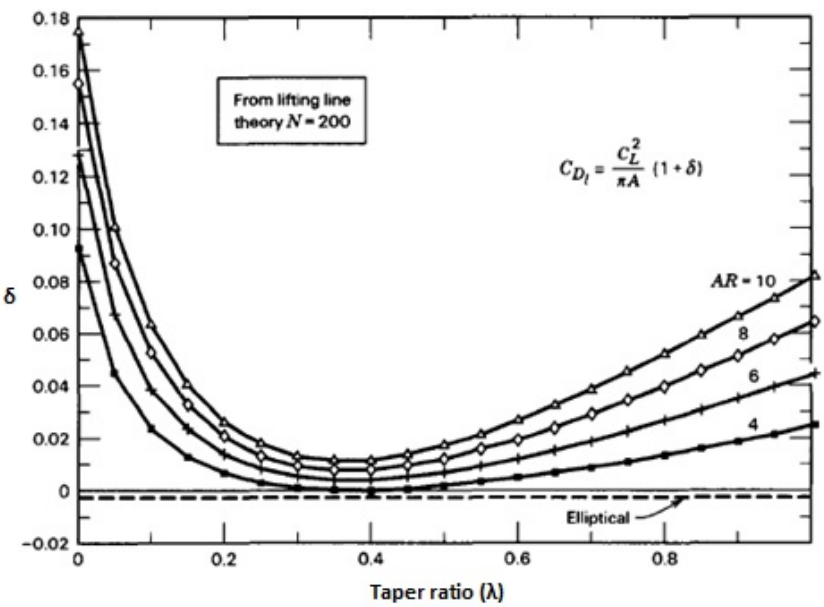

Figure 4.22: Numerical calculation of induced drag factor for linearly tapered and elliptic wings [20].

The problem related with this formulation is that the viscous part of the drag is only accounted for through the value of C_{D_0}, which on an uncambered airfoil is considered to be the value of the zero lift drag coefficient of the airfoil, C_{d_0}, meaning that $C_{D_0} \approx C_{d_0}$. For a cambered airfoil the minimum drag coefficient, $C_{d_{min}}$, is not obtained at zero lift, therefore instead of $C_{D_0} \approx C_{d_0}$ the approach of $C_{D_{min}} \approx C_{d_{min}}$

is used, being $C_{D_{min}}$ the minimum drag coefficient of the wing. This applies also to the remaining formulations here described. The advantage on the other two formulations considered is that they account for the viscous drag in a more conservative fashion, as will be explained.

The other two formulations considered were the one proposed by I. Grosu [21], given by equations 4.16, and another proposed by B. W. McCormick [20], given by equations 4.17 where k is a parameter that corrects the departure from the presumed parabolic shape of the airfoil lift-drag polar. This two equations for C_D can be written in the shape of equation 4.15a using e_f given by equations 4.16b and 4.17b, respectively. In equations 4.16a and 4.16b, t is the airfoil thickness, c is the wing chord and $\frac{t}{c}$ is known as the thickness-to-chord ratio.

$$C_D = C_{D_0} + 0.028\left(\frac{t}{c}\right)_{max} + 1.08\frac{C_L^2}{\pi A} \tag{4.16a}$$

$$e_f = \frac{1}{1.08 + \frac{0.028\,(t/c)_{max}}{C_L^2}\pi A} \tag{4.16b}$$

$$C_D = C_{D_0} + kC_L^2 + \frac{C_L^2}{\pi A}(1+\delta) \tag{4.17a}$$

$$e_f = \frac{1}{1+\delta+k\pi A} \tag{4.17b}$$

Since *k* depends both on the airfoil and on the Reynolds number, Re, analysis were conducted for ten different airfoils, some appropriate for lower Re flyers (as are most of the propeller driven UAV) and other more appropriate for higher Re flyers (as are most of manned aircraft). Also, different Re were considered for estimating *k* to make possible the comparison between the three mentioned formulations. The results of the *k* analysis are provided in appendix C.

In order to compare the different C_D formulations, a study was performed using XFLR5 software to obtain C_L values from three different untwisted rectangular wings corresponding to Re=100k, Re=1M and Re=3M. Afterwords, the obtained C_L values were used to compute C_D using equations 4.15, 4.16 and 4.17. Figure 4.23 shows the results of comparison, where it is possible to observe that both I. Grosu [21] and B. W. McCormick [20] formulations present a more conservative estimate for C_D than the formulation proposed by T. C. Corke [7]. It is important to mention that the vertical displacement between each Re is only for visualization purposes and was achieved by providing each Re with a different value for C_{D_0}. This fact does not influence the evaluation and comparison between each C_D formulation since all of them are dependent of C_{D_0} in the same way and the comparison between them is made within each Re and therefore within the same value for C_{D_0}.

A quick look at figure 4.24 shows that $0.2 \leq C_L \leq 1.2$, approximately, for the realistic angles of attack, meaning, for positive values of α before stall characteristics. Furthermore, the real interesting values

of C_L appear to be around $0.6 \leq C_L \leq 1.1$. Having this in mind and looking back at figure 4.23 it is now straightforward to conclude that, for $0.6 \leq C_L \leq 1.1$, the formulation proposed by [20], given by equation 4.17, is the most conservative of the three. The problem with this formulation is the determination of k.

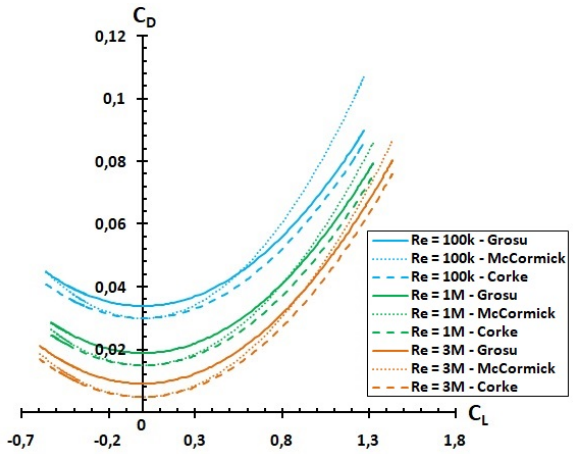

Figure 4.23: Comparison between the presented formulations for estimating the drag coefficient of an aircraft.

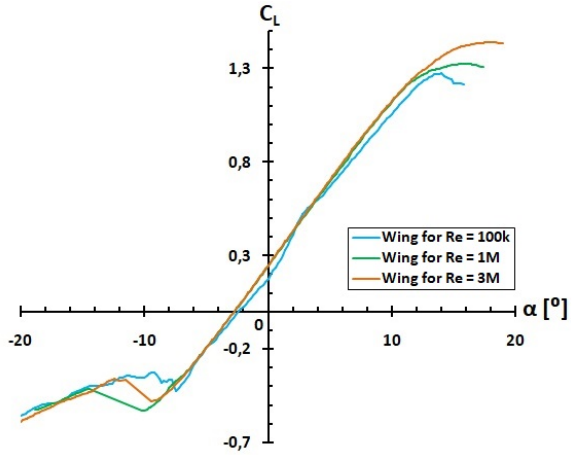

Figure 4.24: Plots of the lift coefficient against the angle of attack for the wings used on the formulations comparison.

Following the line of reasoning presented, the advice is to use the formulation proposed by I. Grosu [21] (equations 4.16), which is better than the alternative proposed by T. C. Corke [7] but at the same time easier to use than the formulation proposed by B. W. McCormick [20]. If choosing a more conservative conceptual design, than the formulation to use is the last mentioned.

After the proposal for a better formulation for the drag coefficient, it is of importance to analyse the problem regarding the zero (or minimum) lift drag coefficient, C_{D_0} or $C_{D_{min}}$.

Zero Lift Drag Coefficient

Despite using a more conservative way of estimating C_D, a problem still resides in the C_{D_0} (or $C_{D_{min}}$) estimate, since the zero lift drag of an aircraft is far from that of the airfoil itself and the drag estimation at this phase is very important because it will then influence the estimate of the needed propulsion power. In this design phase, T. C. Corke [7] proposes $0.01 \leq C_{D_0} \leq 0.02$, as it was empirically proven to be for the majority of manned aircraft. The case is not the same for UAV. As another reference, M. H. Sadraey [5] puts C_{D_0} in the range $0.025 \leq C_{D_0} \leq 0.04$ for small general aviation aircraft with fixed landing gear and for home-built aircraft. Nonetheless, the C_{D_0} range in UAV may be somewhat different, as will be shown.

Figures 4.25 and 4.26 show the results of the study performed to the zero lift drag coefficient parameter and allow for the conclusion that for UAV the range of C_{D_0} values is very different from the proposed for manned aircraft. A closer look puts C_{D_0} approximately in the range $0.005 \leq C_{D_0} \leq 0.08$. From this study it is also noticeable that larger UAV flying at higher Re tend to have a zero lift drag coefficient in

the range proposed for manned aircraft, which is to be expected since their dimensions and operating Re are similar to those of some manned aircraft. It is also important to mention that the same UAV may have different configurations which will lead to different C_{D_0} values. For example, adding a radar dome, special outboard apparatus like antennas, or extra cargo bays below the fuselage, has a significant impact on this parameter. Therefore the range $0.005 \leq C_{D_0} \leq 0.08$ is not to be considered as absolute.

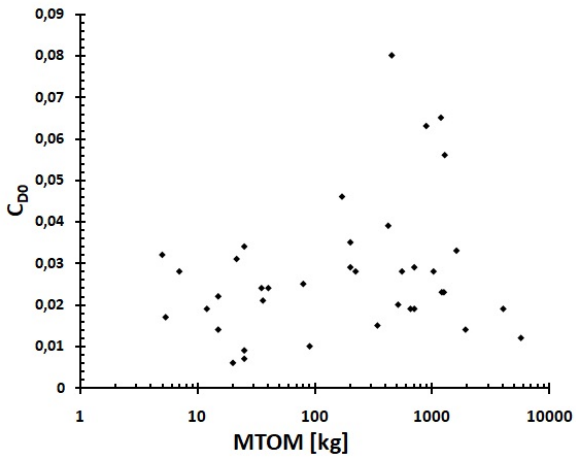

Figure 4.25: Zero lift drag coefficient distribution with the maximum take-off mass, from database.

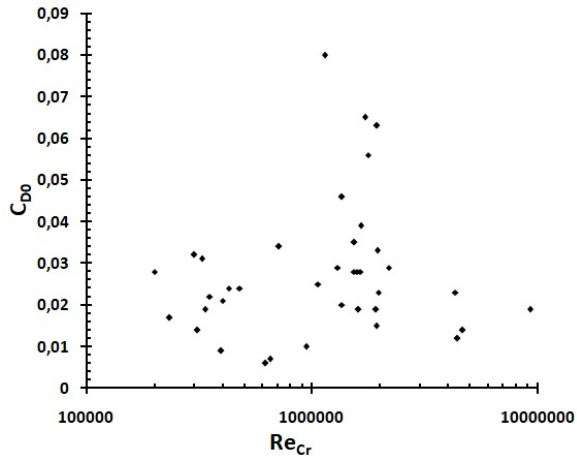

Figure 4.26: Zero lift drag coefficient distribution with the cruise Reynolds, from database.

There is a formulation proposed by T. C. Corke [7] to estimate the C_{D_0} of an aircraft wing based on its geometry. This formulation may be used to estimate the overall zero lift drag coefficient of the aircraft, if used with caution, since the wing should be the main source of drag on an aircraft. The mentioned formulation is given by equation 4.18, where C_f is the friction coefficient, $\mathcal{F}$ is the form factor, $\frac{S_{wet}}{S}$ is the ratio between the wetted or surface area, S_{wet}, of the wing and its planform area, S, and $\mathcal{Q}$ is the interference factor. The friction coefficient is given by equation 4.19 and the form factor is given by equation 4.20, where $(x/c)_{t-max}$ is the chord-wise location of the maximum thickness. The ratio $\frac{S_{wet}}{S}$ is given by equation 4.21 and and the $\mathcal{Q}$ is selected for manned aircraft according to table 4.3.

$$C_{D_0} = C_f \mathcal{F} \mathcal{Q} \frac{S_{wet}}{S} \tag{4.18}$$

$$C_f = \frac{0.455}{(log_{10} Re_{Cr})^{2.58} \left(1 + 0.144 M^2\right)^{0.65}}; \text{ if } \sqrt{Re_{Cr}} \geq 1000 \tag{4.19a}$$

$$C_f = \frac{1.328}{\sqrt{Re_{Cr}}}; \text{ if } \sqrt{Re_{Cr}} < 1000 \tag{4.19b}$$

$$\mathcal{F} = \left[1 + \frac{0.6}{(x/c)_{t-max}} \left(\frac{t}{c}\right)_{max} + 100 \left(\frac{t}{c}\right)^4_{max}\right] \left[1.34 M^{0.18} \left(cos\Lambda_{(\frac{t}{c})_{max}}\right)^{0.28}\right] \tag{4.20}$$

$$\frac{S_{wet}}{S} = 1.977 + 0.52\left(\frac{t}{c}\right)_{max} \tag{4.21}$$

Table 4.3: Interference factor values [7].

Arrangements	$\mathcal{Q}$
Wing mounted nacelle or store	1.5
Wing tip missile	1.25
High wing, mid wing	1
Well filleted low wing	1
Unfilleted low wing	1.25

In most UAV the wing is not the only main source of drag and thus, despite providing a good way of estimating C_{D_0} for manned aircraft, equation 4.18 is not adequate for UAV conceptual design if $\mathcal{Q}$ values from table 4.3 are considered. This conclusion was sustained by a comparison study in which the relative deviation between the real C_{D_0} value and the C_{D_0} value estimated through equation 4.18 was obtained for each UAV. The estimated C_{D_0} were computed according to the following assumptions:

- $\left(\frac{x}{c}\right)_{t-max}$≈0.25, which is common value for many airfoils;
- $\left(\frac{t}{c}\right)_{max}$≈0.14, because it's the value that allows for the highest $C_{L_{max}}$ according to figure 4.6;
- $\Lambda_{(\frac{t}{c})_{max}}$=0, since historically this is the case for aircraft flying below *M*≈0.3, according to figure 4.21;
- $\mathcal{Q}$=1, according to table 4.3.

Notice that the first three assumptions cause the form factor to be larger and thus should be leading to a smaller gap between the real and the estimated C_{D_0}. The relative deviation between real and estimated C_{D_0}, ΔC_{D_0}, is given by equation 4.22 and, after analysis of this parameter, its average was found to be $\Delta\bar{C}_{D_0}$=2.93.

$$\Delta C_{D_0} = \frac{C_{D_{0_{real}}} - C_{D_{0_{est}}}}{C_{D_{0_{real}}}} \tag{4.22}$$

Knowing the average C_{D_0} deviation, $\Delta\bar{C}_{D_0}$, it is now straightforward to conclude that it could represent a value for interference factor to be applied to UAV conceptual design. The proposal is then to consider $\mathcal{Q} = 3$. Notice that C_{D_0} computed considering $\mathcal{Q}$=3 can lead to $C_{D_{0_{est}}} > C_{D_{0_{real}}}$, which poses no problem in this design phase because it presents a conservative estimate. On the other hand, if it leads yet to $C_{D_{0_{est}}} < C_{D_{0_{real}}}$, it is still a more conservative estimate than one which considers $\mathcal{Q}$ values from table 4.3.

4.3 Fuselage Design

The fuselage design of an UAV does not follow an established approach. Albeit there are methodologies for the fuselage conceptual design of a manned aircraft, those are not fit for UAV since UAV do not need to fit passengers inside. Instead, on the conceptual design of an UAV the interior volume of the fuselage is designed to meet storage needs. The essential space inside every UAV fuselage is that enough to store all the electronics. Also, for UAV with interior payload capacity, a cargo bay is also needed. Thus, the two main parts of the fuselage interior in an UAV are the electronics bay (or compartment) and the cargo bay. With this in mind, the fuselage design of an UAV may be performed with mainly two considerations:

1. Space needed for accommodating system components and payload;
2. Fuselage drag.

The goal is to design a fuselage that can fit everything inside and that causes low drag, thus providing a lower overall drag coefficient, $C_{D_{total}}$. Following the approach given by T. C. Corke [7], the fuselage drag coefficient, $C_{D_{fus}}$, may be estimated according to equations 4.23 and 4.24, where $\frac{d}{\ell}$=$\frac{d_{max}}{\ell_{fus}}$ is the fineness ratio.

$$C_{D_0} = C_f \mathcal{F} \mathcal{Q} \frac{S_{wet}}{S} \tag{4.23}$$

$$\mathcal{F} = 1 + 60 \times \left(\frac{d}{\ell}\right)^3 + \frac{1}{400 \times \left(\frac{d}{\ell}\right)} \tag{4.24}$$

Focusing on equation 4.23 it is possible to notice that it returns C_{D_0} instead of C_D. This is not a mistake, instead it is explained simply because when estimating the fuselage drag coefficient a lift-induced component is not considered. And this is a good approach because for many aircraft the fuselage is a non-cambered body (meaning, a body that has a mirrored design regarding its central axes) and, aerodynamically speaking, a non-cambered body, when aligned with the airflow, does not create a pressure gradient when under flow, resulting in a null lifting force.

In many UAV the fuselage is not exactly non-cambered and therefore the lift provided by the fuselage is not null. Despite that, the above mentioned approach may apply to UAV because even for cambered fuselages the lift produced is neglectable when compared to the lift produced by the wing.

Now, from equations 4.23 and 4.24 it is possible to see the influence of the fineness ratio on $C_{D_{fus}}$. Also, for subsonic aircraft the relation between the overall zero lift drag coefficient $C_{D_{0_{total}}}$ (which is the sum of the C_{D_0} given by each component of the aircraft) and the fuselage fineness ratio may be observed in figure 4.27, where the black mark showing how to measure d and ℓ intents to represent the side view of a fuselage.

From figure 4.27 it is possible to see that the fineness ratio which minimizes the overall drag coefficient is $\frac{d}{\ell}$≈0.3. Also, the $\frac{d}{\ell}$ for subsonic passenger aircraft is around $\frac{d}{\ell}$≈0.1 [7], which is very far from the optimum $\frac{d}{\ell}$.

The fineness ratio was computed for the UAV in the database using the fuselage length, ℓ_{fus}, and the equivalent maximum diameter, d_{max}, computed as previously explained in section 2.2. Figure 4.28 shows $\frac{d}{\ell}$ for each UAV and it is possible to observe that for UAV with a boom mounted tail (BMT) the fineness ratio is closer to the optimum ($\frac{d}{\ell}$≈0.3) than for UAV with fuselage mounted tail (FMT) configuration. This has a logical explanation since for two aircraft with the same overall length, ℓ_{Total}, and same d_{max}, one with BMT and the other with FMT, the fuselage length is larger in the second aircraft. As a consequence $\frac{d}{\ell}$ will be lower on the FMT aircraft than on the BMT aircraft. For a quick configuration check please consider appendix A.

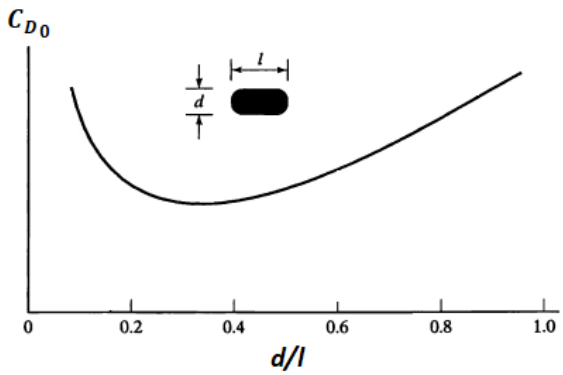

Figure 4.27: Evolution of the overall drag coefficient with the fineness ratio for subsonic aircraft [7].

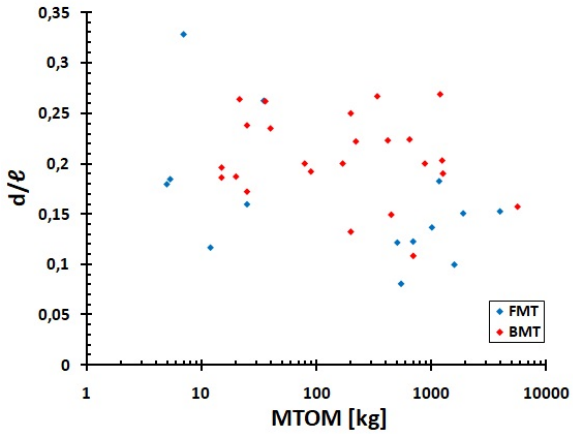

Figure 4.28: Fineness ratio against maximum take-off mass, differing by tail mount configuration, from database.

Having in mind the goal for UAV performance optimization, which reflects upon minimizing the drag coefficient of the vehicle, the conclusion to be taken from this section is that a BMT configuration is better than a FMT configuration.

4.4 Tail Design

The tail conceptual design rests basically upon estimating the position of the horizontal and vertical tails, in respect to the main wing aerodynamic center, and their respective areas, S_{HT} and S_{VT}. This is performed based on wing data such as the span, b, the mean aerodynamic chord, $\bar{c}$, and the area, here represented by S_W to avoid confusion.

In order to understand if the values proposed in the literature [5, 7] for the horizontal and vertical tail size coefficients, C_{HT} and C_{VT}, and the length ratio, $\frac{\ell_T}{\ell_{Total}}$, apply to the conceptual design of UAV,

the necessity came to determining these properties for the UAV presented in the database. In order to do so, the areas of the horizontal and vertical tails were obtained from manufacturer data along with the fuselage length, ℓ_{fus} (which is different from the total aircraft length, ℓ_{Total}, in the case of UAV with BMT), and the length between the wing aerodynamic center and the tail aerodynamic center, ℓ_T.

4.4.1 Length Ratio

The use for a tail on an aircraft is to create moments about the aircraft Centre of Gravity (CG) in order to provide control and stability over the lateral and vertical axis, defined in appendix B. The horizontal tail affects the control over the lateral axis whereas the vertical tail affects the control over the vertical axis. The length ratio is not dependent on the shape of the tail because two tails with different shapes placed at the same distance and having the same airfoil and planform area provide equal moments about the lateral and vertical axis. Consequently, the commitment for selecting a value for $\frac{\ell_T}{\ell_{Total}}$ is then between the restriction of fuselage length, when considering an UAV with FMT, or overall length and the goal for flight efficiency, which translates into drag reduction.

If a larger $\frac{\ell_T}{\ell_{Total}}$ ratio is chosen, the tail will rest further away from the wing and the aircraft CG than if choosing a smaller $\frac{\ell_T}{\ell_{Total}}$ ratio. This directly reflects on the tail size because, for the same moment about the CG, increasing the distance implies a reduction on the horizontal tail planform area. A reduction on the tail size implies a reduction on the induced drag, meaning that the aircraft overall drag will be reduced.

For the analysis of the length ratio performed to the UAV in the database one basic assumption was made, after inspection of the exemplars, which was that the aerodynamic centers of the horizontal and vertical tails are in the same position (ℓ_{VT}=ℓ_{HT}=ℓ_T). This assumption may seem abusive, but it is a rather plausible assumption to make because it is true for a large number of UAV since most of them have V, A or H shaped tails. Even for some cases where the vertical and horizontal tails aerodynamic centers are not vertically aligned, the error introduced upon making this assumption for the general case it's neglectable in this conceptual design phase.

Since the aerodynamic center is considered to be placed at 25% of the chord, as explained previously in section 4.2, the length between the wing aerodynamic center and the tail aerodynamic center, ℓ_{VT} for the vertical tail and ℓ_{HT} for the horizontal tail, is defined as shown in figures B.3 and B.2 in appendix.

The ratio $\frac{\ell_T}{\ell_{Total}}$ was computed for each of the UAV in the database and the result can be seen in figure 4.29, where the different engine positioning configurations represented through their respective acronym are the ones already introduced in chapter 2 and are also described in appendix A.

The length ℓ_T is tabulated, by means of the ratio $\frac{\ell_T}{\ell_{fus}}$, for some aircraft configurations, as seen in table 4.4 [7], which shows that, as it was to be expected, different configurations regarding engine position are bound with different $\frac{\ell_T}{\ell_{Total}}$ ratios. Despite the suggested classes only differing aircraft by front, wing or

fuselage mounted engines, it is possible to find more classes applied to UAV design. Notice that, in table 4.4, fuselage mounted engines refers to having the engine(s) placed on the fuselage, commonly near the tail or after the tail. Table 4.5 shows the defined UAV classes, regarding engine positioning, and their respective proposed ranges for the $\frac{\ell_T}{\ell_{Total}}$ ratio are presented. The proposed ranges are in accordance with those that may be seen in figure 4.29.

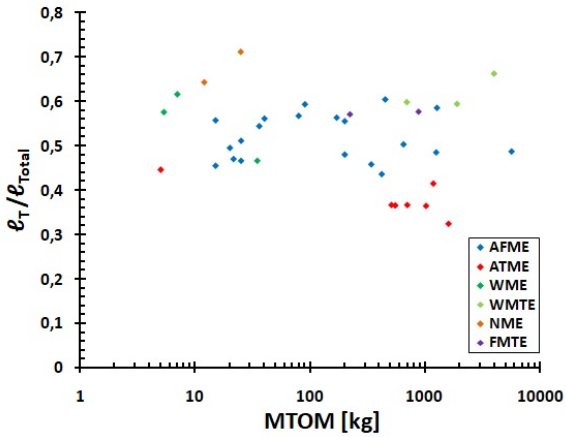

Figure 4.29: Length ratio for different engine positioning configurations.

Table 4.4: Length ratio range for different engine position configurations [7]

Engine configuration	ℓ_T/ℓ_{Total}
Fuselage-mounted engine	0.45 - 0.5
Wing-mounted engines	0.5 - 0.55
Front-mounted prop	0.6

Table 4.5: Length ratio range proposed for unmanned aerial vehicles regarding different engine position arrangements.

Engine configuration	ℓ_T/ℓ_{Total}
Aft tail mounted engine	0.3 - 0.45
Aft fuselage mounted engine	0.4 - 0.6
Fuselage mounted twin engines	0.55 - 0.6
Wing mounted engine(s)	0.55 - 0.65
Nose mounted engine	0.6 - 0.7

4.4.2 Tail Size Coefficients

The horizontal and vertical tail size coefficients, C_{HT} and C_{VT}, are used for estimating the areas of the horizontal and vertical tails when doing the conceptual design of an aircraft, as shown in equations 4.25 an 4.26.

$$S_{HT} = C_{HT}\frac{\bar{c}S_W}{\ell_{HT}} \tag{4.25}$$

$$S_{HT} = C_{VT}\frac{bS_W}{\ell_{VT}} \tag{4.26}$$

Tail size coefficients are tabulated for manned aircraft with conventional tails and different types of mission [7]. For different tail shapes there are also corrective factors to be multiplied by the size coefficients given for conventional tail aircraft. Table 4.6 then shows the horizontal tail size coefficients as proposed by T. C. Corke [7] for different tail shapes and airplane classes. It is possible to see that larger MTOM aircraft, as in the classes General Aviation (twin engine), Twin turboprop, Military Transport/Bomber and Commercial Jet Transport, have higher C_{HT} and C_{VT} values, $0.8 \leq C_{HT} \leq 1.0$ and $0.07 \leq C_{VT} \leq 0.09$. Also, aircraft with requirements for high maneuverability, as in the classes Combat Jet Trainer and Combat Jet Fighter, have higher C_{VT} values, $0.06 \leq C_{VT} \leq 0.07$, as it is to be expected. Another interesting conclusion coming from table 4.6 is that the shape of the tail has almost no effect on the tail size coefficients, which is logically explained since what matters is the tail airfoil, planform area and distance from the aircraft CG, as previously explained.

Although the values on table 4.6 may be suited for manned aircraft, they are not suited to be considered upon the conceptual design of UAV. With the purpose of finding better suited values, the C_{HT} and C_{VT} coefficients were computed for each aircraft on the database and then compared with other parameters.

Table 4.6: Tail size coefficients for different aircraft and tail configurations [7].

Aircraft Class	**Tail Configuration**							
	Conventional		T-tail		V or A tail		H-tail	
	C_{HT}	C_{VT}	C_{HT}	C_{VT}	C_{HT}	C_{VT}	C_{HT}	C_{VT}
Sail Plane	0.5	0.02	0.475	0.019	0.5	0.02	0.475	0.02
Homebuilt	0.5	0.04	0.475	0.038	0.5	0.04	0.475	0.04
General Aviation (single engine)	0.7	0.04	0.665	0.038	0.7	0.04	0.665	0.04
General Aviation (twin engines)	0.8	0.07	0.76	0.0665	0.8	0.07	0.76	0.07
Twin Turboprop	0.9	0.08	0.855	0.076	0.9	0.08	0.855	0.04
Combat Jet Trainer	0.7	0.06	0.665	0.057	0.7	0.06	0.665	0.03
Combat Jet Fighter	0.4	0.07	0.38	0.0665	0.4	0.07	0.38	0.035
Military Transport/Bomber	1.0	0.08	0.95	0.0931	1.0	0.08	0.95	0.04
Commercial Jet Transport	1.0	0.09	0.95	0.0855	1.0	0.09	0.95	0.045

Horizontal tail size coefficient

Focusing on finding out what influences the horizontal tail size coefficient, C_{HT}, first it is necessary to establish equation 4.27. Also, it is important to bear in mind the assumption made on the beginning of section 4.4.1. Using equation 4.27, the C_{HT} value was computed for each UAV in the database.

$$C_{HT} = \frac{\ell_T S_{HT}}{\bar{c} S_W} \tag{4.27}$$

A closer look at figures 4.30 and 4.31 allows for the conclusion that C_{HT} assumes a wide range of values which may be set at approximately $0.1 \leq C_{HT} \leq 1.3$. This poses a big difference from the C_{HT}

range shown in table 4.6, which means that it is already justifiable to state that the C_{HT} proposed by T. C. Corke [7] do not apply to the majority of UAV. The next step is to evaluate C_{HT} as a function of MTOM regarding engine positioning and tail configuration. Regarding the tail configuration, as figure 4.31 shows, there is not room for much considerations because albeit the appearance of some clusters of points, the C_{HT} range associated is wide. From figure 4.30 it is possible to see a clear influence of the engine positioning on C_{HT}. Firstly, the UAV with Wing Mounted Engine(s) (WME or WMTE) are all in the $0.3 \leq C_{HT} \leq 0.65$. Also, UAV with Nose Mounted Engine (NME) clearly tend to have $C_{HT} \simeq 0.6$. Furthermore, another class is identifiable for UAV with Aft Tail Mounted Engine (ATME) which is $0.7 \leq C_{HT} \leq 0.8$, with one apparent exception which corresponds to the Hermes 450 UAV. This difference is explained fairly by comparing this aircraft with one with the same engine positioning and with similar MTOM, such as the GNAT 750.

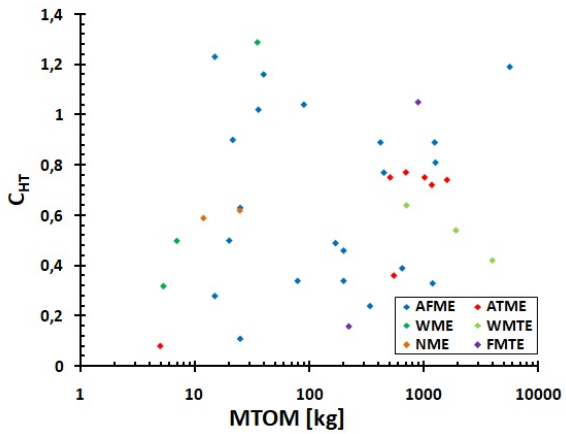

Figure 4.30: Horizontal tail size coefficient distribution with the maximum take-off mass for the different engine positioning configurations referenced in appendix A. Taken from the database.

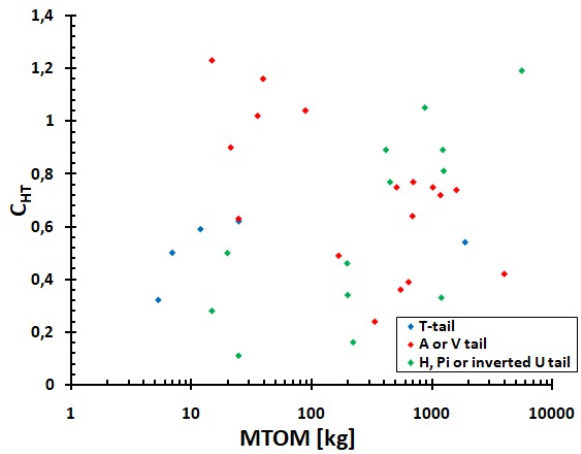

Figure 4.31: Horizontal tail size coefficient distribution with the maximum take-off mass for the different tail configurations referenced in appendix A. Taken from the database.

By inspection of figure 4.32 it becomes clear that the Hermes 450 presents a bigger ℓ_T and wing area whilst the GNAT 750 presents a bigger aspect ratio and horizontal tail area, S_{HT}. In fact, the Hermes 450 presents $S_W \simeq 7.7m^2$, $A \simeq 14.3$, $\ell_T \simeq 2.23m$ and $S_{HT} \simeq 0.91m^2$, whilst the GNAT 750 presents $S_W \simeq 5.9m^2$, $A \simeq 19.6$, $\ell_T \simeq 1.95m$ and $S_{HT} \simeq 1.25m^2$. Since C_{HT} may be written like in equation 4.28, the comparison between the two aircraft in terms of C_{HT} is given by equation 4.29, which basically shows that the Hermes 450 C_{HT} is about half of the GNAT 750 C_{HT}, just like figure 4.30 demonstrates. A curious fact shown by table 4.6 is that C_{HT}=0.4 is the proposed value for jet fighters and C_{HT}=0.7, which corresponds to the ATME category on figure 4.30, is the proposed value for a range of classes shown in table 4.6. This may suggest that the Hermes 450 was an experiment regarding the tail size.

$$C_{HT} = \frac{\ell_T S_{HT} A}{b S_W} \tag{4.28}$$

$$\frac{[C_{HT}]_{Hermes450}}{[C_{HT}]_{GNAT750}} = \frac{\left[\frac{\ell_T S_{HT} A}{b S_W}\right]_{Hermes450}}{\left[\frac{\ell_T S_{HT} A}{b S_W}\right]_{GNAT750}} = \frac{\frac{2.23\times0.91\times14.3}{10.5\times7.7}}{\frac{1.95\times1.25\times19.6}{10.8\times5.9}} \simeq 0.48 \tag{4.29}$$

Figure 4.32: Size comparison between Hermes 450 and GNAT 750 unmanned aerial vehicles.

Since the horizontal tail size coefficient is directly proportional to the wing aspect ratio of the aircraft, as shown in equation 4.28, the necessity came to determining whether or not the A is a good tool to help estimate the right C_{HT} to use in the preliminary design of an UAV. For that purpose, the plots presented on figures 4.33 and 4.34 were computed. A quick look at these figures shows that C_{HT} grows with the wing aspect ratio, as expected. On the other hand, a closer look at figure 4.33 shows a clear division regarding the A for UAV with Aft Fuselage Mounted Engine (AFME). Albeit one exception with $C_{HT}\simeq0.4$ and A=15, it is straightforward to state that for this UAV category $0.1\leq C_{HT}\leq0.6$, for $A<11$, and $0.8\leq C_{HT}\leq1.2$, for $A>11$. The mentioned exception corresponds to the Bayraktar UAV and the reason for it falling out of the range proposed may be explained in the same way as the previously mentioned case of the Hermes 450 UAV.

Another interesting implication arises from the plotting C_{HT} against the A for the two main tail categories defined, Boom Mounted Tail (BMT) and Fuselage Mounted Tail (FMT), as it is shown in figure 4.34. In fact, a quick observation allows to determine right away that for each category there are two major groups of dots with different C_{HT} ranges. FMT UAV with $A<16$ have $0.3\leq C_{HT}\leq0.6$ and for the cases with $A>16$ the C_{HT} range is $0.6\leq C_{HT}\leq0.8$. On the other hand, BMT UAV with $A<11$ have $0.1\leq C_{HT}\leq0.65$ whereas for the cases with $A>11$ the C_{HT} range is $0.75\leq C_{HT}\leq1.2$. The only exception to the previously established is the above mentioned case of the Bayraktar UAV.

Finally, table 4.7 shows the proposed C_{HT} ranges to be applied in UAV conceptual design, regarding different engine positioning configurations. Nonetheless, it is important to understand that this values

are not absolute, in fact the tail size coefficients are somewhat a designers choice. In order to empirically guide the designer on the C_{HT} selection a new approach was developed and will be presented next.

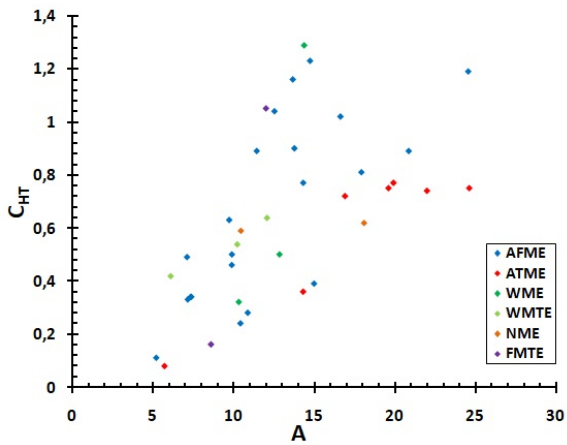

Figure 4.33: Horizontal tail size coefficient versus wing aspect ratio for different engine positioning configurations, from database.

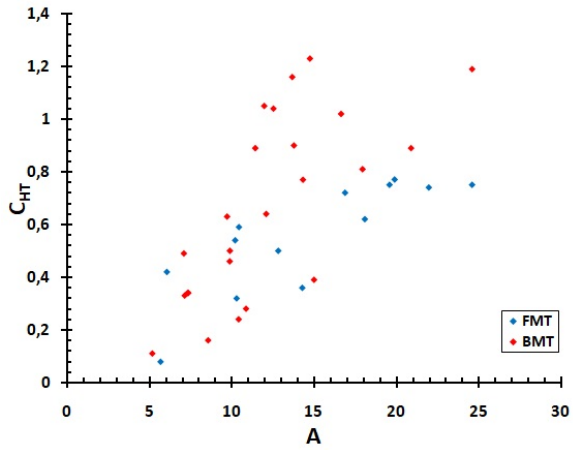

Figure 4.34: Horizontal tail size coefficient versus wing aspect ratio, focusing on the difference between boom-mounted tails and conventional aft tails.

Table 4.7: Horizontal tail size coefficient range proposed for different engine position configurations.

Engine Position	C_{HT}
Wing Mounted Engine (WME)	0.3 - 0.65
Nose Mounted Engine (NME)	0.6
Aft Tail Mounted Engine (ATME)	**A<16:** 0.3 - 0.6 | **A≥16:** 0.6 - 0.8
Aft Fuselage Mounted Engine (AFME)	**A<11:** 0.1 - 0.65 | **A≥11:** 0.75 - 1.2

When studying the effect of some aircraft parameters on the horizontal tail size coefficient, a new approach was developed for its determination. This approach applies only to UAV, since it has been based on UAV data only.

First, knowing that C_{HT} has a direct relation with the ratio $\frac{\ell_T}{\bar{c}}$, as shown in equation 4.27, the idea was to graphically relate the two parameters, the result of which may be observed in figure 4.35. Then, figure 4.36 provides a relation between the ratio $\frac{\ell_{Total}}{b}$ and the wing aspect ratio, A. Considering the linear regressions presented on the mentioned figures, the approach developed is as follows.

1. With the wing A find the $\frac{\ell_{Total}}{b}$ ratio for the UAV in project through the linear relation presented in figure 4.36 and reflected in equation 4.30.
$$\frac{\ell_{Total}}{b} = -0.015A + 0.8 \tag{4.30}$$
2. Multiply the obtained $\frac{\ell_{Total}}{b}$ ratio by the wing span, b, to obtain the aircraft total length, ℓ_{Total}.
3. From table 4.5 choose the $\frac{\ell_T}{\ell_{Total}}$ ratio that best fits the configuration of the UAV in project.
4. Multiply the chosen $\frac{\ell_T}{\ell_{Total}}$ ratio by ℓ_{Total} to obtain ℓ_T.

5. Knowing the wing mean aerodynamic chord, $\bar{c}$, compute the ratio $\frac{\ell_T}{\bar{c}}$

6. With the computed $\frac{\ell_T}{\bar{c}}$ ratio find C_{HT} for the UAV in project through the linear relation presented in figure 4.35, where m.a.c stands for the mean aerodynamic chord, $\bar{c}$, and reflected in equation 4.31.

$$C_{HT} = 0.2\frac{\ell_T}{\bar{c}} - 0.15 \tag{4.31}$$

Furthermore, the relative error, as defined in equation 4.32, on the C_{HT} computed using the above mentioned approach is below 20% for the majority of UAV on the database. This shows that the approach may be utilized without compromising the conceptual design of the UAV. Also, on this design phase the idea is to apply a relatively good value for C_{HT} and therefore there is no need for a more accurate C_{HT} prediction.

$$Error(\%) = \frac{\mid C_{HT_{computed}} - C_{HT_{approach}} \mid}{C_{HT_{computed}}} \tag{4.32}$$

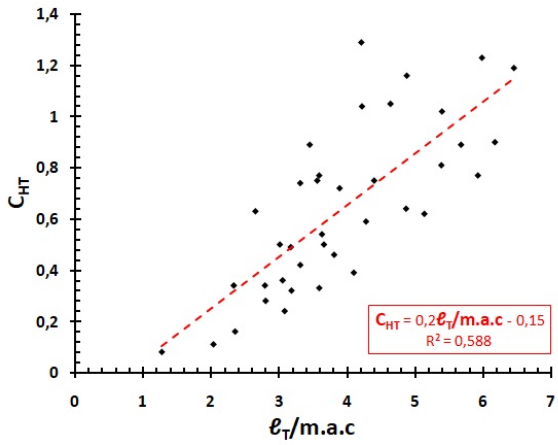

Figure 4.35: Horizontal tail size coefficient against the tail position over wing mean aerodynamic chord ratio, from database.

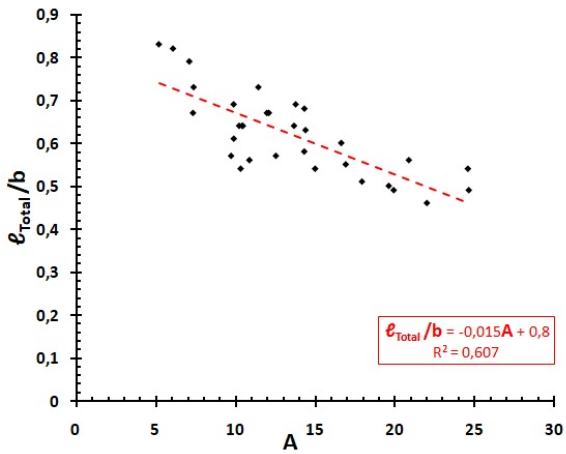

Figure 4.36: Total length over span ratio against wing aspect ratio, from database.

Vertical tail size coefficient

Focusing now on finding out what influences the vertical tail size coefficient, C_{VT}, it is necessary to establish equation 4.33 and, again, to keep in mind the assumption made on the beginning of section 4.4.1. Furthermore, the size of the vertical tail, albeit a minimum necessary for stability, is mainly influenced by the amount of yaw agility the designer wants for the aircraft.

$$C_{VT} = \frac{\ell_T S_{VT}}{b S_W} \tag{4.33}$$

By means of equation 4.33, the C_{VT} value was computed for each UAV in the database and fig-

ures 4.37 and 4.38 show the distribution of C_{VT} with MTOM, exploring the different defined classes regarding engine positioning and tail configuration. By inspection of these figures it is straightforward to conclude that C_{VT} assumes a wide range of values, just like C_{HT}, that may be set at approximately $0.01 \leq C_{VT} \leq 0.075$. This poses a big difference from the C_{VT} range shown in table 4.6, therefore it is possible to conclude that the C_{VT} values proposed in the literature are not the best fitted to UAV conceptual design.

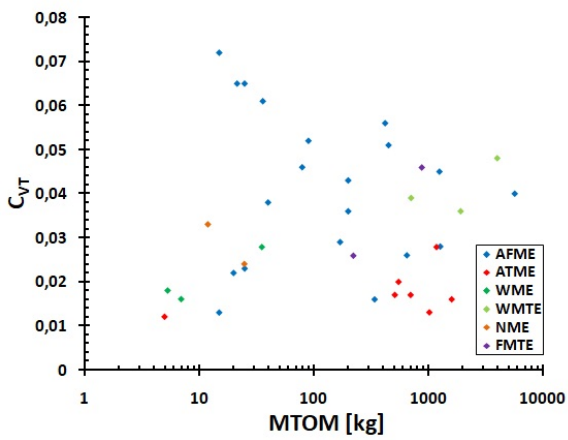

Figure 4.37: Vertical tail size coefficient distribution with the maximum take-off mass for different engine positioning configurations, from database.

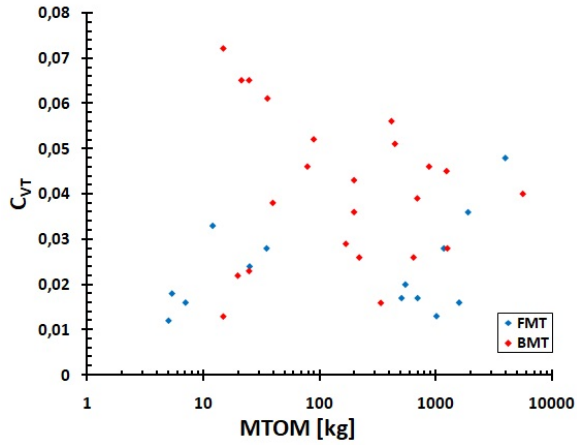

Figure 4.38: Vertical tail size coefficient distribution with the maximum take-off mass for different tail configurations, from database.

When trying to evaluate C_{VT} as a function of MTOM regarding engine positioning, figure 4.37, and tail configuration, figure 4.38, there is not much that can be said. Nonetheless, from figure 4.38 it is possible to notice that C_{VT} for UAV with BMT is within $0.01 \leq C_{VT} \leq 0.075$, approximately, and for UAV with FMT is within $0.01 \leq C_{VT} \leq 0.05$, approximately. One explanation for this might be the fact that for UAV with BMT there is not a limit for ℓ_T imposed by the fuselage. On the other hand, from figure 4.37, it is possible to see that for UAV with ATME $0.01 \leq C_{VT} \leq 0.03$ approximately and for UAV with Wing Mounted Twin Engines (WMTE) $0.01 \leq C_{VT} \leq 0.03$. For better understandment of the different configurations here discussed, visual references are presented in appendix A.

It is of importance to mention that different relations were tested with the goal of finding a better way for estimating C_{VT}, nonetheless neither of the attempts revealed a clear relation. As mentioned above the vertical tail size coefficient is not that important for the overall conceptual design of an aircraft, therefore the suggestion is to use C_{VT}=0.035 as a first estimate when doing the conceptual design of an UAV. This value corresponds to the average C_{VT} on the UAV studied.

4.5 Verification of the Proposed Adaptations

In order to validate the proposed adaptations to the conceptual design methodology, three UAV were selected from the database and the conceptual design methodology, along with the proposals made on the previous sections of chapter 4, were applied. The goal was to prove that by following the proposals made in this chapter, based on performance requirements, the resulting aircraft would be very similar, thus verifying the adapted methodology. The UAV were selected from different weight classes so to prove the viability of the presented solutions. The chosen exemplars were the Predator, manufactured by General Atomics and shown in figure 4.39, the Hermes 450, manufactured by Elbeit Systems and shown in figure 4.40, and the Ogassa, manufactured by UAVision Aeronautics and shown in figure 4.41. Table 4.8 shows the requirements considered for computing the aircraft properties and in table 4.9 the computed properties of the aircraft are presented. Notice that in table 4.8 there is no stall speed, V_S for Hermes 450 because that data could not be found.

Figure 4.39: Predator, General Atomics.

Figure 4.40: Hermes 450, Elbeit Systems.

Figure 4.41: Ogassa, UAVision Aeronautics.

Table 4.8: Aircraft requirements for verifying the proposed methodology adaptations.

Parameter	Predator	Hermes 450	Ogassa
MTOM [kg]	1020	550	36
Payload [kg] for max. E	185	45	5
Max. E [h]	24	30	8
V_S [m/s]	27.7	-	19.55
V_{Cr} [m/s]	37.55	36.2	25.72
V_D [m/s]	52.3	48.7	41.2
Ceiling [ft]	25000	18000	6500

Table 4.9: Computed properties of the aircraft selected for verifying the proposed methodology adaptations.

Parameter	Predator	Hermes 450	Ogassa
S_W [m^2]	11.54	7.95	1.01
b [m]	16.8	10.5	4.2
A	24.46	13.87	17.46
P [kW]	85.37	39.9	4.99
$\ell_T[m]$	2.95	2.4	1.329
Equivalent S_{HT} [m^2]	2.07	0.874	0.194
Equivalent S_{VT} [m^2]	0.85	0.67	0.195

In order to determine whether or not the resulting aircraft properties on table 4.9 are close to the

real values, a comparison was established between the results presented this table and the values considered for each property in the database, which are summoned in table 4.10.

Table 4.10: Relevant properties of the aircraft selected for verifying the proposed methodology adaptations.

Parameter	Predator	Hermes 450	Ogassa
S_W [m^2]	11.455	7.7	1.06
b [m]	16.8	10.5	4.2
A	24.64	14.32	16.64
P [kW]	84.5	39	5.22
$\ell_T[m]$	3.0	2.234	1.362
Equivalent S_{HT} [m^2]	1.947	0.912	0.2
Equivalent S_{VT} [m^2]	0.853	0.714	0.2

By inspection of tables 4.9 and 4.10 it is possible to observe the proximity between the computed values and the real ones. The values could never be exactly the same since in the conceptual design steps there are certain parameters which are left for the designer to select their values and it is not possible to know which values were considered by the manufacturers upon the design of each UAV. Since the same set of requirements can lead to entirely different aircraft configurations, depending on the designers choices, the span of each UAV was chosen to be the same as the value on the database, simply because to verify the methodology it was necessary to select either the span or the aspect ratio to remain equal to the database value, otherwise the resulting aircraft could be entirely different.

To better visualize the magnitude of the differences between the database values and the computed ones, the relative error was computed for each property, other than b, based on equation 4.34, where $X_{database}$ represents the database property value and $X_{computed}$ represents the computed property value. Furthermore, figure 4.42 presents the relative error, in percentage, for each of the mentioned properties.

$$\text{Error} = \frac{|X_{database} - X_{computed}|}{X_{database}} \tag{4.34}$$

In the first three parameters, S_W, A and P, the result observable in figure 4.42 showing the higher errors associated to Ogassa, the intermediate to Hermes 450 and the lower to Predator, is to be expected. The reason for this fact is justified by the difference of mass class between the three UAV. Higher MTOM values usually imply bigger wing areas, higher aspect ratios and more powerful propulsion systems. With this in mind, it is very expectable to find higher relative errors in this three properties lowering the MTOM, despite the small differences in the values associated with this parameters.

As for the two last parameters, S_{HT} and S_{VT}, figure 4.42 shows the highest relative error at about 6$\%$ for both, nonetheless, by inspection of tables 4.10 and 4.9 this errors become insignificant. For the S_{HT} the highest error is of about 6.3$\%$ for Predator's horizontal tail, which represents a difference of 0.123m^2 in a real area of almost 2m^2. As for the S_{VT}, the highest error is of about 6.2$\%$ for the vertical tail of Hermes 450, representing a difference of only 0.044m^2 in a real area of nearly 0.7m^2.

The highest relative error presented in figure 4.42 is 7.43% and it is related to the tail positioning of Hermes 450, through ℓ_T. A quick inspection back at tables 4.10 and 4.9 allows for the conclusion that the database ℓ_T value for this aircraft is 2.234m while the computed value is 2.4m, meaning that the difference between them represents less than 0.2m. A difference of 0.2m in an aircraft with a real overall length of 6.1m would represent a forward displacement of the wing of about 3.28%, which would be almost imperceptible on a first glance and would also be neglectable performance-wise.

Furthermore, the methodology proposed is to be used for the conceptual design of UAV and the results obtained in a conceptual design phase may not be the same as in a later detailed design phase. With this in mind, an error of 7.43% is deemed acceptable. Also, as previously explained, the conceptual design phase suits the purpose for a not that detailed first design of an aircraft, therefore the proposed methodology and adaptations may well be used.

Having all this in consideration it becomes clear that the proposed adaptations to the methodology do apply to the conceptual design of unmanned aerial vehicles, and are thus verified.

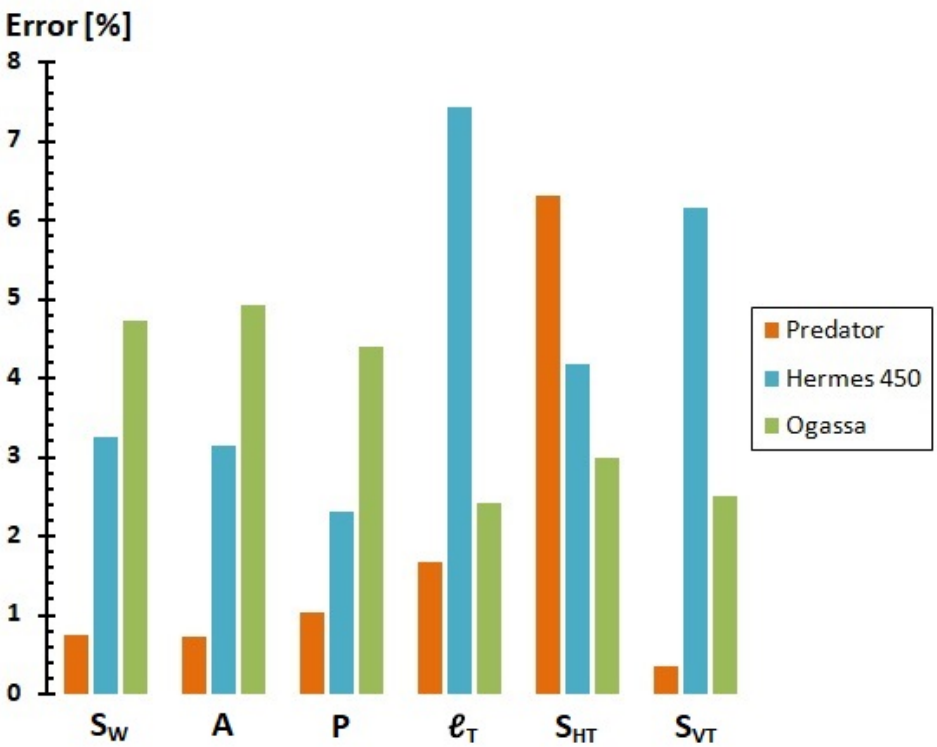

Figure 4.42: Relative error of each computed property for the selected aircraft.

Chapter 5

MALE UAV Design Project

After the conceptualization and validation of a methodology fitted for the conceptual design of UAV, described in the previous chapter, it was time to develop the conceptual design of a new UAV. Driven by UAVision Aeronautics longing to develop an UAV for the 150kg$<$MTOM$\leq$600kg class, the requirements were set and the methodology applied. This chapter documents the project of a Medium Altitude Long Endurance (MALE) class UAV developed in cooperation with the portuguese manufacturer. The aircraft was baptized as Heimdall, after the ever-vigilant guardian of the gods stronghold, Asgard, from Norse mythology. It is the intent of UAVision Aeronautics to further develop Heimdall's project and ultimately produce a first exemplar, thus the design project description is somewhat limited by confidentiality reasons. Furthermore, albeit a more detailed project has already begun, here will be only described the conceptual design project.

5.1 Requirements and Payload

The mission goals required for the UAV in development are those commonly seen in typical surveillance missions. The aircraft must be able to sustain flight for a considerable amount of time, acquire graphical data from the surveillance targets and perform target acquisition and locking, among other things. Also, the aircraft must be equipped with a radar and a satellite communication system. Furthermore, the Heimdall project is to be developed in accordance with international aviation regulations, thus complying with European Aviation Safety Agency (EASA) regulations [22], Federal Aviation Administration (FAA) regulations [23], as well as with North Atlantic Treaty Organization (NATO) regulations [24].

The following list reflects the specific requirements for the MALE UAV developed in this work, which were provided by UAVision Aeronautics.

- Maximum take-off mass - 600kg
- Maximum payload - 150kg
- Fuel reserve at landing - 5%
- Minimum endurance for maximum payload - 15h
- Cruise and loiter ceilings - 22000ft
- Stall speed - 25m/s
- Cruise speed - 50m/s
- Loiter speed - 40m/s
- Dash speed - 65m/s
- Minimum climb speed from mean sea level - 5m/s
- Maximum take-off distance - 1000m
- Minimum performance load factor - -1.5
- Maximum performance load factor - 2.5
- Limit load factors to be sustained by the structure in flight - $-1.52 \leq n \leq 3.8$ [24]
- Structural safety factor - 1.5 [24]
- Minimum sustainable gusts at cruise - 15m/s [24]
- Minimum sustainable gusts at dash - 7.6m/s [24]
- Minimum bank allowed for take-off and landing - 5°

Regarding the surveillance, communication and sensoring requirements, to be matched by payload equipments (gimbal camera, satellite comunications system and radar system), a market study was performed by UAVision Aeronautics communications and imagery specialists to select the equipments best fitted for the application. The selected gimbal camera was the L3 MX-15D [25], shown in figure 5.1, and also other two cameras were considered, the L3 MX-10D [26] and the Octopus Epsilon 175 [27], shown in figures 5.2 and 5.3 respectively. The selection of three different gimbal solutions was considered in order to present the costumers with three levels of performance regarding the imagery systems, which will also be affecting the aircraft maximum endurance. The radar solution considered was the Garmin 18xHD radar dome [28] shown in figure 5.4, for being lightweight and capable of matching the needed

radar accuracy. Finally, the equipment select to enable satellite communications was a specially light system developed by Ultisat [29], shown in figure 5.5.

Figure 5.1: MX-15D gimbal, L3 WESCAM [25].

Figure 5.2: MX-10D gimbal, L3 WESCAM [26].

Figure 5.3: Epsilon 175, Octopus ISR Systems [27].

Figure 5.4: 18xHD radar, Garmin [28].

Figure 5.5: Satellite communication system, Ultisat [29].

5.2 Take-off Mass Estimation

Being Heimdall an aircraft designed for surveillance missions, the main design driver in terms of performance was to maximize the endurance, E. This is the reason why there is only a requirement for minimum endurance. With this in mind, the approach was to perform Heimdall's project as if its ultimate mission profile was to perform loiter for as long as possible.

For the m_{To} estimate, equation 4.1 was applied, imposing m_{pl}=150kg and solving for m_{To} considering: m_e given by equation 4.2, m_{fuel} given by equation 4.3 and m_{res} equal to 5% of m_{fuel}. The fuel mass fractions considered are shown in the following equations. The flight phases are highlighted in bold only to maintain the coherence to that established in section 4.1.2.

Equation 5.1 shows the considered fuel mass fraction for the **Engine Start-up and Take-off** and **Landing** phases, $\left(\frac{m_f}{m_i}\right)_{ESTO}$ and $\left(\frac{m_f}{m_i}\right)_{Ld}$, respectively.

$$\left(\frac{m_f}{m_i}\right)_{ESTO} = \left(\frac{m_f}{m_i}\right)_{Ld} = 0.975 \tag{5.1}$$

Equation 5.2 shows the considered fuel mass fraction for the **Climb and Acceleration to Cruise** phase, $\left(\frac{m_f}{m_i}\right)_{CAC}$.

$$\left(\frac{m_f}{m_i}\right)_{CAC} = 0.99 \tag{5.2}$$

Equation 5.3 shows the considered fuel mass fraction for the **Loiter** phase, $\left(\frac{m_f}{m_i}\right)_{Lt}$.

$$\left(\frac{m_f}{m_i}\right)_{Lt} = e^{\left[-\frac{EV_{Lt}C}{0.9\eta\sqrt{\frac{3\pi Ae_f}{16C_{D_0}}}}\right]} \tag{5.3}$$

Regarding the **Cruise** phase, the fuel mass fraction is assumed to be 1, since there is no range requirement.

Since one of the requirements restricts the MTOM and there is not a set required value for E, being the scope to maximize performance, the approach was to compute m_{To} by increasing E, until m_{To} reaches the required MTOM.

Table 5.1 shows the values of the input parameters and the result of the first take-off mass estimation.

Table 5.1: Inputs and result of the take-off mass estimation.

Parameter	Value
V_{Lt}	40m/s
A	25
C_{D_0}	0.04
e_f	0.5
η	0.8
C	0.35 $\frac{kg}{kWh}$
SF	0.5
Result	**Value**
m_{To}	598.9kg
E	14.7h

5.3 Design Point Selection

The design point selection, or, in other terms, the wing loading, $\frac{W}{S}$, and the power loading, $\frac{W}{P}$, selection, was performed according to the conceptual design methodology proposed by T. C. Corke [7], albeit the necessary adaptations regarding units since the empirically based parameters used in the conceptual design methodology are mostly presented in the imperial system and the present work is developed using the international system. The design point selection is based on equations derived for each flight manoeuvre which impose a limit relation between $\frac{W}{S}$ and $\frac{W}{P}$. Considering the requirements for Heimdall, only take-off distance, speed constraints, climb conditions and maximum load manoeuvres were considered upon selecting the design point.

Equation 5.4 accounts for stall requirements, where $\rho_{_{SL}}$ is the air density at sea level, $C_{L_{max}}$ is the maximum lift coefficient and V_S is the stall speed. This equation represents a minimum required wing area, S, so that the aircraft may be able to stall at the required V_S.

$$\left(\frac{W}{S}\right) = \frac{1}{2}\rho_{_{SL}} C_{L_{max}} V_S^2 \tag{5.4}$$

Equation 5.5 accounts for take-off requirements, where s_{To} is the take-off distance, $\rho_{_{To}}$ is the air density at take-off elevation and V_{To} is the take-off speed, which is equal to 1.2V_S as proposed in the literature [5, 7].

$$\left(\frac{W}{P}\right) = \frac{s_{To} C_{L_{max}} \rho_{_{To}} \eta}{1.305 \rho_{_{SL}} V_{To} \left(\frac{W}{S}\right)} - \frac{12.002\eta}{1.305 V_{To}} \sqrt{\frac{C_{L_{max}} \rho_{_{To}}}{\left(\frac{W}{S}\right) \rho_{_{SL}}}} \tag{5.5}$$

Equation 5.6 accounts for speed requirements by selecting V and ρ equal to the loiter, cruise or dash conditions.

$$\left(\frac{W}{P}\right) = \frac{\eta}{\frac{\frac{1}{2}\rho V^3 C_{D_0}}{\left(\frac{W}{S}\right)} + \frac{\left(\frac{W}{S}\right)}{\frac{1}{2}\rho V \pi A e_f}} \tag{5.6}$$

Equation 5.7 accounts for climb requirements and may reflect different flight conditions by selecting different sets of V and ρ.

$$\left(\frac{W}{P}\right) = \frac{\eta}{\frac{\frac{1}{2}\rho V^3 C_{D_0}}{\left(\frac{W}{S}\right)} + \frac{\left(\frac{W}{S}\right)}{\frac{1}{2}\rho V \pi A e_f} + V_{Cl}} \tag{5.7}$$

Equation 5.8 accounts for maximum performance load factor manoeuvres requirement. This equation is used to account for all manoeuvres to be performed at load factors, n, greater than 1. For Heimdall's project the manoeuvres that need addressing are the sustained turn and the acceleration, both performed at n=2.5. Different flight conditions can be studied by selecting the according V and ρ.

$$\left(\frac{W}{P}\right) = \frac{\eta}{\frac{\frac{1}{2}\rho V^3 C_{D_0}}{\left(\frac{W}{S}\right)} + \frac{n^2 \left(\frac{W}{S}\right)}{\frac{1}{2}\rho V \pi A e_f}} \tag{5.8}$$

Table 5.2 shows the values of the input parameters used to compute the plot on figure 5.6. The values used for properties at sea level are properties of the International Standard Atmosphere [30] and the parameters related to the take-off and landing consider these manoeuvres performed at sea level. Figure 5.6 shows all the relations considered upon selecting the design point as well as the selected design point, which was $\frac{W}{P}$=0.078 and $\frac{W}{S}$=400.

Table 5.2: Inputs for the design point selection.

Parameter	Value	Parameter	Value
ρ_{SL}	1.225kg/m^3	V_S	25m/s
ρ_{To}	1.225kg/m^3	V_{To}	30m/s
ρ_{Lt}	0.6095kg/m^3	V_{Lt}	40m/s
ρ_{Cr}	0.6095kg/m^3	V_{Cr}	50m/s
g_{SL}	9.8067m/s^2	V_D	65m/s
g_{To}	9.8067m/s^2	V_{Cl}	5m/s
g_{Lt}	9.7860m/s^2	$C_{L_{max}}$	2
g_{Cr}	9.7860m/s^2	e_f	0.5
s_{To}	1000m	C_{D_0}	0.04
n_{max}	2.5	A	25

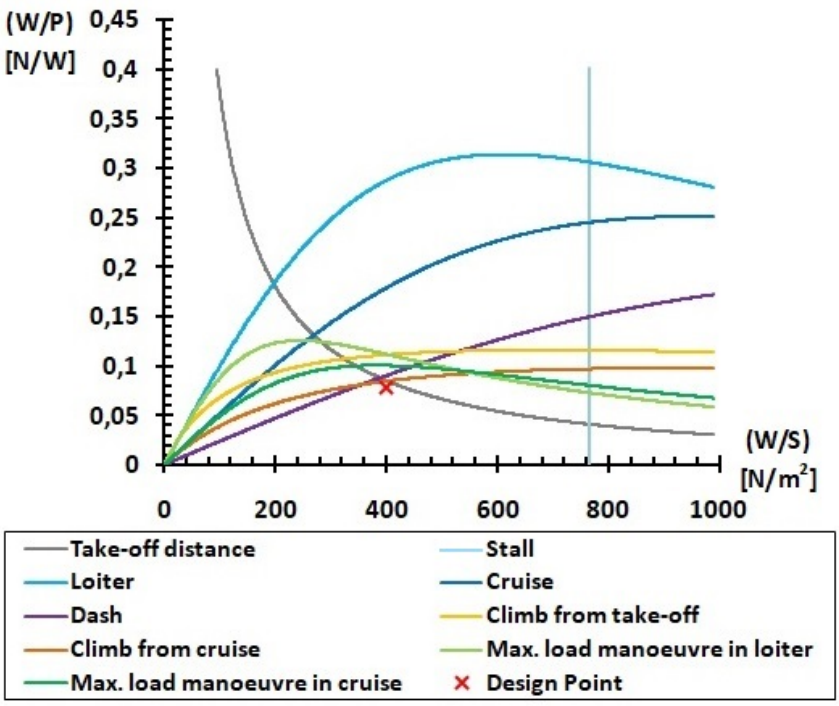

Figure 5.6: Design point selection for Heimdall's conceptual design project.

5.4 Wing Design

The first step on the wing design phase was to select the wing planform shape knowing the required wing area, S, given by the wing loading selection and the initial m_{To} estimation, as shown in equation 5.9. The choice for S, span, b, taper ratio, λ, and aspect ratio, A, was an iterative process having the goal of optimizing the wing efficiency factor, e_f, and the aircraft zero lift drag coefficient, C_{D_0}, therefore maximizing the lift-to-drag ratio. Nonetheless, there was the concern for not increasing the wing struc-

tural complexity, since higher aspect ratios impose heavier wing structures. The final outcome regarding the wing planform shape is presented in table 5.3 and figure 5.7.

$$S \simeq \frac{598.9 \times 9.8067}{400} \simeq 14.67m^2 \tag{5.9}$$

Table 5.3: Heimdall wing planform shape parameters.

Parameter	Value
S	14.7m^2
b	20m
A	27.21
λ	0.4
c_{root}	0.917m
c_{tip}	0.367m
$\bar{c}$	0.778m

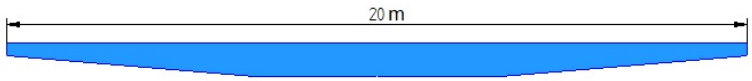

Figure 5.7: Heimdall wing planform shape.

As for the airfoil selection, various airfoil candidates were studied taking into account their performance and their thickness, which is important for structural purposes. The 3D lift coefficient, C_L, needed for loiter is always higher than that needed for cruise since the required loiter speed is lower than the required cruise speed. Besides, as aforementioned, Heimdall is being design for maximum endurance loiter, therefor, knowing the C_L needed for loiter, given by equation 5.10, the approach was to select airfoils which could provide a 2D lift coefficient, C_l, equal or higher than the C_L given in equation 5.10, for low α.

$$C_L = \frac{m_{To} g_{Lt}}{\frac{1}{2}\rho_{Lt} V_{Lt}^2 S} = \frac{598.9 \times 9.786}{\frac{1}{2} \times 0.6095 \times 40^2 14.7} \simeq 0.82 \tag{5.10}$$

Ultimately, two candidates were selected to be further studied in order to determine the efficiency the wing would provide for both cases, computed through equation 4.17b and selecting δ to be 0.04, inferred from figure 4.22. The candidates were the NACA 5415 and the Selig 1020 airfoils and the results of the analysis are shown in figure 5.8 and table 5.4, where $\left(\frac{t}{c}\right)_{max}$ is the airfoil maximum thickness-to-chord ratio and $\left(\frac{x}{c}\right)_{max}$ is the chordwise position of the maximum thickness.

Table 5.4: Summary of the decision driver characteristics of the airfoils in study.

Parameter	NACA 5415	Selig 1020
$\left(\frac{t}{c}\right)_{max}$	0.150	0.151
$\left(\frac{x}{c}\right)_{max}$	0.2929	0.338
k	0.004	0.0137
e_f	0.724	0.452

By comparing the two airfoils on figure 5.8 it is straightforward to notice the much more unsteady behavior of the Selig 1020 airfoil when compared to that of the NACA 5415 airfoil. It is also possible to notice that the Selig 1020 presents stall characteristics for angles of attack, α, much lower than

those presented by NACA 5415 airfoil. Furthermore, given the unsteadiness present in the Selig 1020 behavior, its polynomial fitting is much worse than that of the NACA 5415 airfoil, thus providing a much higher k and a much lower efficiency factor by extent. Taking all this into account, the best choice for airfoil between the two is the NACA 5415.

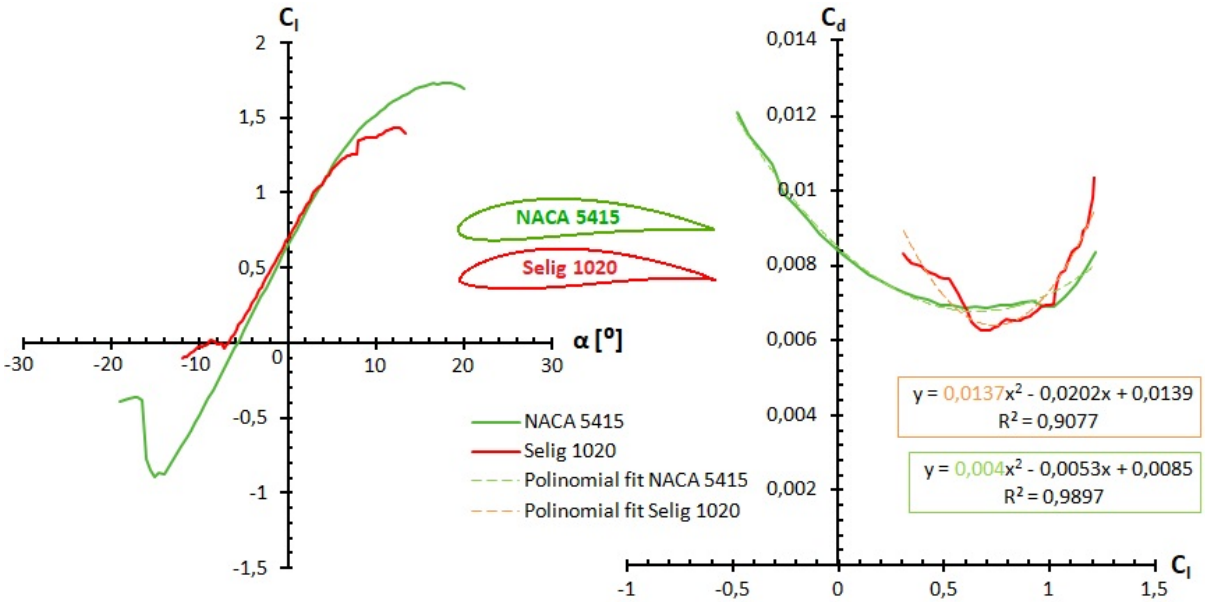

Figure 5.8: Analyses of the airfoils in study. Left side: lift coefficient evolution with the the angle of attack. Right side: drag polar and respective polynomial fitting needed to acquire k.

Having defined Heimdall's wing, its expected performance was studied. Firstly, the wing lift coefficient was obtained following the approach provided by T. C. Corke [7]. This approach consists of computing first the wing C_L versus α linear slope, C_{L_α}, through equation 5.11, where $\Gamma_{(x/c)_{max}}$ is the sweep angle of the maximum thickness line, Γ_{LE} is the leading edge sweep angle and M is the Mach number, and afterwords obtaining C_L through equation 5.12, where α_0 is the airfoil α at which C_l is null.

$$C_{L_\alpha} = \frac{2\pi A}{2 + \sqrt{4 + \left[A\sqrt{1-(M cos\Lambda_{LE})^2}\right]^2 \left[1 + \left(\frac{tan\Lambda_{(x/c)_{max}}}{\sqrt{1-(M cos\Lambda_{LE})^2}}\right)^2\right]}} \tag{5.11}$$

$$C_L = C_{L_\alpha}(\alpha - \alpha_0) \tag{5.12}$$

Also, the wing drag coefficient, C_D, was computed following the approach provided by B. W. McCormick [20], given by equations 4.17. Figure 5.9 shows the linear lifting characteristics of the wing, and figure 5.10 shows the aircraft drag polar.

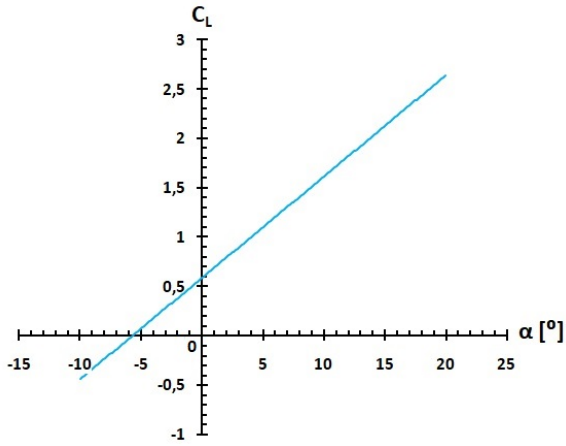

Figure 5.9: Estimated 3D lift coefficient against angle of attack for Heimdall wing.

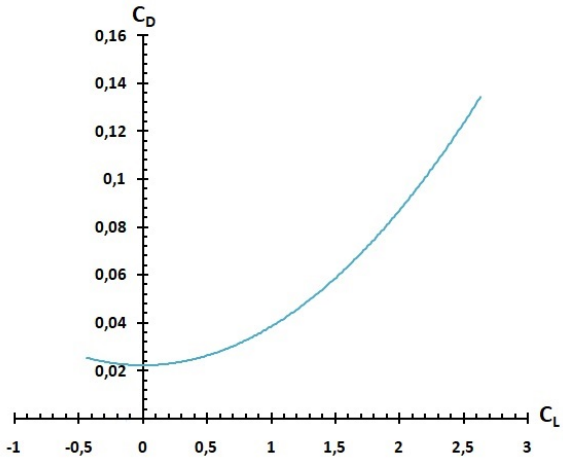

Figure 5.10: Heimdall's estimated drag polar.

5.5 Enhanced Lift Design

Enhanced lift devices will be needed for Heimdall to be capable of taking-off in the required distance. The choice regarding the enhanced lift devices was to use only plain flaps. This decision was supported by some considerations, namely, the fact that plain flaps are the simplest solution for enhanced lift devices regarding implementation and the fact that, after some analyses, they proved to be more than sufficient for the job and provide for a $C_{L_{max}}$ even higher than the needed. For computing the gain in the maximum lift coefficient $C_{L_{max}}$ due to the plain flaps the approach given by T. C. Corke [7] was followed.

Equation 5.13 gives the variation in the zero lift angle of attack, α_0, of the airfoil due to the addition of a trailing-edge flap. In equation 5.13, C_{l_α} is the airfoil C_l versus α slope, δ_f is the flap deflection and K' is a correction for nonlinear effects.

$$\Delta\alpha_0 = -\frac{dC_l}{d\delta_f}\frac{K'}{C_{l_\alpha}} \tag{5.13}$$

Equation 5.14 estimates the wing (3D) $C_{L_{max}}$ from the airfoil (2D) $C_{l_{max}}$ through an empirically based ratio.

$$C_{L_{max}} = \left[\frac{C_{L_{max}}}{C_{l_{max}}}\right] C_{l_{max}} \tag{5.14}$$

Equation 5.15 estimates the wing stall angle of attack, α_S. Here $\Delta\alpha_{C_{L_{max}}}$ is the variation of α at which $C_{L_{max}}$ occurs.

$$\alpha_S = \frac{C_{L_{max}}}{C_{L_\alpha}} + \alpha_0 + \Delta\alpha_{C_{L_{max}}} \tag{5.15}$$

Equation 5.16 gives the increment in the wing $C_{L_{max}}$ due to the flaps, $\Delta C_{L_{max}}$. Here $\Delta C_{l_{max}}$ is the

increment in the airfoil $C_{l_{max}}$ due to the flaps, S_{WF} is the wing flapped area, S_W is the wing area and K_Δ is an empirical correction that accounts for wing sweep.

$$\Delta C_{L_{max}} = \Delta C_{l_{max}} \frac{S_{WF}}{S_W} K_\Delta \tag{5.16}$$

To compute $\Delta C_{l_{max}}$, knowing $(C_{l_{max}})_{flapped}$, which is the maximum lift coefficient generated with the flaps in use, is required and it may be computed through equation 5.17.

$$(C_{l_{max}})_{flapped} = (\Delta\alpha_S - \Delta\alpha_0)\, C_{l_\alpha} + C_{l_{max}} \tag{5.17}$$

Table 5.5 shows the values used for each parameter and their origin, where applicable, as well as the $C_{L_{max}}$ increase and the resulting $C_{L_{max}}$. Notice that parameters which do not present any mention to their origin are either the designers choice or have a fixed known value. On the other hand, parameters mentioning XFLR5 as the origin were obtained through airfoil analyses in the XFLR5 software. Also, $\frac{c_{flap}}{c}$, which gives the flaps chord, c_{flap}, as a percentage of the wing chord, c, despite not being directly used in the presented equations, is used for selecting other parameters, thus its value is also presented.

Table 5.5: Input parameters and outputs of the enhanced lift devices design.

Parameter	Value	Origin
C_{l_α}	2π	Approximation
C_{L_α}	5.875rad^{-1}	Wing design
$C_{l_{max}}$	1.73	XFRL5
$\frac{S_{WF}}{S_W}$	0.7	
$\frac{c_{flap}}{c}$	0.3	
K_Δ	0.92	Equation 9.12 on [7]
$\frac{dC_l}{d\delta_f}$	4.6	Figure 9.4 on [7]
K'	0.54	Figure 9.3 on [7]
$\left[\frac{C_{L_{max}}}{C_{l_{max}}}\right]$	0.9	Figure 9.9 on [7]
$\Delta\alpha_{C_{L_{max}}}$	1.8º	Figure 9.11 on [7]
$\Delta\alpha_S$	-2.8º	Figure 9.18 on [7]
Output	**Value**	
$\Delta C_{L_{max}}$	0.919	
$(C_{L_{max}})_{flapped}$	2.477	
$(\alpha_S)_{flapped}$	12.977º	

5.6 Tail Design

The tail design for Heimdall's project was performed according to the approach established on section 4.4.2 and the decisions applied to this design phase were as follows.

- **Engine(s) placement**. At this point the number of engines was not yet decided, nonetheless, the decision was to place the engine(s) like in the ATME configuration (appendix A). This decision was motivated by two major issues. Firstly, placing the engine(s) in an ATME configuration would help bringing the aircraft CG further back which is good for stability purposes. Secondly, the alternative configuration in the case of having two engines would be to place them on the wing which would imply an increase in the complexity and mass of the wing structure.

- **Tail shape**. The decision was to have an A or V shaped tail, not due to any performance reason, simply because it gives a nicer look to the aircraft.

- **Length ratio**. $\frac{\ell_T}{\ell_{Total}}$ was set to be 0.45, according to the results shown in the database for UAV having the same engine placement.

- **Airfoil**. The airfoil selected was the NACA 0012, which is a symmetric airfoil not to thick and therefore a good choice in terms of performance since it allows for tail drag and mass reduction.

Table 5.6 presents some properties of the selected tail configuration.

Table 5.6: Heimdall's tail shape parameters.

Parameter	Value
ℓ_T	3.996m
S	5.11m^2
Half span (b/2)	3.573m
A	10
λ	0.4
c_{root}	1.02m
c_{tip}	0.408m
V angle	89.44º

5.7 Engine Selection

As a result of the design point selection, the power loading required is known and therefore the power, P, required for propulsion may be obtained through equation 5.18.

$$P \simeq \frac{598.9 \times 9.8067}{400} \simeq 75297.64W \tag{5.18}$$

Knowing P, a search was conducted among some of the renown UAV engine manufacturers, such as Desert Aircraft [11], 3W International [12], Hirth Engines [13], Rotron [14] and NorthwestUAV [15], to find suitable engine candidates. Apart from P required, the engine(s) selection was performed keeping in mind the goal for efficiency and therefore the candidates studied were all rotary or 4-stroke engines.

The final decision was to use two RT600LCR-EXE engines, manufactured by Rotron [31], which provide a combined maximum continuous power output of 79kW. The choice for having two engines instead of just one was due to two major reasons. Firstly, a bigger engine capable of delivering more than the required power would have the same or even higher mass than the two selected engines combined, according to the research performed on the UAV engines market. Secondly, having two engines allows for redundancy in the propulsion system. According to figure 5.6, for the selected wing loading, the power loading required to perform cruise is a bit more than two times the selected power loading, meaning that it requires less than half the power given in equation 5.18 for Heimdall to fly at cruise conditions. For loitering the required power is even less, meaning that Heimdall would be capable of sustaining flight even with one engine down. Therefore, by using two RT600LCR-EXE engines the propulsion system redundancy is ensured, thus greatly improving Heimdall's reliability. The RT600LCR-EXE engine is presented in figure 5.11 and table 5.7 provides some relevant engine performance details.

Table 5.7: RT600LCR-EXE engine performance details [31].

Parameter	Value
Max power	53HP at 5000rpm
Max continuous power	53HP at 5000rpm
Mass (block only)	21.2kg
C at 3700rpm	0.3528 $\frac{kg}{kWh}$

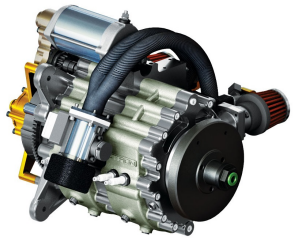

Figure 5.11: RT600LCR-EXE engine.

5.8 Fuselage Design

The main purpose for the fuselage design is the definition of the placement of each component. Since the position of the components directly influences the aircraft CG, and therefore its stability, this design step was performed by iterating with the refined mass and static stability analysis culminating in the final layout presented in figure 5.12, where the bottom part is a top view, the top part is a side view and all units are in mm.

Regardless of the fact that a FMT provides less overall efficiency than a BMT, due to the influence on the fuselage fineness ratio, as previously explained in chapter 4, the aircraft was design with a FMT configuration by choice of UAVision Aeronautics. The rational for this decision is bound with the expected overall look of the aircraft. For that reason, the fuselage drag is not a driver in this project and thus the fuselage fineness ratio was not a concern. The fuselage length was first computed based on the previously selected length ratio, $\frac{\ell_T}{\ell_{Total}}$, knowing ℓ_T obtained in the tail design. Afterwords, the fuselage length was iterated due to the placement of the engines.

Albeit not required, the liberty was taken to establish a component layout which would allow for the setting of not one but three cargo bays. The idea was to make use of the fuselage internal volume,

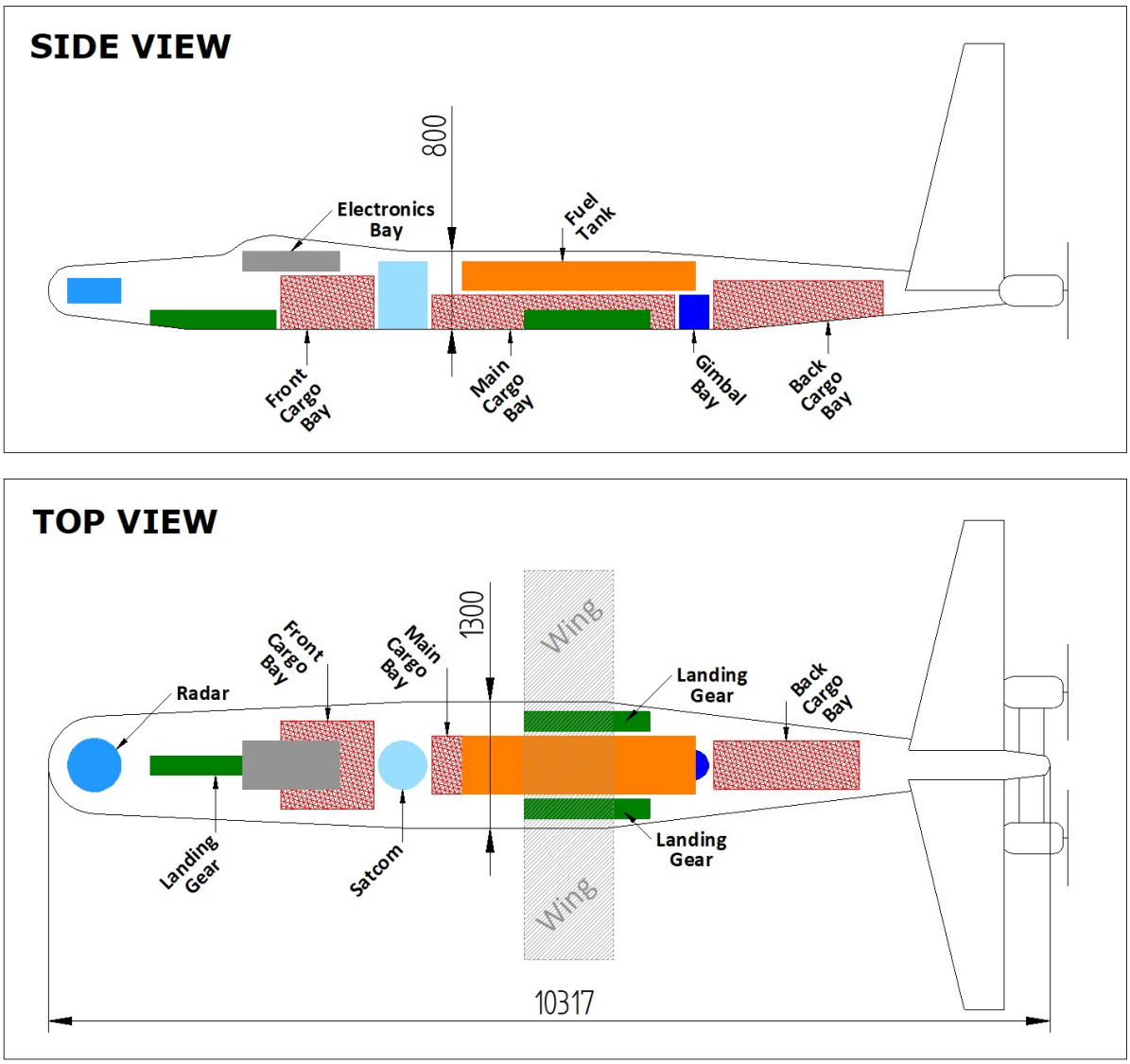

Figure 5.12: Heimdall's fuselage layout.

not needed for the remaining components, to allow the inclusion of more payloads inside the fuselage. Furthermore, the cargo bays may be a nice feature considering the type of missions Heimdall would perform, e.g. maritime surveillance.

It is of importance to mention the origin of the considered components dimensions. The dimensions of the payload components were taken from manufacturer data [25, 26, 27, 28, 29]. The dimensions for the fuel tank were selected considering the available internal volume, the needed fuel for a maximum endurance mission, which will be defined in section 5.11, a 5% fuel reserve and some extra volume, for safety. The dimensions for the electronics bay were selected by comparison with UAV exemplars already developed by UAVision Aeronautics as well as by recommendation of the company's electronics

experts. Finally, the dimensions for the landing gear bays were set considering the needed landing gear dimensions that were determined considering a bank limit of 5º and an α of 13º, which is above the stall angle of attack, on the take-off and landing phases.

5.9 Structure Design and Material Selection

The structure design and material selection is a design step of utmost importance when it comes to the aircraft performance. The aircraft structure must be designed to sustain the loads that may be experienced during operation as well as those imposed by international regulations. All this keeping in mind the objective of developing the aircraft with an empty mass as low as possible.

It is usual in this design step to compute the aircraft V-n diagram showing the aircraft flight envelope. For this purpose the approach presented by T. C. Corke [7] was followed and Heimdall's flight envelope is presented in figure 5.13, where $V_{highAoA}$ is the flight speed for high angle of attack and V_{dive} is the dive speed, which was set at 1.5V_{Cr} as proposed in the literature [5, 7]. Furthermore, table 5.8 shows some of the parameters used upon computing the V-n diagram, where $\hat{u}$ is the average gust normal speed component. It is of importance to mention that the average gust speeds used for this project are higher than those statistically considered in the literature for the atmosphere at 22000ft [5, 7].

Table 5.8: Parameters used for computing Heimdall's V-n diagram.

Parameter	Value
Performance load factor range	-1.5≤n≤2.5
Design load factor range	-1.52≤n≤3.8
Ceiling	22000ft
ρ	0.6095kg/m^3
g	9.786m/s^2
$\hat{u}$ in loiter	12.5m/s
$\hat{u}$ in cruise	11m/s
$\hat{u}$ in high α flight	15m/s
$\hat{u}$ in dive	5m/s

Having the goal for overall efficiency, the main building material for the Heimdall had be some kind of composite material. The commonly used composite materials on aeronautic structures are formed by a matrix of epoxy resin and a filling composed of carbon, glass and/or kevlar fibers, being the filling the part which provides most of the mechanical properties to the composite. Glass fiber composites usually provide good electrical insulation, have good fire and chemical resisting properties and have a low production cost when compared to carbon or kevlar composites, for example. Carbon fiber composites are mainly used for structural purposes due to their strength, resistance and durability. As for the kevlar composites, apart from their strength similar to that found on carbon composites, can in some cases ensure the mobility of the structure in joints, for example, and are used in a large number of UAV applied

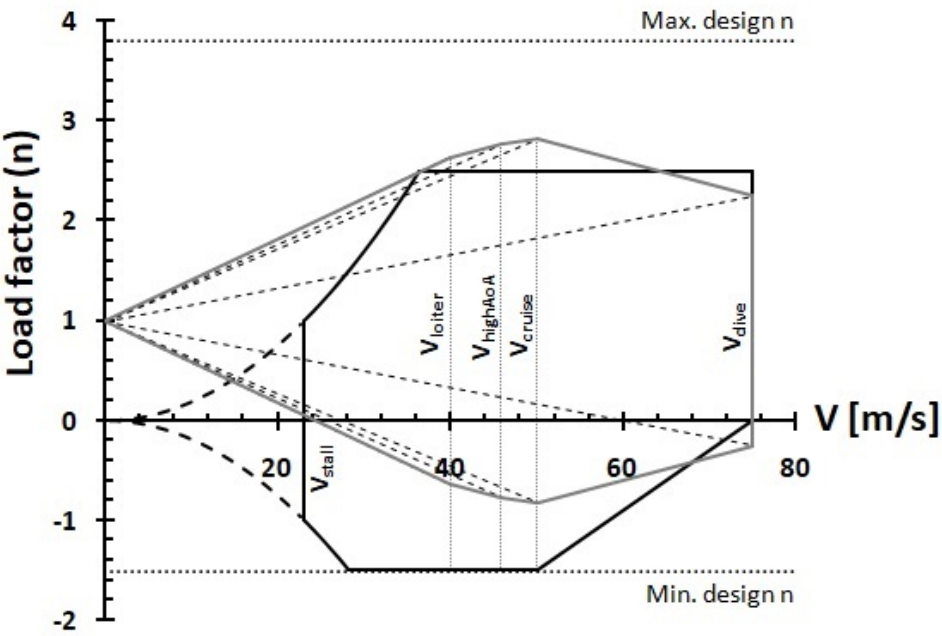

Figure 5.13: V-n diagram showing Heimdall's flight envelope including gusts (full grey line).

to the aircraft movable surfaces such as flaps, ailerons, elevators and rudders.

The decision for Heimdall's project was to have the entire structure made of composite materials only using an aluminum alloy where fittings and mounts would exist, simply because fiber composites are not so good when it comes to secure parts through the use of bolts and/or screws and therefore a metal surface is normally required, at least on main structural components.

For this work only the main wing structure was addressed, since in this earlier design phase there is no need for detailed production related considerations which would affect the structural design. In a later design phase a structural design and analysis will be needed also for the tail and specially for the fuselage. Nonetheless, the tail structural design will be performed alike that which will be described for the wing and the fuselage structural design will also follow a similar procedure albeit with some different considerations regarding the loading distribution.

The basic structure needed for a wing is composed by one or more spars, which are cantilevered beams functioning as the wing main structural component by resisting to the majority of the forces applied during flight, and several ribs, which serve the main purpose of securing the wing upper and lower surfaces in place. Heimdall's wing was designed having one main spar and several ribs, made entirely of carbon fiber composites, along with upper and lower surfaces also made of carbon fiber composites. For the upper and lower surfaces the decision was to use 2 layers of carbon fiber with 0.4kg/m^2 and the fibers aligned at +/-45°. In some areas of the wing surfaces the carbon layers will be fitted with 1.2mm airex foam in between them.

The main spar was designed scoping to make the most use of the wing thickness, therefore the solution was to design it to be built as part of the upper and lower surfaces, since a beam resistance grows with the third power of its sectional height. An optimization algorithm previously developed by UAVision Aeronautics, which is based on composite engineering principles found on the literature [32, 33, 34], was used in the design of the spar. Basically, this algorithm considers the maximum in flight load, the structural safety factor, the span, the maximum wing thickness and allowed width for each layer, by user input, and computes the number of carbon fiber layers needed for the spar, along with the length of each layer, considering an elliptical load distribution. The material considered was unidirectional carbon fiber with 0.2kg/m^2 and an yielding stress of 1.1GPa. Being the spar embedded in the upper and lower wing surfaces, the space in between the spar upper and lower surfaces is to be filled with a sandwich composite made of airex foam and carbon fiber. Table 5.9 shows the relevant inputs and table 5.10 the resulting layering for the spar, where ℓ is the length of the unidirectional carbon fiber strip of each layer. Figure 5.14 shows the complete layering for the upper and lower surfaces, as well as the predicted placement of the ribs.

Table 5.9: Input parameters for computing the wing spar layering.

Parameter	Value
MTOM	600kg
Wing span (b)	20m
Max. load factor	3.8
Safety factor (sf)	1.5
Spar width	0.192m
Max. thickness	0.1378m
Min. thickness	0.0551m
Layer thickness	0.0002m

Table 5.10: Carbon fiber layering for the wing spar.

Layer	ℓ [m]	Amount	Layer	ℓ [m]	Amount
1	15,5	2	11	4,6	2
2	13,6	2	12	4,05	2
3	12,05	2	13	3,5	2
4	10,75	2	14	3	2
5	9,55	2	15	2,5	2
6	8,4	2	16	2,05	2
7	7,4	2	17	1,6	2
8	6,5	2	18	1,15	2
9	5,85	2	19	0,75	2
10	5,2	2	20	0,3	2

As aforementioned, the fuselage and the tail structural design were not addressed in this project. This decision was taken considering the fact that, at this point, Heimdall's preliminary design project is already good enough for the future manufacturer, UAVision Aeronautics, and a more detailed design will only be needed once Heimdall is cleared for detailed design and production. Also, the fuselage structural design, which would be the most complex of the two, needs to be performed with detail otherwise would be useless for UAVision Aeronautics.

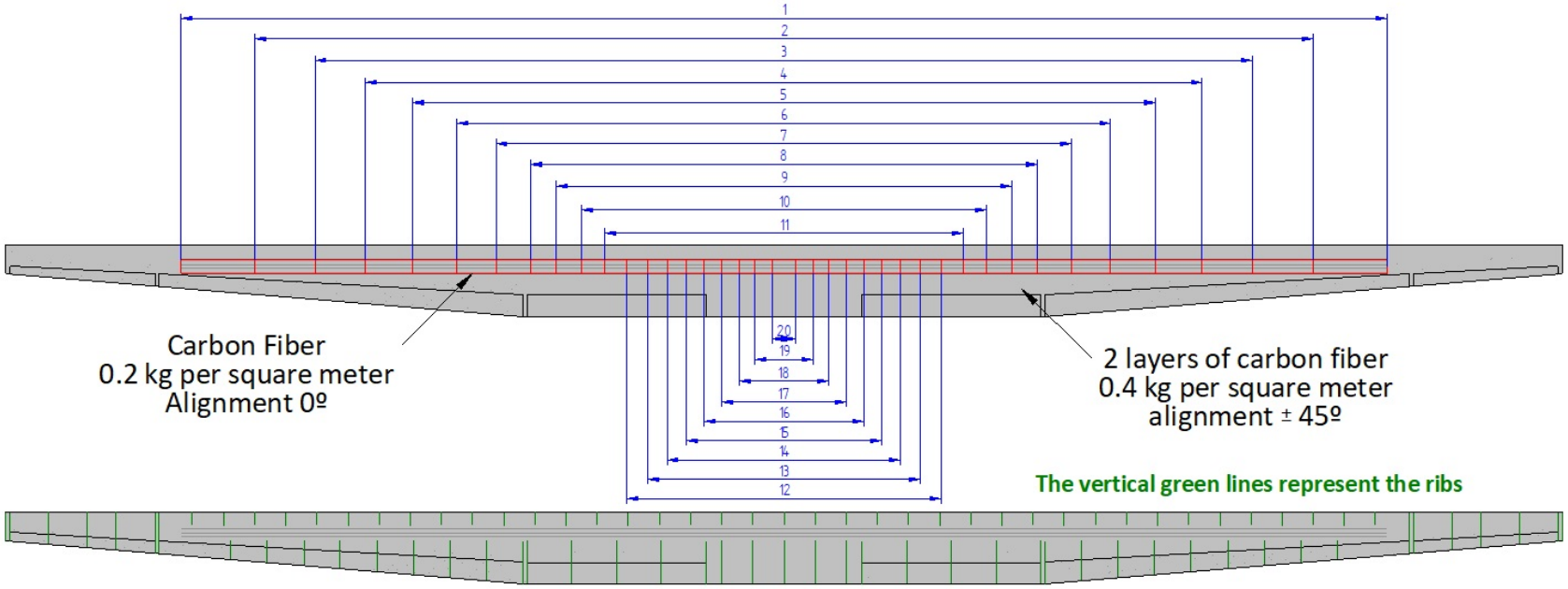

Figure 5.14: Heimdall's wing structural layout.

5.10 Refined Mass and Static Stability Analysis

The refined mass analysis is used, combining with the fuselage design, to determine the aircraft CG and its inertia. To perform this task, the positioning, dimensioning and mass estimation of each of Heimdall's components was determined and the principles proposed by P. F. Beer and R. E. Johnston Jr. [35] were applied. The mass considered for each component is presented in table 5.11 along with the resulting calculated CG position and moments of inertia. The mass considered for each part of the aircraft structure was taken by comparison with the mass of similar structures already built by UAVision Aeronautics. As for the landing gears, a search was conducted between the known UAV landing gear manufacturers, and the mass taken by comparison with models matching the project requirements. Regarding the payload, it was considered the basic payload version which includes the radar, the satellite communication system and the MX-15D gimbal, along with a fictional extra payload to reach m_{pl}=150kg.

Table 5.11: Refined mass estimates and computed moments of inertia.

Component	Mass [kg]	Component	Mass [kg]
Wing	80	Satcom	12.5
Fuselage	80	Gimbal MX-15D	53
Tail	20	Electronics board	5
Fuel	180	Fuel tank	5
Engine 1	35	Front landing gear	15
Engine 2	35	Left landing gear	20
Radar	7.7	Right landing gear	20
Extra Payload	76.8	Cabling	5
Moment of Inertia	**Value [kgm^2]**		
I_x	6922.77		
I_y	7432.93		
I_z	10349.57		
I_{xz}	130.91		
Other results	**Value**		
SF	0.53		

Regarding the static stability analysis, it was performed using an algorithm previously developed by UAVision Aeronautics, which is based on the principles proposed by B. Etkin [36]. The main objective of this analysis was to compute the range of the static margin, k_n, which represents the difference between the neutral point position and the CG position, with respect to the wing aerodynamic center. The neutral point is the most aft position of the CG at which the horizontal tail is still effective for controlling the aircraft pitch and thus the longitudinal aircraft stability. For the aircraft to be statically stable k_n must be positive, otherwise, the aircraft would need active control to be longitudinally stable. The range for k_n computed in this analysis, given as a percentage of the mean aerodynamic wing chord, $\bar{c}$, was 0.0827$\leq$k$_n\leq$1.0425. The lateral and directional static stability of the aircraft were not considered for this project because they do not present a major concern since an UAV requires active control. The longitudinal stability is of importance because if the aircraft is naturally unstable it would mean that a critical failure in the autopilot

would plunge the aircraft to the ground.

5.11 Heimdall's Overview and Performance

Following the conceptual design methodology proposed by T. C. Corke [7] and applying the necessary adaptations that were described and verified in the previous chapters, it was possible to establish the conceptual design of the Heimdall MALE UAV. As aforementioned, the design project was developed aiming for the maximum overall efficiency of the aircraft although respecting both the requirements and also UAVision Aeronautics will regarding the fuselage.

At this stage in the design project, Heimdall is ready for the detailed design phase since even its dynamic stability was analysed, albeit not described in this work for falling out of its scope. Furthermore, the project has already passed the final evaluation and validation stand point and, provided the financial availability, will pass on to the detailed design phase and later to production.

Designed to perform any kind of surveillance mission and to be a versatile asset for any civil and/or military operator, Heimdall makes use of an high aspect ratio wing, to provide the needed lift with low drag, and two powerful propeller pusher engines in order to be able to sustain flight with low fuel consumption, and, at the same time, be able to achieve a respectful dash speed. Having two independent engines allows for the assurance of mission accomplishment since Heimdall can sustain cruise and loiter with only one engine operational. Moreover, table 5.12 presents a sum-up of Heimdall's design and performance characteristics.

Table 5.12: Heimdall design and performance parameters.

Property	Value	Property	Value
MTOM	600 kg	ℓ_{Total}	10.5m
Max. payload	150kg	b	20m
V_S	25m/s	S_W	14.7m^2
V_{Lt}	40m/s	$\bar{c}$	0.755m
V_{Cr}	50m/s	A	27.21
V_D	65m/s	S_{HT}	2.531m^2
P	79kW	S_{VT}	2.575m^2
Max. E	53.5h	C_{D_0}	0.0223

Heimdall's overall efficiency is one of its game changing characteristics, resulting in a platform able to perform long endurance missions within the below 600kg class. Its maximum endurance for the minimum payload configuration of 53.5h equals and even overcomes the performances of other UAV in the same class. For example, the Gnat 750 manufactured by General Atomics presents a maximum endurance of 48h with a MTOM of 510kg. Furthermore, Heimdall's performance will be further increased once the detailed design project is performed.

Another important feature of Heimdall are the three cargo bays. At first glance, given the fact that

Heimdall has been designed to perform mostly surveillance missions, the existence of cargo bays may not present that much of an advantage. On the other hand, since the ultimate goal of UAVision Aeronautics is to sell this aircraft for the maximum number of applications possible, presenting the customers with an aircraft of this class having this kind of performance and also the ability to transport cargo within its fuselage in three separate cargo bays may be a deal closer.

As a practical example of the importance of Heimdall's internal cargo capacity, since one of its missions would be maritime surveillance, imagine how useful would be if the aircraft could carry an inflatable raft as a mandatory payload when performing maritime surveillance mission, just in case of any distress call from a sinking vessel. This idea was explored and, in fact, Heimdall could carry not one but up to five inflatable rafts as payload within its cargo bays. Common inflatable life rafts used in aviation were look after and two models were selected, manufactured by Eastern Aero Marine [37], the EAM-12, designed for twelve people, and the EAM-25, designed for twenty five people, shown in figures 5.15 and 5.16, respectively. Several payload options (Op) were explored and are presented in table 5.13 along with the resulting expected maximum endurance of the aircraft.

Figure 5.15: EAM-12 life raft, Eastern Aero Marine.

Figure 5.16: EAM-25 life raft, Eastern Aero Marine.

Table 5.13: Heimdall's payload options and expected performance.

Op	Payload	m_{pl}	Max. E
1	radar + satcom + Epsilon 175	25kg	53.5h
2	radar + satcom + MX-10D	40kg	49h
3	radar + satcom + Epsilon 175 + (1x) EAM-12	41kg	48.5h
4	radar + satcom + Epsilon 175 + (1x) EAM-25	60kg	43h
5	radar + satcom + MX-15D	73kg	39.5h
6	radar + satcom + MX-15D + (1x) EAM-12	89kg	35h
7	radar + satcom + MX-15D + (1x) EAM-25	108kg	30h
8	radar + satcom + MX-15D + (2x) EAM-25	143kg	21h
9	radar + satcom + Epsilon 175 + (2x) EAM-25 + (3x) EAM-12	143kg	21h
10	maximum payload	150kg	19.5h

In the sense of a maritime search and rescue mission, Heimdall will be capable of carrying up to five life rafts (payload option 9 on table 5.13) which would be sufficient to save a minimum of 86 people from a sinking vessel situation. Even with payload option 8, which includes the best gimbal camera option but only two life rafts, a minimum of 50 people could be saved. In this regards, it becomes clear that having three cargo bays might be very handy. On the other hand, considering a direct military application,

Heimdall's payload capacity and internal storage may present a good advantage when considering a weaponized variant.

Concluding the project overview it is important to notice that the obtained maximum endurance for the maximum payload configuration (payload option 10 on table 5.13) was well above the requirement of 15h. This helps to the conclusion that the conceptual design project was successful and the goal for efficiency was accomplished.

The overall look of Heimdall MALE UAV may be visualized in figure 5.17.

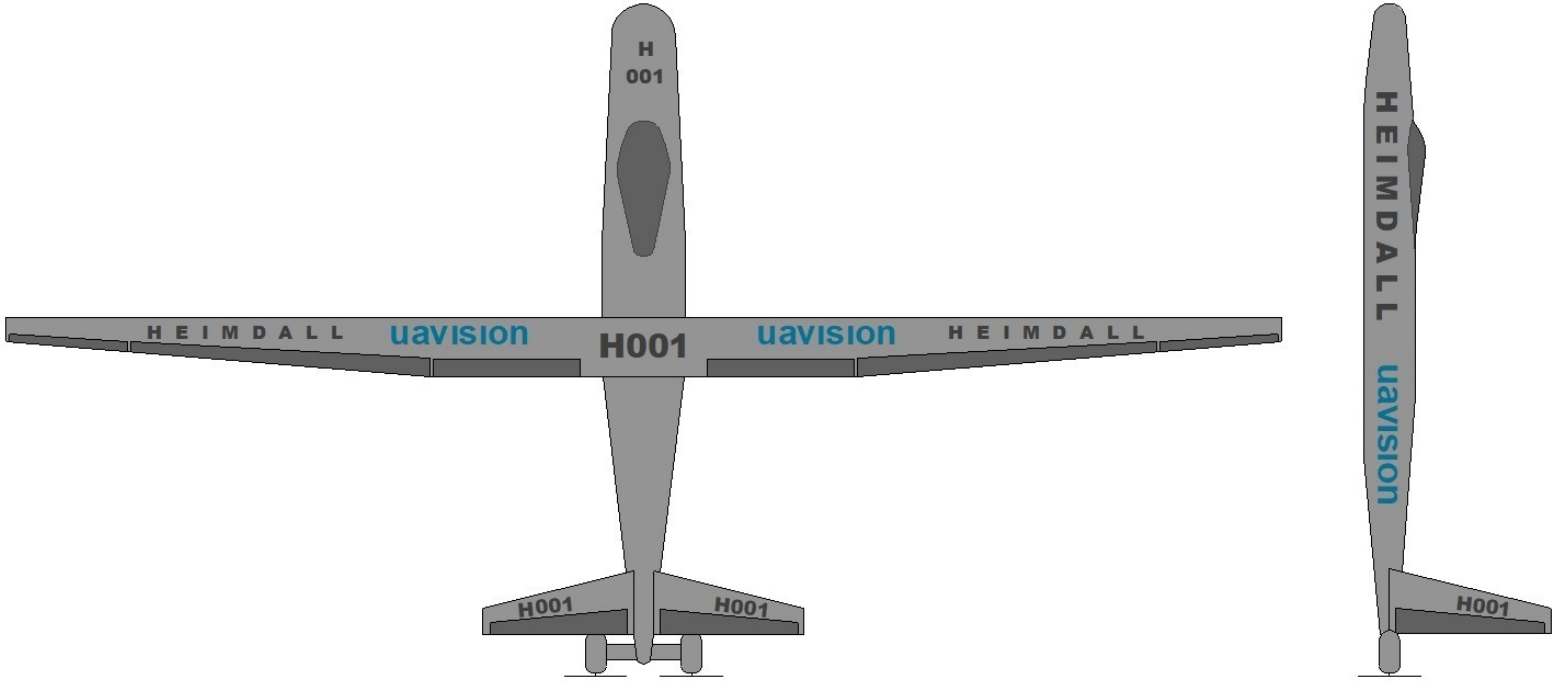

Figure 5.17: Heimdall's overall look. Left side: top view. Right side: side view.

Chapter 6

Conclusions

In the reality of XXI century society, many are the applications for UAS and the number of UAS is ever increasing as technological advances allow the improvement of systems and techniques. As far as fixed-wing UAV are concerned, the envelope of applications is growing quite rapidly and, albeit some may find the uses for this aircraft to be finite, there will always be the need for this fixed-wing platforms, until a more efficient way of sustaining flight and accomplishing different mission requirements is developed. Since UAV are platforms built for carrying something through the air, whether it is a camera, a particular set of measurement sensors, communications relay systems, weapon systems or other type of cargo, their lifespan as a technology will be long as people will always find the need to acquire information from above. Furthermore, technology improvements will allow for the development of better sensors and better cameras, etc., and therefore it is very likely that the present generations will live in a time in which more and more UAV will be cruising the sky. Being that as it may, the need for regulations and literature regarding the development of fixed-wing UAV is a must.

For the successful development of a conceptual design methodology for unmanned aircraft it would be necessary to convince all the manufacturers, or at least a large number of them, to provide to the general public data from their UAV which is now considered sensitive information. This is bound to the fact that the conceptual design of an aircraft has to be perform based sometimes on empirical data, as was promptly clarified in chapters 2 and 3. The only way to obtain empirical data is with the cooperation of UAV manufacturers. This posed the major setback for the realization of this work, since the lack of available data lead to the need for estimating many parameters considered in the database.

Albeit many of the data gathered in the database had to be estimated based on other properties of the aircraft and conservative assumptions, the work was not jeopardized because the goal was ultimately to prove that certain assumptions considered in the literature [3, 4, 5, 6, 7] for manned aircraft do not apply to most UAV, only being possibly fitted for UAV with the size and performance similar to a manned aircraft.

This goal was duly accomplished and, as a result, the methodology to be followed in the conceptual design of an UAV may be that presented by T. C. Corke [7] or M. H. Sadraey [5], for example, applying the changes proposed in chapter 4. The down side was that the range of values proposed for certain UAV parameters, or even the methods proposed for estimating certain parameters, do not have the accuracy that would be possible if all the data was provided by the manufacturers.

Nonetheless, the proposals made on chapter 4 allowed for the establishment of a methodology that, if followed and handled with certain care, allows the development of a much more conservative conceptual design of UAV, specially due to the proposals made regarding the zero lift drag coefficient, C_{D_0}, and the efficiency factor, e_f, estimation. A conservative conceptual design approach for UAV is of utmost importance when applied to the industrial world. In fact, it is always a good practice to present a conceptual design which, despite being good, is somewhat worse, performance wise, than the detailed design and ultimately the actual aircraft. This way the designer assures that the predicted performance may even improve and can never worsen.

As for the application of the conceptualized methodology, materialized in the conceptual design of Heimdall, it may be considered as a success. Having the ultimate goal for the maximum endurance possible, the initial perspective presented in table 5.1 was somewhat poor, not even respecting the requirement for E_{max} with max. payload of 15h. Nonetheless, the final outcome accomplishes and even surpasses those requested 15h. It was mainly due to the use of McCormick's formulation for C_D and e_f and the study of the airfoils fitting constant, k, that the resulting performance, albeit conservatively computed, was so good when compared to that of other UAV in the below 600kg class. As expected and demonstrated in section 5.4, the resulting efficiency factor of the wing is largely influenced by the airfoil and its performance at different Reynolds numbers, which supports the suggested adaptations regarding the computation of C_D and e_f.

The majority of decisions regarding Heimdall's design were performed scoping to the highest overall efficiency, which translates into the highest maximum endurance. On top of that Heimdall's fuselage layout allows the transport of extra payload inside one of its three cargo bays. Table 5.13, showing the expected performance for different payload options, ultimately demonstrates Heimdall's versatility and, moreover, its ability to sustain flight for over two days, reaching the competence level of some of the best military grade UAV of its class. Therefore, Heimdall's expected performance and design characteristics are very desirable for its expected applications, and UAVision Aeronautics itself is very pleased with the aircraft and intents to continue its project and ultimately pass it on to production. Hopefully, Heimdall aircraft will be used to perform surveillance and other types of mission at the hands of European armed forces.

6.1 Future Work

The major proposal regarding future work, in terms of the UAV conceptual design methodology, is to add more and more UAV to the database and ultimately obtain their data directly from the manufacturers or operators. This would allow for the proposal of better fitted empirically based values for certain parameters and thus the results obtained through this conceptual design methodology would be closer to those obtained afterwords in the detailed design of an UAV.

Furthermore, a list of airfoils better fitted for lower Reynolds numbers, Re, would also be a nice addition to this proposed methodology. For that purpose, another proposal for future work is to study a considerable number of airfoils, namely Selig airfoils [18], with the scope of determining the values of their parabolic fitting constant, k, for different Re. This would facilitate the choice for airfoil regarding the wing efficiency factor , e_f.

As for Heimdall's design project, the work that needs to be developed so forth is mainly bounded with the detailed design phase. Nonetheless other requirements should also be defined such as strict take-off and landing distances and, if needed, size-related limits, such as a maximum allowed span.

A more careful dynamic stability analysis for defining the needed ailerons and ruddervators areas must be done, albeit a dynamic stability analysis has already been performed.

A more detailed search and study regarding the retractable landing gear systems to be applied is also needed, in order to better understand the actual internal space they would occupy.

A final fuselage internal layout, considering all the equipment needed and its placement, as well as the size and position of the doors of the cargo bays and the placement of all the cabling throughout the fuselage, and the fuselage structural design and analysis are needed. Regarding the fuselage structural design it must consider the loads that would be transmitted by the wing and the tail, the loads transmitted by the landing gears and also the internal mountings of all the equipment.

The internal structure of the tail must be designed, in the same fashion as the wing, considering the in-flight loads to be suffered and the limit load factors imposed by international regulations, the mounting of the servo actuators for the ruddervators, the lights needed in both tips and all the cabling.

The internal structure of the wing needs an iteration to include the servo actuators mounting plates, the tip lights and the cabling, and also, if possible, maybe some structural optimization with the goal of reducing the number of ribs.

An ultimate aerodynamic computational analysis, to be performed in a fluid mechanics software, would be a must, in order to confirm the aircraft performance in terms of lift and drag.

After all this, the final design of Heimdall would be completed and, after all the detailed 3D Computer Aided Designs (CAD) terminated, a first prototype could be manufactured.

Bibliography

[1] Paul G. Fahlstrom and Thomas J. Gleason. *Introduction to UAV Systems*, volume I. John Wiley Sons, Inc., 4th edition, 2012.

[2] E. Atkins, A. Ollero, and A. Tsourdos. *Unmanned Aircraft Systems*, volume I. John Wiley Sons Ltd, 1st edition, 2016.

[3] Jan Roskam. *Airplane Design*, volume I. Roskam Aviation and Engineering Corporation, 1st edition, 1985.

[4] Jan Roskam and Chuan-Tau Edward Lan. *Airplane Aerodynamics and Performance*. Design, Analysis and Research Corporation (DARcorporation), 1st edition, 1997.

[5] Mohammad H. Sadraey. *Aircraft Design: A Systems Engineering Approach*. John Wiley Sons, Ltd., 1st edition, 2013.

[6] Daniel P. Raymer. *Aircraft Design: A Conceptual Approach*. American Institute of Aeronautics and Astronautics (AIAA), Inc., 2nd edition, 1992.

[7] Thomas C. Corke. *Design of Aircraft*. Prentice Hall, 1st edition, 2003.

[8] M. Adamsky. Analysis of propulsion systems of unmanned aerial vehicles. *Journal of Marine Engineering Technology*, 16(4):291–297, 2017.

[9] David F. Rogers. Propeller efficiency rule of thumb, 2010. URL: `http://www.nar-associates.com/technical-flying/propeller/cruise_propeller_efficiency_screen.pdf` - (23-04-2019).

[10] Brian D. Rutkay. A process for the design and manufacture of propellers for small unmanned aerial vehicles. Master's thesis, Carleton University, Ottawa, Ontario - Canada, 2014.

[11] Desert Aircraft. 1815 S. Research Loop, Tucson AZ, 85710, USA. URL: `https://www.desertaircraft.com` - (15-04-2019).

[12] 3W International. Hollerstrasse 12, 61350 Bad Homburg, Germany. URL: `http://3w-international.com` - (15-04-2019).

[13] Hirth Engines. Max-Eyth-Strasse 10, 71726 Benningen am Neckar, Germany. URL: http://hirthengines.com - (15-04-2019).

[14] Rotron Power Ltd. 9 Chaldicott Barns, Tokes Ln, Semley, Dorset, SP7 9AW, United Kingdom. URL: http://www.rotronuav.com - (15-04-2019).

[15] Northwest UAV. 11160 SW Durham Lane, Suite 1, McMinnville OR 97128, USA. URL: https://www.nwuav.com - (15-04-2019).

[16] Advanced Precision Composites. Propellers performance data summary. URL: https://www.apcprop.com/files/PER2_MAXPE.DAT - (16-04-2019).

[17] Ira H. Abbott, Albert E. Von Doenhoff, and Louis S. Stivers Jr. Summary of airfoil data. Technical Report 824, National Advisory Committee for Aeronautics, Langley Memorial Aeronautical Laboratory, Langley Field, Virginia., 1945.

[18] Michael S. Selig, James J. Guglielmo, Andy P. Broeren, and Philippe Giguère. Summary of low-speed airfoil data. 1, 1995.

[19] G. R. Spedding and J. McArthur. Span efficiencies of wings at low reynolds numbers. *Journal of Aircraft*, 47(1):120–128, 2010.

[20] Barnes W. McCormick. *Aerodynamics, Aeronautics, And Flight Mechanics*, volume I. John Wiley Sons, Inc., 2nd edition, 1995.

[21] I. Grosu. *Calculul Si Constructia Avionului*, volume I. Editura Didactica Si Pedagogica, 1st edition, 1965.

[22] *Regulation 2018/1139 of the european parliament and of the council*, chapter Annex IX - Essential requirements for unmanned aircraft. Official Journal of the European Union, July 2018.

[23] Federal Aviation Administration. Part 23 – small airplane certification process study, July 2009. URL: https://www.faa.gov/about/office_org/headquarters_offices/avs/offices/air/directorates_field/small_airplanes/media/CPS_Part_23.pdf - (17-04-2019).

[24] *UAV Systems Airworthiness Requirements for North Atlantic Treaty Organization Military UAV Systems - STANAG 4671*. NATO, 1st edition, March 2007.

[25] L3 WESCAM. Mx-15d gimbal technical specifications. URL: https://www.wescam.com/technical-specifications/mx-15d - (25-02-2019).

[26] L3 WESCAM. Mx-10d gimbal technical specifications. URL: https://www.wescam.com/technical-specifications/mx-10d/ - (25-02-2019).

[27] Octopus ISR Systems. Epsilon 175 gimbal technical specifications. URL: http://octopus.uavfactory.com/uav-payloads-equipment/epsilon-175 - (25-02-2019).

[28] Garmin ^{TM}. High-definition gmr 18xhd dome radar. URL: https://buy.garmin.com/pt-PT/ES/p/86235 - (25-02-2019).

[29] Ultisat. Unmanned aerial systems beyond-line-of-sight communications system. URL: https://www.sgamf.com/suas/pdf/UAS-SATCOM.pdf - (25-02-2019).

[30] International Civil Aviation Organization (ICAO). Manual of the icao standard atmosphere, 1993. Doc 7488-CD.

[31] Rotron UAV. Rt600lcr-exe engine specifications. URL: http://www.rotronuav.com/engines/rt-600exe#dimensions - (16-04-2019).

[32] Bryan Harris. *Engineering Composite Materials*. The Institute of Materials, London., 1st edition, 1999.

[33] Isaac M. Daniel and Ori Ishai. *Engineering Mechanics of Composite Materials*. Oxford University Press, 1st edition, 1994.

[34] J. N. Reddy. *Mechanics of Laminated Composite Plates and Shells - Theory and Analysis*. CRC Press LLC, 2nd edition, 2004.

[35] Ferdinand P. Beer, E. Russell Johnston Jr., David F. Mazurek, Phillip J. Cornwell, and Elliot R. Eisenberg. *Vector Mechanics For Engineers*. McGraw-Hill, 9th edition, 2010.

[36] B. Etkin. *Dynamics of Flight*, volume I. John Wiley Sons Ltd, 3rd edition, 1982.

[37] Eastern Aero Marine. Eastern aero marine life raft. URL: https://eamworldwide.com/ - (05-05-2019).

Appendix A

Aircraft Configurations

Tail Shape and Mountage Configurations

There are several tail configurations for aircraft depending on the tail planform and also on the way in which the tail is connected with the rest of the aircraft.

The conventional aft tail configuration is the most used in general aviation aircraft. It consists on having the tail assembled in the aft section of the fuselage, meaning that the fuselage spans through the entire length of the aircraft. The variants considered in this document are:

- Conventional A-tail (CAT), as in figure A.1;
- Conventional V-tail (CVT), as in figure A.2;
- Conventional T-tail (CTT), as in figure A.3;
- Conventional Y-tail (CYT), as in figure A.4.

The boom-mounted tail configuration is often seen in the UAV industry. It consists of connecting the tail to the main wing using what is known as tail booms. The variants considered in this document are:

- Boom Mounted V-tail (BMVT), as in figure A.5;
- Boom Mounted A-tail (BMAT), as in figure A.6;
- Boom Mounted H-tail (BMHT), as in figure A.7;
- Boom Mounted L-tail (BMLT), as in figure A.8;
- Boom Mounted Π-tail (BMPT), as in figure A.9;

- Boom Mounted Inverted U-tail (BMIUT), as in figure A.10.

Figure A.1: Gnat 750 by General Atomics, USA.

Figure A.2: Hermes 900 by Elbeit Systems, Israel.

Figure A.3: TD100 by BRICAN, Canada.

Figure A.4: SkyPro V2 by SkyPro, UAE.

Figure A.5: Tiguar C by UAVionics, Poland.

Figure A.6: Wingo by UAVision, Portugal.

Figure A.7: Heron by IAI, Israel.

Figure A.8: Havoc by BrockTek, USA.

Figure A.9: Sky-Y by Alenia Aeronautica, Italy.

Figure A.10: Phoebus by Drone America, USA.

Engine Positioning Configurations

There are three basic configurations regarding the engine positioning, the pusher configuration, the puller configuration and the pusher-puller configuration which is the combination of the first two.

The puller configuration is the most seen in commercial aircraft and has basically two variants:

- Nose Mounted Engine (NME), as in figure A.11;
- Wing Mounted Twin Engines (WMTE), as in figure A.12.

The pusher configuration is widely used in UAVs and has three basic variants:

- Aft Tail Mounted Engine (ATME), as in figure A.13;
- Aft Fuselage Mounted Engine (AFME), as in figure A.14;
- Wing Mounted Engine (WME), as in figure A.15.

Also, some aircraft use a pusher-puller configuration, Fuselage Mounted Twin Engines (FMTE), as in figure A.16.

Figure A.11: Argos by CATUAV, Spain.

Figure A.12: Dominator by ADS, Israel.

Figure A.13: Predator by General Atomics, USA.

Figure A.14: Ogassa by UAVision, Portugal.

Figure A.15: Recon by UASUSA, USA.

Figure A.16: Phoebus by Drone America, USA.

Appendix B

Aircraft Reference Definitions

Aircraft Reference System

In the present document the aircraft reference coordinate systems is presented in figure B.1., where:

- x is the longitudinal axis.
- y is the lateral axis.
- z is the vertical axis.
- u is the linear velocity along the x axis.
- v is the linear velocity along the y axis.
- w is the linear velocity along the z axis.
- p is the angular velocity about the x axis (roll velocity).
- q is the angular velocity about the y axis (pitch velocity).
- r is the angular velocity about the z axis (yaw velocity).
- X is the force applied along the x axis.
- Y is the force applied along the y axis.
- Z is the force applied along the z axis.
- L is the moment about the x axis (roll moment).
- M is the moment about the y axis (pitch moment).
- N is the moment about the z axis (yaw moment).

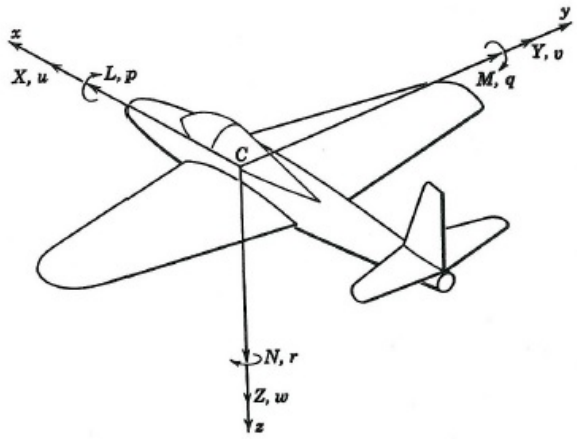

Figure B.1: Aircraft reference coordinate system [36].

Aircraft Reference Measurements

Here the measurements of some parameters are graphically presented for clarification purposes.

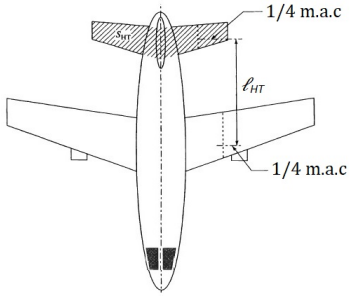

Figure B.2: Horizontal tail placement [7].

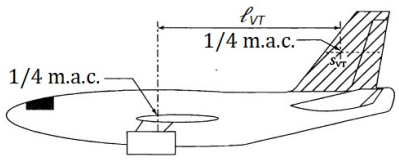

Figure B.3: Vertical tail placement [7].

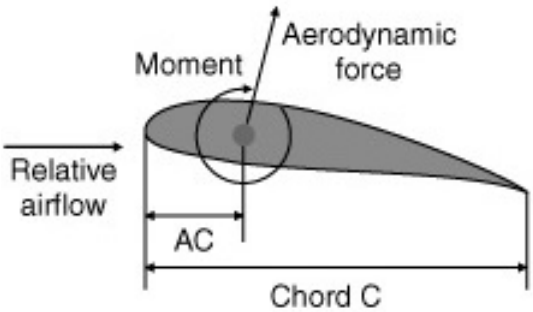

Figure B.4: Location of the aerodynamic center for thin airfoils.

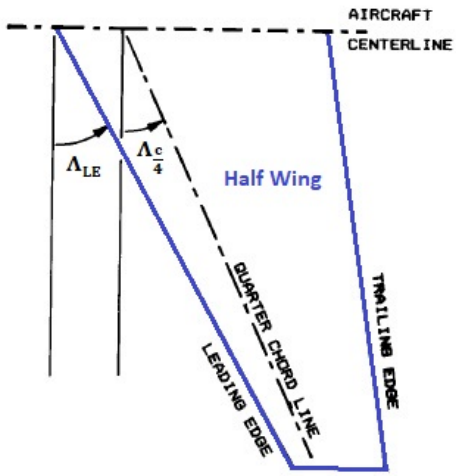

Figure B.5: Leading edge sweep angle and quarter chord line sweep angle definitions [6].

Appendix C

Airfoil Studies

According to B. W. McCormick [20], an analytic formulation for the aircraft C_D may be given by equation C.1 where k is the coefficient of the quadratic term of the parabolic fitting function to the airfoil drag polar. In order to obtain reference k values, ten different airfoils were suited using the XFLR5 software to obtain their drag polar and the data was then treated to obtain the fitting constants. The results of this study are presented in table C.1 and figures C.1, C.2, C.3, C.4, C.5, C.6, C.7, C.8, C.9 and C.10. The main criteria for the selection of the airfoils was their performance at lower Reynolds numbers, therefore most of them are airfoils which were specifically designed for low Reynolds flight.

$$C_D = C_{D_0} + kC_L^2 + \frac{C_L^2}{\pi AR}(1+\delta) \tag{C.1}$$

Table C.1: k values obtained for the airfoils studied.

Airfoil	Re=100k	Re=200k	Re=500k	Re=1M	Re=1.5M	Re=2M	Re=3M
CLARK Y	0,015	0,012	0,008	0,007	0,006	0,006	0,005
EPPLER 387	0,012	0,01	0,01	0,009	0,009	0,008	0,007
EPPLER 403	0,013	0,012	0,01	0,008	0,007	0,007	0,005
EPPLER 423	0,09	0,04	0,026	0,015	0,012	0,012	0,011
NACA 2412	0,01	0,009	0,007	0,005	0,004	0,004	0,003
NACA 23012	0,012	0,01	0,008	0,006	0,006	0,006	0,005
NACA 64110	0,01	0,01	0,01	0,009	0,008	0,008	0,007
SELIG 2027	0,013	0,012	0,009	0,006	0,006	0,005	0,005
SG 6043	0,025	0,021	0,014	0,009	0,007	0,007	0,006
SELIG 1223	0,048	0,034	0,02	0,014	0,012	0,01	0,007

The conclusion of the present study was that it is hard to estimate a generic k value fit for many airfoils. By inspection of table C.1 it is straightforward to see that different airfoils present different k values and even the same airfoil at different Reynolds presents different k values. This means that the

formulation proposed by McCromick [20] for the computation of the drag coefficient is harder to use on a conceptual design phase because it requires computational analysis of the airfoil.

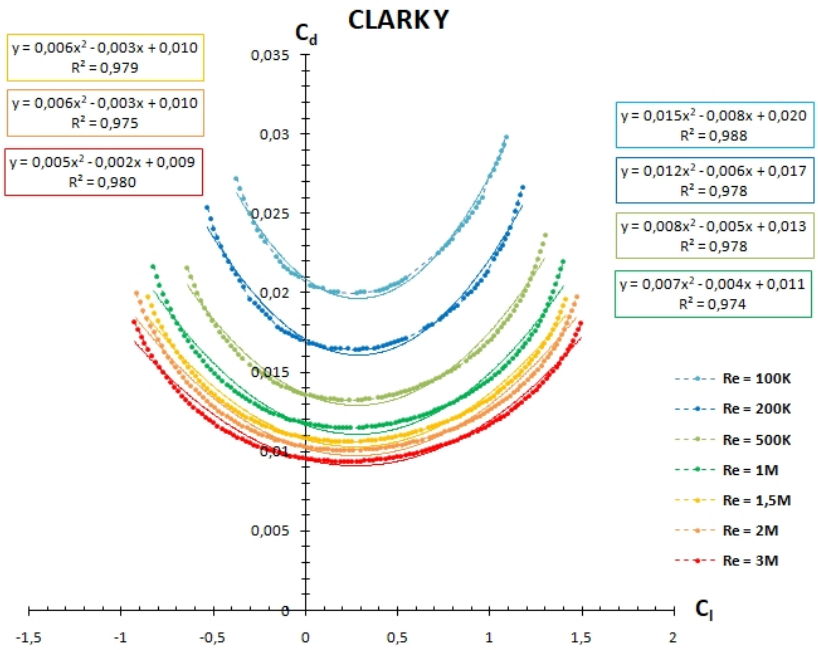

Figure C.1: Parabolic fitting, CLARK Y airfoil.

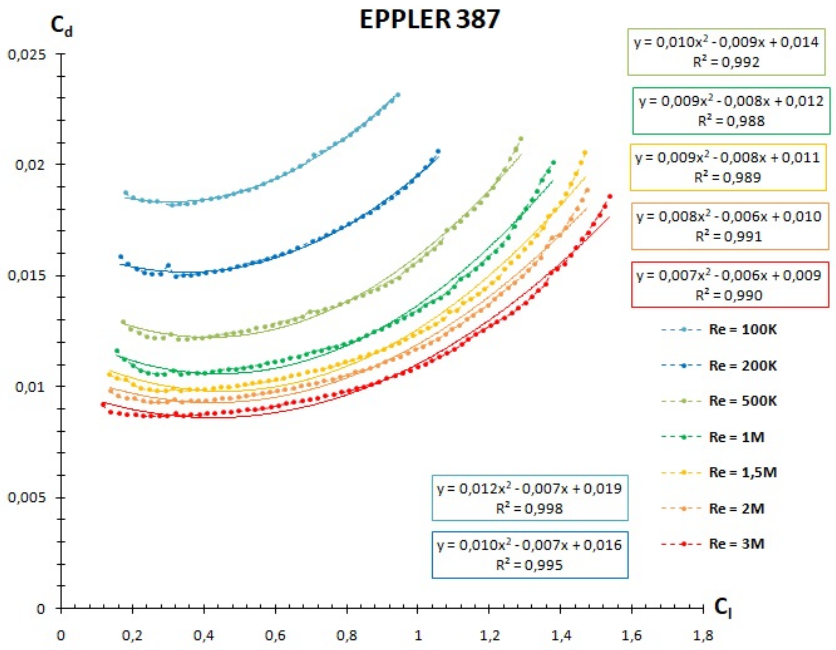

Figure C.2: Parabolic fitting, EPPLER 387 airfoil.

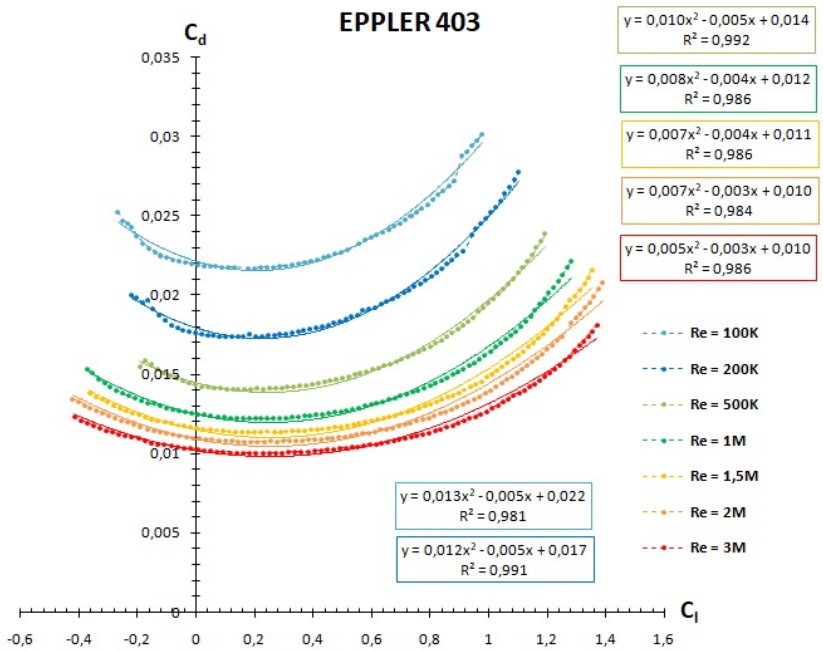

Figure C.3: Parabolic fitting, EPPLER 403 airfoil.

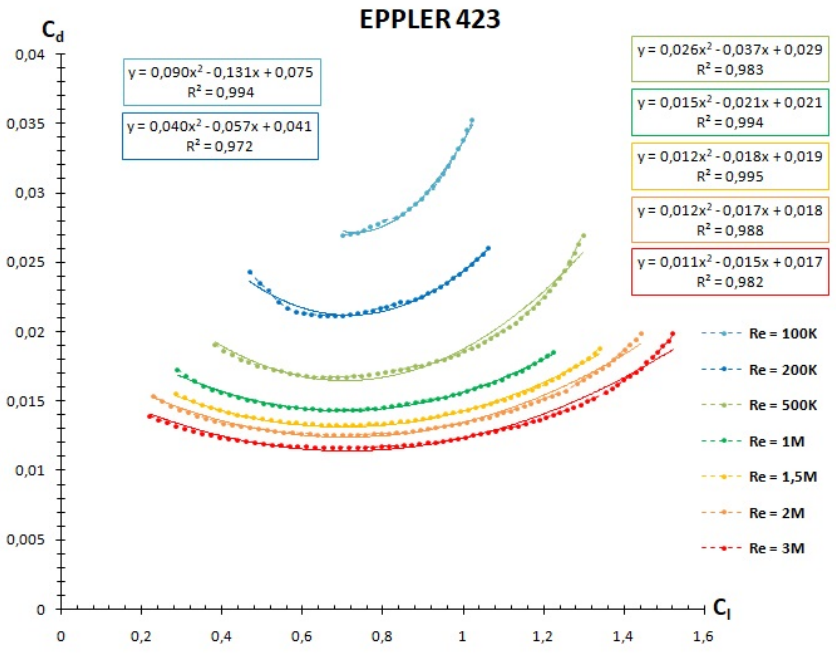

Figure C.4: Parabolic fitting, EPPLER 423 airfoil.

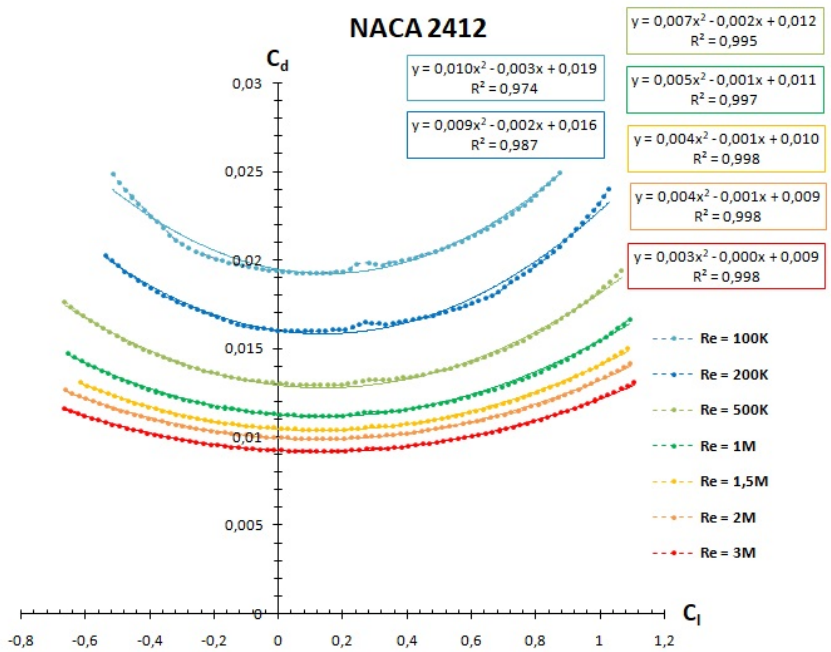

Figure C.5: Parabolic fitting, NACA 2412 airfoil.

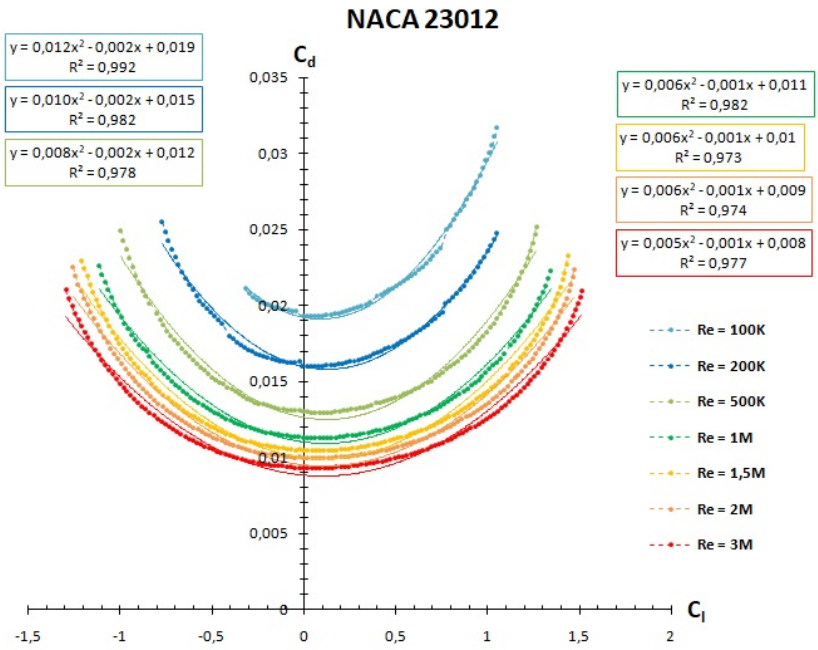

Figure C.6: Parabolic fitting, NACA 23012 airfoil.

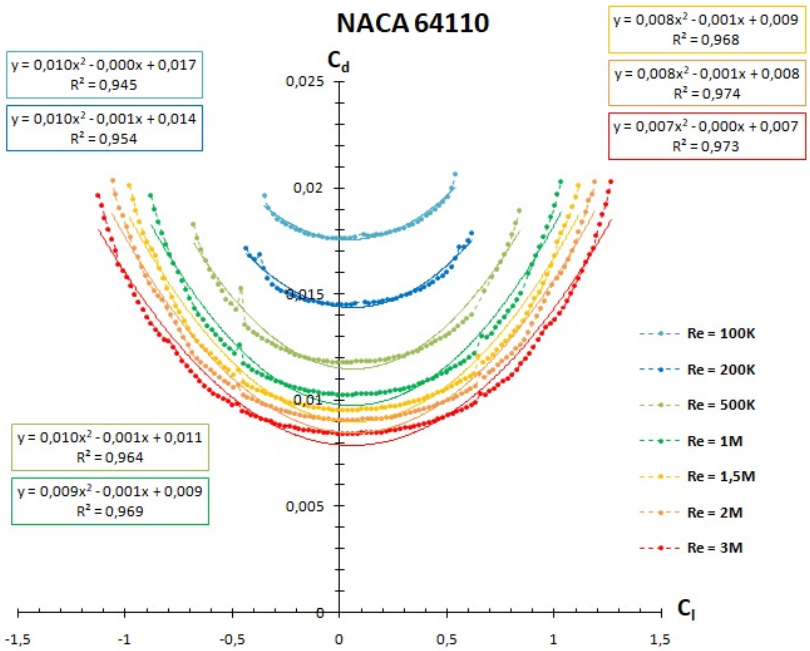

Figure C.7: Parabolic fitting, NACA 64110 airfoil.

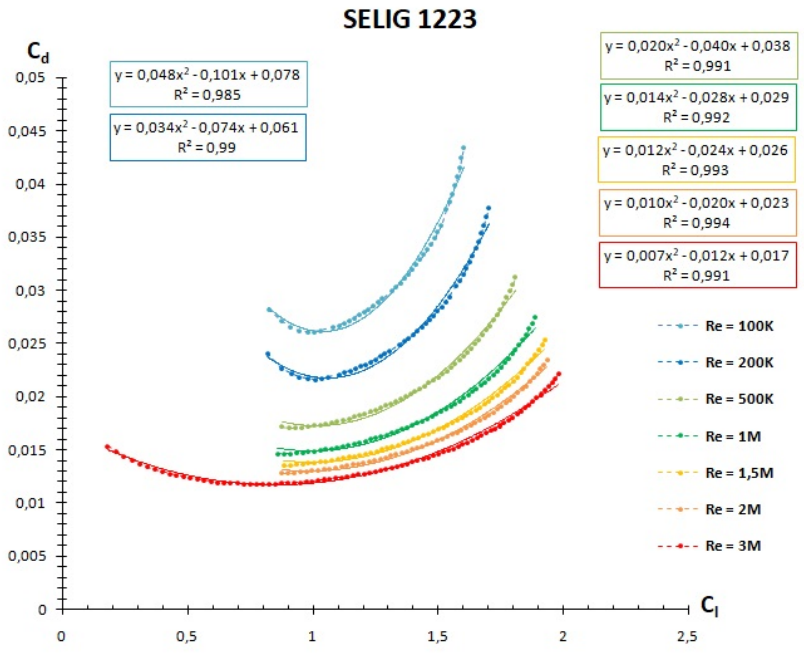

Figure C.8: Parabolic fitting, SELIG 1223 airfoil.

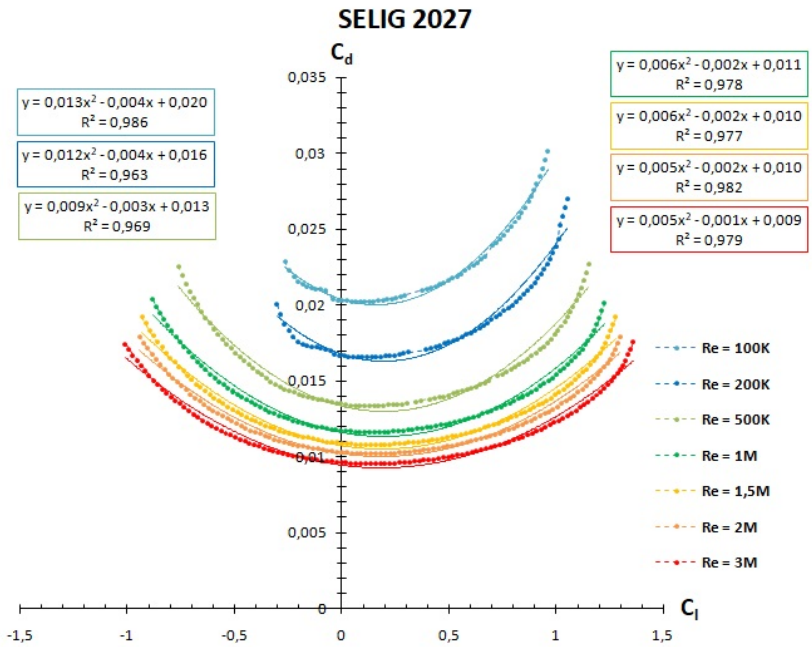

Figure C.9: Parabolic fitting, SELIG 2027 airfoil.

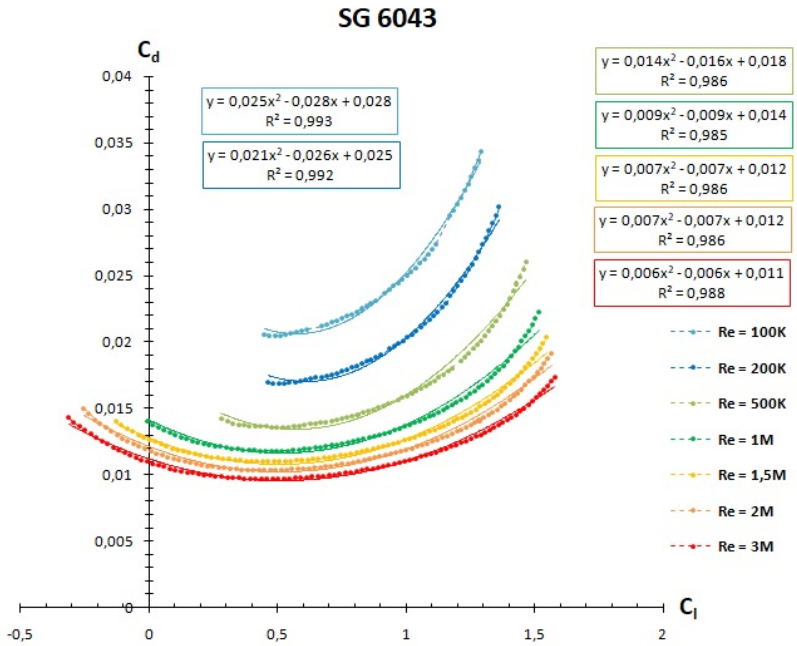

Figure C.10: Parabolic fitting, SG 6043 airfoil.